



VRIJE
UNIVERSITEIT
BRUSSEL

Vrije Universiteit Brussel
Faculteit Wetenschappen en
Bio-ingenieurswetenschappen
Departement Natuurkunde

1

2

3

4

5

6

7

8

9

10

11

12

Search for Dark Matter in the Monojet and Trackless Jets Final States with the CMS Detector at the LHC

Isabelle De Bruyn

Promotor

Prof. Dr. Steven Lowette

Proefschrift ingediend met het oog op het behalen van de
academische graad van Doctor in de Wetenschappen

September 2017

Table of Contents

1

2	1 Introduction	1
3	2 Dark Matter Scenarios Beyond the Standard Model	3
4	2.1 The Standard Model of Particle Physics	3
5	2.1.1 Elementary particles and their interactions	3
6	2.1.2 The theoretical framework of the Standard Model	4
7	2.1.3 Unanswered questions of the Standard Model	6
8	2.2 Dark matter	7
9	2.2.1 Observational evidence	7
10	2.2.2 Dark matter models	10
11	2.2.3 Detection of dark matter	12
12	2.2.3.1 Direct detection experiments	12
13	2.2.3.2 Indirect detection experiments	13
14	2.2.3.3 Collider experiments	15
15	2.2.4 From EFTs to simplified models	16
16	2.3 Strongly Interacting Massive Particles	17
17	2.3.1 The SIMP simplified model	18
18	2.3.2 Experimental constraints	19
19	3 The LHC and the CMS Detector	21
20	3.1 The Large Hadron Collider at CERN	21
21	3.1.1 The LHC injector chain	21
22	3.1.2 The Large Hadron Collider	22
23	3.1.3 The experiments at the LHC	23
24	3.2 The CMS detector	24
25	3.2.1 The tracker	25
26	3.2.1.1 The pixel tracker	25
27	3.2.1.2 The strip tracker	26
28	3.2.2 The electromagnetic calorimeter	26
29	3.2.3 The hadronic calorimeter	28
30	3.2.4 The muon system	28
31	3.2.5 Trigger and data acquisition	30
32	3.2.6 CMS performance in Run 2	31
33	3.2.6.1 Pre-amplifier saturation in the APV25 chip	31
34	4 Event Simulation and Reconstruction	35
35	4.1 Event generation	35
36	4.1.1 Simulation of the monojet signals	38
37	4.2 Detector simulation	38
38	4.3 Event reconstruction	39
39	4.3.1 Track and vertex reconstruction	39
40	4.3.2 Electron and isolated photon reconstruction	41
41	4.3.3 Electron and photon identification	41
42	4.3.4 Muon reconstruction	42
43	4.3.5 Muon identification	43
44	4.3.6 Particle flow	43
45	4.3.7 Jet reconstruction	44
46	4.3.8 Identification of b-jets	45

1	4.3.9	Reconstruction of tau leptons	46
2	4.3.10	Missing transverse momentum reconstruction	46
3	4.4	Simulation and reconstruction of the SIMP signal	46
4	5	The Monojet Analysis	51
5	5.1	Physics object reconstruction	51
6	5.1.1	Jets	51
7	5.1.2	Leptons	51
8	5.1.3	Photons	52
9	5.2	Trigger selection	52
10	5.3	Event selection	54
11	5.4	Background estimation	54
12	5.4.1	The Z and W background estimation	55
13	5.4.2	The QCD background estimation	58
14	5.4.3	Simulation-based background estimation	58
15	5.5	Systematic uncertainties	59
16	5.6	Results	61
17	5.7	Improvements going from the 2015 to 2016 analysis	61
18	5.8	Interpretation	65
19	6	Search for SIMPs using Trackless Jets	69
20	6.1	Physics object reconstruction	69
21	6.1.1	Jets	69
22	6.1.2	Photons	70
23	6.1.3	Primary vertex	70
24	6.2	Trigger selection	71
25	6.3	Event selection	72
26	6.4	Background estimation	74
27	6.4.1	Photon + jets	74
28	6.4.2	QCD multijets	75
29	6.5	Systematic uncertainties	79
30	6.6	Results	81
31	6.7	SIMP model interpretation	81
32	7	Conclusion & Outlook	83

1

Introduction

1

2

2

1

2

3

Dark Matter Scenarios Beyond the Standard Model

4 In modern particle physics, the fundamental structure of matter at subatomic scales is described by the
5 Standard Model [1, 2], which has already predicted many experimental results and is today considered
6 among the most thoroughly tested scientific theories. The Higgs boson, the last missing piece which
7 was predicted more than 50 years ago, was recently discovered at the Large Hadron Collider (LHC) in
8 2012 [3, 4], thus completing this elegant theory. Although it has survived many precision tests so far,
9 the Standard Model only describes 5% of the matter and energy in the known universe and is unable to
10 explain many unresolved questions and observations, such as the baryon asymmetry, dark matter and dark
11 energy, the neutrino masses, the incorporation of gravity, and the hierarchy problem.

12 In this chapter, a brief description of the Standard Model is first given in Section 2.1, including its
13 shortcomings. In Section 2.2, one of the missing pieces in the Standard Model, dark matter, is discussed.
14 The observational evidence for dark matter, as well as possible models and detection mechanisms are
15 detailed. Finally, in Section 2.3 one of the dark matter models considered in this thesis is described in
16 detail.

2.1 The Standard Model of Particle Physics

18 The Standard Model of elementary particle physics has been developed during the second half of the
19 20th century, and reached its current formulation in the 1970's with the combination of the electromagnetic
20 and weak interactions into the electroweak interaction [5–7], incorporating the Brout-Englert-Higgs
21 (BEH) mechanism [8–10], and the addition of asymptotic freedom [11, 12] into the theory of the strong
22 interaction. It is a quantum field theory which describes the fundamental particles and their interactions,
23 incorporating three of the four fundamental forces. While this consistent framework describes the elec-
24 tronagnetic force and the weak and strong nuclear interactions, the fourth interaction, gravity, has not yet
25 been included successfully.

2.1.1 Elementary particles and their interactions

27 All ordinary matter we see around us is built up from atoms, which consist of negatively charged electrons
28 circulating around the positively charged atomic nucleus, formed by protons and neutrons, which in turn
29 consist of up and down quarks. The electrons and up and down quarks are fundamental particles called
30 fermions. Although all ordinary matter can be built from this so-called first generation of fermions,
31 there are twelve fermions with different flavours in total, six quarks and six leptons, grouped in three

1 generations with increasing mass, as shown in Figure 2.1. The electrically neutral neutrinos interact
 2 only via the weak nuclear interaction, which complicates their observation, but they can be detected in
 3 dedicated experiments.

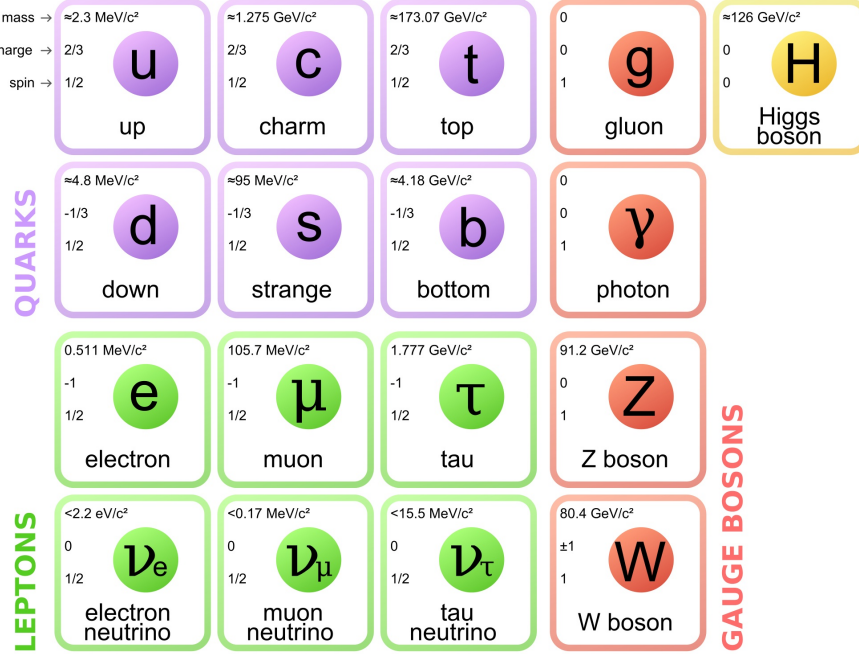


Figure 2.1: The particle content of the Standard Model, showing the fermions divided into 3 generations (columns) on the left and the bosons on the right. The electrical charges are expressed as multiples of the absolute value of the electron charge. Figure taken from [13].

4 A common characteristic of the fermions is their half-integer spin, in contrast to the integer spin of
 5 the force mediators, called bosons. Within the Standard Model, the mediation of the different fundamen-
 6 tal interactions is represented by the exchange of these spin-1 gauge bosons, which are summarized in
 7 Figure 2.1. The massless photon mediates the most familiar force, the electromagnetic interaction, which
 8 is responsible for light, electromagnetic fields, and chemical reactions. The weak nuclear interaction is
 9 among other things used to describe the radioactive β decay, and is propagated by the neutral Z boson
 10 and two charged massive W bosons. Lastly, the strong nuclear interaction is carried by massless glu-
 11 ons, keeping the protons and neutrons in the atomic nuclei and holding the quark constituents together.
 12 A resulting property of the quarks is that they hadronise, i.e. they cannot exist isolated, but form bound
 13 states via the strong interaction. These bound states are referred to as hadrons, and can be made up from
 14 three quarks or a quark and an antiquark, respectively called baryons and mesons.

15 Finally, it is also important to note that for every fermion (f) there exists an antifermion (\bar{f}), which
 16 differs only in electric charge and handedness of spin. When matter and antimatter come into contact
 17 they annihilate, generating energy which can be transformed into other particles.

18 2.1.2 The theoretical framework of the Standard Model

19 The Standard Model goes further than merely giving an exhaustive list of elementary particles, it has a
 20 supporting theoretical framework formulated as a relativistic quantum field theory. In a quantum field
 21 theory, every particle is represented by discrete excitations of a field $\psi(x)$, where x is the space-time
 22 coordinate. The interactions and kinematics of this particle are fully determined by the action S , which
 23 is defined as the integral of the Lagrangian $\mathcal{L}(\psi(x), \partial^\mu \psi(x))$ over the space-time coordinates:

$$S = \int \mathcal{L}(\psi(x), \partial^\mu \psi(x)) d^4x. \quad (2.1)$$

The Lagrangian is a function of the field $\psi(x)$ and its first derivative $\partial^\mu\psi(x)$, where μ represents the index of the space-time coordinate. The physical behaviour of the particles is obtained by following the principle of least action $\delta S = 0$, minimizing the action.

In this framework based on the gauge invariance of the Lagrangian under the fundamental symmetries, the interactions between the fermions and bosons follow automatically. This can be illustrated with the following example for invariance under a general local gauge transformation.

As mentioned before, a fermion has a half integer spin and can thus be represented as a complex relativistic spin-1/2 field, called a Dirac spinor:

$$\mathcal{L}_{Dirac} = i\bar{\psi}\gamma^\mu\partial_\mu\psi - m\bar{\psi}\psi, \quad (2.2)$$

where γ^μ are the Dirac matrices, and the adjoint field $\bar{\psi} = \psi^\dagger\gamma^0$ is the field associated to the antifermion. The imposed local gauge invariance then requires the fermion fields, and the overall Lagrangian, to be invariant under so-called local phase transformations

$$\psi \rightarrow \psi' = U(x)\psi = e^{i\vec{\alpha}(x) \cdot \frac{\vec{\tau}}{2}}\psi \quad (2.3)$$

where $\vec{\alpha}(x)$ are the space-time dependent rotation parameters in the symmetry group represented by the Lie group generators $\vec{\tau}$. Since the derivative ∂_μ in (2.2) spoils the invariance of the Lagrangian under a local phase transformation, it is replaced with a covariant derivative

$$D_\mu = \partial_\mu - ig\frac{\vec{\tau}}{2}\vec{A}_\mu, \quad (2.4)$$

restoring the invariance. This however introduces new vector gauge fields A_μ , which interact with the fermion fields with a coupling strength g . As a result, the Dirac Lagrangian contains an additional term, which describes the interaction between the fermion fields mediated by the gauge fields A_μ , and (2.2) becomes

$$\mathcal{L}_{Dirac} = i\bar{\psi}\gamma^\mu\partial_\mu\psi - m\bar{\psi}\psi + g\bar{\psi}\gamma^\mu\psi\vec{A}_\mu \cdot \frac{\vec{\tau}}{2} \quad (2.5)$$

The matrix $U(x)$ which was introduced above, was defined as a general rotation matrix of the symmetry group $SU(N)$. In order to obtain the three fundamental interactions of the Standard Model, the described procedure can be simplified using the corresponding symmetry groups as mentioned below.

Electroweak theory

The electroweak interaction describes the electromagnetic and weak interactions, which appear very different at low energies but can be merged into a single electroweak force above the electroweak energy scale. This theory is described by requiring gauge invariance under the $SU(2)_L \otimes U(1)_Y$ symmetry group. This leads to 3 gauge fields W_μ^α introduced by the $SU(2)_L$ group, and one gauge field B_μ from the $U(1)_Y$ group. Two coupling constants are introduced, g_1 and g_2 , for $U(1)_Y$ and $SU(2)_L$, respectively. The corresponding observable gauge bosons are the photon, the Z^0 , and the W^\pm bosons.

Quantum Chromodynamics (QCD)

The strong interaction is described by the theory of Quantum Chromodynamics and is represented by the symmetry group $SU(3)$. It describes the interaction between particles that carry a colour charge, which can be red, green, blue, or one of the three corresponding anticolours. There are eight gauge boson fields associated to this group, which are massless and known as gluons. An important aspect which is unique for this interaction is asymptotic freedom, which states that the strong coupling constant, denoted by α_s , goes to zero at high energies. Consequently, the strong force becomes stronger as the distance between the strongly interacting quarks and gluons increases. As a result, the quarks and gluons cannot exist independently and are not observed individually, but are instead confined in colour-neutral hadrons. This effect is called confinement.

At this point the resulting Lagrangian including the three fundamental forces does not contain any mass terms, and so it cannot explain the observed particle masses. Additional mass terms cannot simply

be added explicitly because they would break gauge invariance. Instead, a solution to this problem is found by introducing a complex scalar doublet ϕ with a non-zero vacuum expectation value (vev) v . This breaks the electroweak symmetry and is known as the Brout-Englert-Higgs (BEH) mechanism, postulated in 1964 [8–10]. The Lagrangian of the Higgs field is

$$\begin{aligned}\mathcal{L}_H &= (D^\mu\phi)^\dagger(D_\mu\phi) - V(\phi) \\ &= (D^\mu\phi)^\dagger(D_\mu\phi) - \frac{1}{2}\mu^2\phi^\dagger\phi + \frac{1}{4}\lambda^2(\phi^\dagger\phi)^2,\end{aligned}\quad (2.6)$$

where μ is a real constant representing a mass parameter and λ is a dimensionless parameter standing for the self-interaction strength. The potential V of the scalar doublet has an infinite set of minima or ground states, and by choosing a ground state and expanding the field around it, the electroweak symmetry is broken. As a result, three of the four original fields of the scalar doublet are absorbed by the massless vector fields of the weak interaction, giving mass to the W and Z bosons:

$$M_W = \frac{1}{2}vg_2 \quad M_Z = \frac{1}{2}v\sqrt{g_1^2 + g_2^2}. \quad (2.7)$$

From the remaining field, the H boson arises, acquiring a mass $m_H = \sqrt{2\lambda v}$.

The introduction of mass terms for the fermions also follows from the BEH mechanism, which allows to insert the following gauge-invariant term in the Lagrangian:

$$\mathcal{L}_{Yukawa} = -Y_{ij}\bar{\psi}_{L,i}\phi\psi_{R,j} + h.c. \quad (2.8)$$

with the Y_{ij} Yukawa matrices. The L and R here denote left-handed and right-handed fermions. This handedness or chirality is defined as $\psi_L = \frac{1}{2}(1 - \gamma_5)\psi$ for left-handed and $\psi_R = \frac{1}{2}(1 + \gamma_5)\psi$ for right-handed fermions. The fermion masses then arise from the Yukawa interactions describing the couplings of the fermions with the Higgs field. For massive particles, a reference frame which overtakes the spinning particle can always be found, in which case the particle will seem to move backwards, flipping its helicity¹. This is however not the case for massless particles, which travel at the speed of light. As only left-handed neutrinos and right-handed antineutrinos have been observed so far, the neutrinos are massless in the Standard Model.

2.1.3 Unanswered questions of the Standard Model

Although the Standard Model is an extremely successful theory, there are still many questions that remain unanswered, indicating that the Standard Model cannot be a complete theory of nature. A brief description of some of the main unsolved problems follows here.

Grand Unified Theory

As the weak and electromagnetic interactions were successfully unified into the electroweak one, the idea of representing the three forces of the Standard Model by a single one is envisaged and studied. While this Grand Unified Theory (GUT) could be a first step towards the incorporation of gravity in the Standard Model, it cannot be achieved with the current Standard Model and requires new physics at a very high energy scale.

Baryon asymmetry

This problem refers to the imbalance of matter and antimatter in the universe. While the Big Bang should have produced an equal amount of baryonic and antibaryonic matter, this is not measured in our observable universe. It is assumed that most of the primordial matter and antimatter annihilated, but an imbalance allowed a fraction of the matter to survive. Within the Standard Model, some asymmetry in the production of matter and antimatter could be explained by the CP-violation² of the weak interaction. However, the amount of CP-violation needed to explain the baryon asymmetry is ten times higher than is observed from Standard Model measurements.

¹The helicity is defined as the sign of the projection of the spin vector onto the momentum vector of a particle, left is negative and right is positive.

²According to Charge Parity (CP) symmetry, the laws of physics should remain identical when converting a particle into its antiparticle and mirroring the space coordinates. However, measurements of e.g. kaon-antikaon mixing show that this symmetry is violated.

1 **Hierarchy problem**

2 The most important hierarchy problem concerns the question why the weak force is so much
 3 stronger than gravity. The measured vector boson masses suggest that the electroweak symme-
 4 try breaking should occur at an energy scale of $\mu^2 \sim (100 \text{ GeV})^2$, while the energy regime
 5 where gravity becomes comparable to the other forces, called the Planck scale, is of the order
 6 of $\Lambda_{\text{Planck}} \sim 10^{19} \text{ GeV}$. This question is related to the mystery as to why the Higgs boson mass is
 7 so much smaller than the Planck scale. The real physical Higgs boson mass is composed of its bare
 8 mass and quantum loop corrections. These corrections depend strongly on a cut-off scale, which
 9 would be the Planck scale if no additional physics on top of the Standard Model is present up to
 10 this scale. In order for the theoretical prediction to match the experimentally determined mass of
 11 125 GeV, the bare mass would need to be tuned to cancel the huge quadratic radiative corrections.
 12 This would require a significant fine-tuning of more than 30 orders of magnitude, which is not
 13 desirable for any theory.

14 **Neutrino masses**

15 The Standard Model predicts that the neutrinos are massless weakly interacting particles, but ob-
 16 servations by the Sudbury Neutrino Observatory [14] and Super-Kamiokande [15] collaborations
 17 showed the first clear evidence that the neutrinos oscillate from one flavour into another. This can
 18 only be explained if the neutrinos differ in mass, implying that they are not massless. As men-
 19 tioned above, the Standard Model does not provide masses for the neutrinos and it should therefore
 20 be extended to explain this observation.

21 **Dark matter and energy**

22 This mystery arises from cosmological observations, which indicate that the known matter de-
 23 scribed by the Standard Model makes up only 5% of the matter and energy in the universe. The
 24 remaining matter, called dark matter, contributes another 27%, and will be discussed in more detail
 25 in Section 2.2. In the Standard Model, neutrinos contribute to the dark matter, but their relic density
 26 is by far not enough to account for all the dark matter. The last 68% has been labelled dark energy
 27 and is believed to be responsible for the acceleration of the observed expansion of the universe, but
 28 remains even more enigmatic as no explanation can be provided by the Standard Model.

29 **2.2 Dark matter**

30 One of the current open questions in particle physics that is not answered by the Standard Model is the ex-
 31 istence of dark matter. Many astrophysical observations from gravitational effects (see for instance [16])
 32 show there must be some additional matter in the universe, the so-called dark matter, next to the known
 33 matter. Despite this, its precise nature remains as of yet unknown. Countless theoretical models are being
 34 constructed in order to explain its origin, and on the experimental side dark matter is being looked for in
 35 many different ways, but no observation has been made so far.

36 **2.2.1 Observational evidence**

37 The first hints of dark matter were observed by F. Zwicky [17] in 1933 by studying the velocity dispersion
 38 of galaxies in the Coma cluster. The effect is not only observed for entire galaxies, but also for various
 39 luminous objects, such as stars or gas clouds, inside a galaxy. The rotation curves of galaxies have been
 40 well studied, and show clear evidence for the existence of dark matter. An example of a rotation curve is
 41 shown in Figure 2.2, exhibiting a flat behaviour of the rotational velocity at large distances, going even
 42 far beyond the edge of the visible disk. However, in Newtonian dynamics the circular velocity is expected
 43 to be

$$v(r) = \sqrt{\frac{GM(r)}{r}}, \quad (2.9)$$

44 where $M(r) = 4\pi \int \rho(r)r^2 dr$ with $\rho(r)$ the mass density profile. Assuming $M(r)$ to be constant, the
 45 circular velocity is expected to fall like $1/\sqrt{r}$ beyond the disk. Since the measurements show an approx-
 46 imately constant velocity but a dropping visible mass density, this implies the existence of a halo with

¹ $M(r) \propto r$ and $\rho(r) \propto 1/r^2$. A universal density profile seems to be suggested by the rotation curves of
² both low and high surface luminosity galaxies, consisting of an exponential thin stellar disk and a spheri-
³ cal dark matter halo with a flat core of radius r_0 and density $\rho_0 = 4.5 \times 10^{-2} (r_0/\text{kpc})^{-2/3} M_\odot \text{pc}^{-3}$ [18]³.

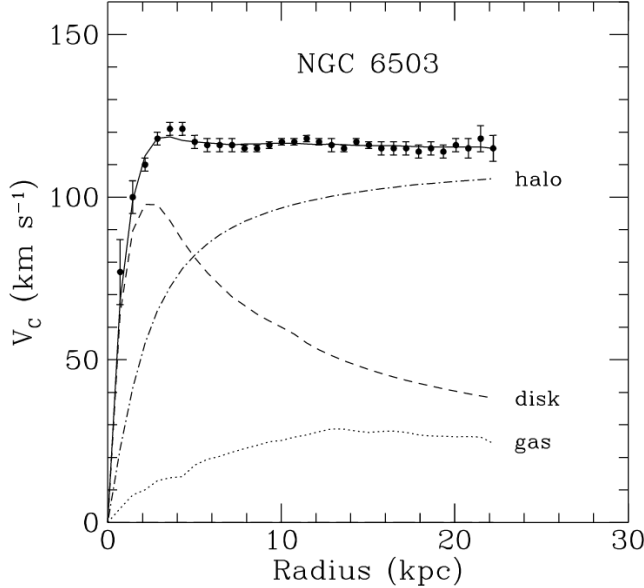


Figure 2.2: Rotation curve of NGC 6503. The dotted, dashed, and dash-dotted lines show the contributions of gas, disk, and dark matter, respectively. Figure taken from [19].

⁴ Another evidence for dark matter comes from the effect of gravitational lensing, allowing to determine
⁵ the mass of an object regardless of the light it emits. When a distant star or quasar is aligned with a
⁶ massive compact object, the bending of its light due to the gravitational field of the massive object can
⁷ lead to multiple distorted, magnified, and brightened images, as illustrated in Figure 2.3. The distortion
⁸ of the image can then be used to determine the potential well and thus the mass of the heavy object.
⁹ Yet another way to determine the mass of a cluster of galaxies, next to gravitational lensing and the
¹⁰ distribution of radial velocities, is by studying the profile of X-ray emission, tracing the distribution of
¹¹ the hot emitting gas in clusters. In general, these three methods are in reasonable agreement with each
¹² other.

¹³ Additionally, at a cosmological level, the analysis of the Cosmic Microwave Background (CMB)
¹⁴ allows to determine the total amount of dark matter in the universe. The existence of this isotropic
¹⁵ background radiation was already predicted in 1948, and unintentionally discovered by A. Penzias and
¹⁶ R. Wilson in 1965 [21]. This relic radiation comes from the propagation of photons in the early universe,
¹⁷ once they decoupled from matter. Before this, the photons were energetic enough to ionise hydrogen,
¹⁸ creating a plasma of electrons and protons which were unable to combine into hydrogen. As the universe
¹⁹ expanded and cooled down, the photons also cooled down enough to let the hydrogen atoms recombine,
²⁰ and the universe became transparent. The photons can then travel freely without scattering off the protons
²¹ and electrons of the plasma, still carrying information from this surface of last scattering. The CMB is
²² now known to be isotropic at the level of 10^{-5} and to follow the spectrum of a black body corresponding
²³ to a temperature of 2.726 K. However, small anisotropies in the CMB have first been observed by the
²⁴ COBE satellite [22] and more recently by WMAP [23] and Planck [24], as can be seen in Figure 2.4.
²⁵ These anisotropies correspond to small thermal variations, and are usually expanded as

$$\frac{\delta T}{T}(\theta, \phi) = \sum_{l=2}^{+\infty} \sum_{m=-l}^{+l} a_{lm} Y_{lm}(\theta, \phi), \quad (2.10)$$

³ M_\odot denotes a solar mass, 2×10^{30} kg.

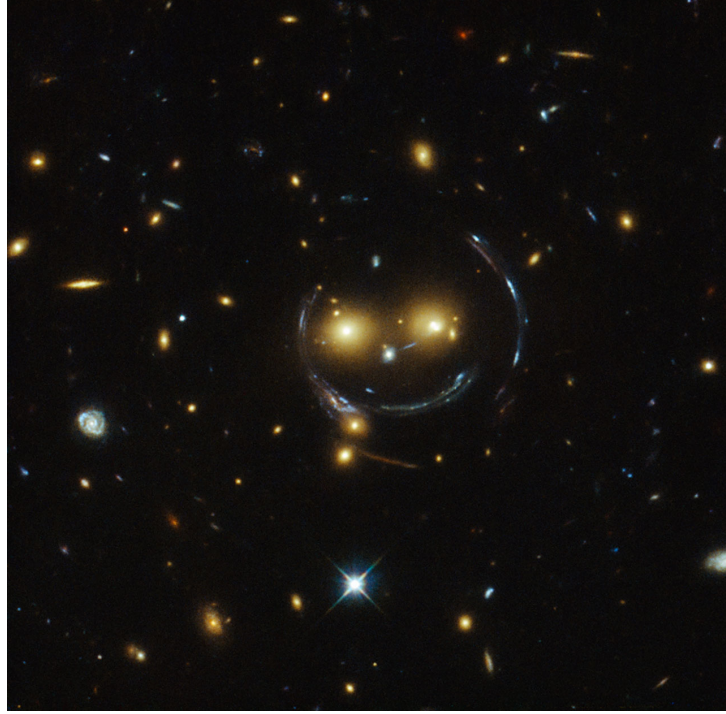


Figure 2.3: An example of gravitational lensing showing the “Cheshire Cat” image of galaxy cluster SDSS J1038+4849, taken by the Hubble Space Telescope. Figure taken from [20].

1 where $Y_{lm}(\theta, \phi)$ are spherical harmonics. The variance of a_{lm} is given by

$$C_l = \langle |a_{lm}|^2 \rangle = \frac{1}{2l+1} \sum_{m=-l}^{+l} |a_{lm}|. \quad (2.11)$$

2 As the temperature fluctuations appear to be Gaussian, all the information contained in the CMB anisotropy
3 maps can be condensed into the power spectrum given by the behaviour of C_l as a function of l . This is
4 generally represented using $D_l = l(l+1)C_l/2\pi$, as illustrated in Figure 2.5.

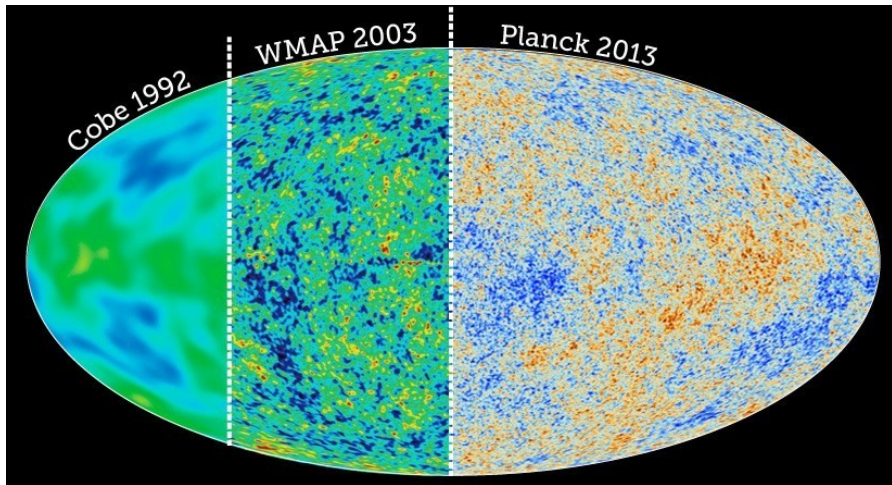


Figure 2.4: The CMB temperature fluctuations obtained from the COBE, WMAP, and Planck data. Figure taken from [25].

5 The CMB anisotropies are caused by acoustic oscillations arising from the conflict between the grav-
6 itational pull from baryons and dark matter and the repulsive force due to the radiation pressure from the

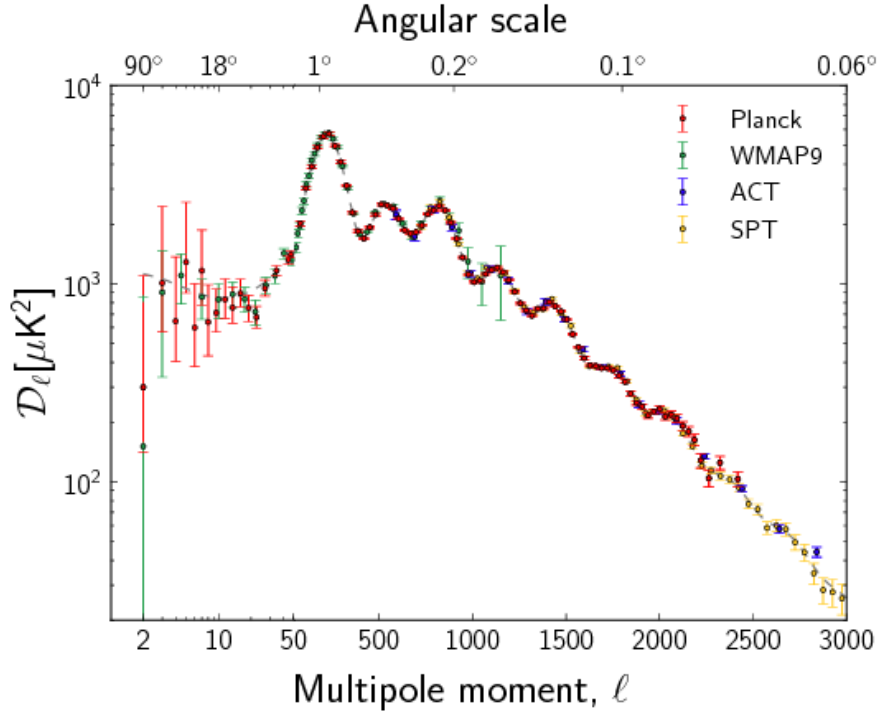


Figure 2.5: The observed power spectrum of the CMB anisotropies. The horizontal axis is logarithmic up to $l = 50$ and linear beyond. Figure taken from [26].

1 photons. One popular model to describe and interpret these observations is the Λ CDM model. CDM
 2 stands for cold dark matter, indicating that in this model the dark matter particles are moving slowly compared
 3 to the speed of light, while the Λ represents the cosmological constant, which is associated with the
 4 vacuum energy or dark energy that is used to explain the accelerating expansion of space. The Λ CDM
 5 model is compatible with a number of observations beyond the CMB fluctuations, such as the large scale
 6 structure in the distribution of galaxies, the relative abundance of light nuclei, and the accelerating expansion
 7 of the universe which is observed from the red shift of well-known spectral absorption or emission
 8 lines in the light of distant galaxies. Using this model to fit the power spectrum, the multiple peaks in the
 9 spectrum can be interpreted. The angular scale of the first peak can be used to determine the curvature of
 10 the universe. The second peak determines the reduced baryon density and the third peak can be used to
 11 retrieve information about the dark matter density. From the analysis of the Planck data the abundance of
 12 baryons and matter in the universe is determined to be

$$\Omega_b h^2 = 0.02205 \pm 0.00028 \quad \Omega_M h^2 = 0.1423 \pm 0.0029 \quad (2.12)$$

13 This result shows that only about 15% of the matter in the universe is made up from the ordinary known
 14 matter, and the remaining 85% is called dark matter.

15 More evidence for dark matter was found from a great variety of data, both on subgalactic and inter-
 16 galactic scales. Without discussing them here in detail, a few examples are the velocity dispersions of spi-
 17 ral galaxy satellites, suggesting the existence of dark halos around spiral galaxies extending well beyond
 18 the visible disk [27], the velocity dispersion of dwarf spheroidal galaxies, implying larger mass-to-light
 19 ratios than those observed in our local neighbourhood [28], and the so-called Oort discrepancy in the disk
 20 of the Milky Way, inferring the existence of dark matter from the inconsistency between the amount of
 21 stars in the solar neighbourhood and the gravitational potential indicated by their distribution [29].

22 **2.2.2 Dark matter models**

23 Since very little is known so far concerning the nature of dark matter, a multitude of dark matter candidates
 24 are discussed in the literature. Without attempting to be complete, a list is given and a few of the more

1 popular candidates are briefly covered here.

2 Standard Model neutrinos

3 As mentioned before, the Standard Model could explain the existence of dark matter with the
4 already observed neutrinos. However, it can be shown [30] that their total relic density is predicted
5 to be

$$\Omega_\nu h^2 = \sum_{i=1}^3 \frac{m_i}{93 \text{ eV}}, \quad (2.13)$$

6 taking the sum over the 3 neutrino flavours. Currently, the most stringent upper bound on neutrino
7 masses is

$$m_\nu < 2.05 \text{ eV} \quad \text{at 95\% CL} \quad (2.14)$$

8 obtained in tritium β -decay experiments at Troitsk [31, 32] and Mainz [33]. Since the mass difference
9 between the 3 neutrinos must be very small to explain solar and atmospheric neutrino anomalies [34], this mass limit applies to the three mass eigenvalues, implying an upper bound on
10 the total neutrino relic density of

$$\Omega_\nu h^2 \lesssim 0.07. \quad (2.15)$$

11 This shows that Standard Model neutrinos are not abundant enough to be the dominant component
12 of dark matter.

14 Sterile neutrinos

15 Proposed in 1993 by Dodelson and Widrow [35], these hypothetical particles are similar to the
16 Standard Model neutrinos, but without Standard Model weak interactions, except for mixing. The
17 analysis of their cosmological abundance and the study of their decay products places stringent con-
18 straints on the sterile neutrinos. Light neutrinos with masses below a few keV would for example
19 be ruled out [36].

20 Axions

21 These particles were originally introduced to solve the problem of the apparent absence of CP-
22 violation by the strong interaction, and have often been discussed as dark matter candidates. They
23 are expected to interact extremely weakly with Standard Model particles. Furthermore, observa-
24 tions from laboratory searches, stellar cooling, and the dynamics of supernova 1987A constrain the
25 axion mass to be very small, of the order of or below 0.01 eV [37].

26 SUSY candidates

27 Several particles in supersymmetry (SUSY) models can serve as dark matter candidate, such as
28 gravitinos and neutralinos. Gravitinos are the superpartners of the graviton. In some SUSY models,
29 they can be the lightest supersymmetry particle and can be stable. While they are very strongly
30 motivated theoretically, they are very difficult to observe, as they only interact gravitationally. The
31 neutralinos are the superpartners of the photon, Z boson, and neutral Higgs bosons. The lightest
32 of the four is stable and is an excellent dark matter candidate. These dark matter candidates are
33 often called weakly interacting massive particles (WIMPs), since they are massive and interact
34 through the weak interaction. As many SUSY models predict a new particle with the correct
35 properties and self-annihilation cross section to obtain the correct abundance of dark matter today,
36 a stable supersymmetric partner has long been a very plausible dark matter candidate and a lot of
37 experimental effort has been made to detect it.

38 WIMPs

39 A prevalent assumption is that dark matter particles are a relic from the early universe, when all
40 particles were in thermal equilibrium. At those high energies the dark matter particles and antiparti-
41 cles could be formed by sufficiently energetic lighter particles, and they would annihilate back into
42 these lighter particles as well. However, as the universe expanded and cooled down, the thermal en-
43 ergy of the lighter particles became insufficient to form dark matter particle-antiparticle pairs. The
44 annihilation of the dark matter particles and antiparticles continued however, until the dark matter

1 density decreased considerably and the interaction between the dark matter particles stopped. The
 2 number of dark matter particles would remain constant from that moment on. In comparison, par-
 3 ticles with a large interaction cross section would continue to annihilate for a longer period of time
 4 and would be less abundant.

5 The interaction cross section of the annihilating dark matter particles can be inferred from the
 6 current estimates of the dark matter abundance in the universe, and can in this case not be larger
 7 than the cross section of the weak interaction. According to this model, WIMPs would be the
 8 perfect candidates for dark matter. In general, they are hypothetical new elementary particles that
 9 interact gravitationally and through any other force which is as weak or weaker than the Standard
 10 Model weak interaction, and they could have been produced thermally as described in this model.
 11 Since WIMPs have a relatively large mass, they would also constitute cold dark matter, which
 12 would fit the observed large scale structure of the universe. The coincidence of WIMPs fitting
 13 so well into this model and corresponding to the current observations is known as the “WIMP
 14 miracle”.

15 Many more dark matter candidates are discussed in literature, such as but not limited to heavy fourth
 16 generation neutrinos [38], Kaluza-Klein states in ADD [39] or RS [40] extra dimensions models,
 17 superheavy dark matter or Wimpzillas [41], self-interacting dark matter [42], charged massive particles
 18 (CHAMPs) [43], and Q-balls [44]. More detailed reviews are given in [30, 45, 46].

19 **2.2.3 Detection of dark matter**

20 The detection of dark matter can be categorised in three groups, based on the diagram shown in Figure 2.6.
 21 In the case of direct detection experiments, the studied process is the scattering of dark matter off ordinary
 22 matter. Experiments searching for dark matter with the indirect approach look for particles or radiation
 23 produced in the annihilation of dark matter particles. Finally, at collider experiments, attempts are made
 24 to produce and detect dark matter particles by colliding Standard Model particles at high energies.

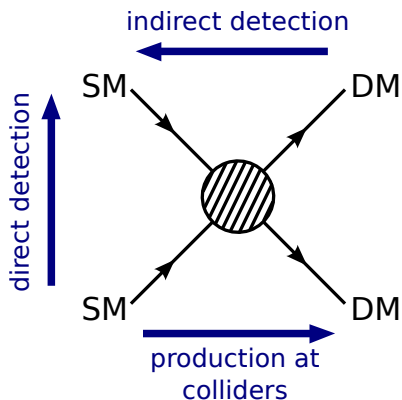


Figure 2.6: Diagram illustrating the three used methods to detect dark matter.

25 **2.2.3.1 Direct detection experiments**

26 This category of experiments is based on the fact that if our galaxy is filled with a static halo of dark
 27 matter particles, then many of them should pass through the Earth as it rotates around Galactic Center,
 28 and they could be detected by looking for the interaction of such particles with matter. This is for example
 29 done by recording the recoil energy of nuclei when WIMPs scatter off them. In order to determine the
 30 expected rate of events per unit detector material mass, the WIMP-nucleon scattering cross section and
 31 the density and velocity distribution of the WIMPs in the solar neighbourhood are needed.

32 There are several types of scattering processes which can be classified by two relevant characteristics:
 33 elastic or inelastic scattering and spin-dependent or spin-independent scattering. In the case of elastic
 34 scattering, the WIMP simply scatters off a nucleus as a whole, causing it to recoil. The recoil energy

1 spectrum can then be measured by detecting the emitted scintillation light with very sensitive detectors
 2 or by measuring very small temperature changes due to crystal vibrations. Taking a Maxwell-Boltzmann
 3 velocity distribution with as characteristic velocity our rotation velocity of about 270 km/s, the recoil
 4 spectrum is exponential with typical energies of $\langle E \rangle \sim 50$ keV. This range of energies is easily detectable
 5 by current experiments, which can detect recoils as low as 1-10 keV. Instead, when the WIMP scatters
 6 inelastically, it interacts with the orbital electrons of the target, exciting the electrons or ionising the
 7 target. Differently, the WIMP could also excite the target nuclei, which would then emit a photon about a
 8 nanosecond after the observed recoil. This signature has, however, to compete with the background from
 9 natural radioactivity.

10 The spin dependence or independence of the scattering depends on the coupling of the WIMPs to
 11 the Standard Model particles. Spin-dependent interactions result from couplings to the spin content of a
 12 nucleon, yielding cross sections that are proportional to $J(J+1)$ instead of the number of nucleons. For
 13 spin-independent interactions, the cross section instead increases considerably with the mass of the target
 14 nuclei. The spin-independent scattering therefore dominates over the spin-dependent one in experiments
 15 which use heavy atoms.

16 Numerous direct detection experiments are currently operational or in development. They use one or
 17 more techniques to measure the nuclear recoil, by detecting the scintillation light, the change in tempera-
 18 ture, or the ionisation. Some experiments also try to separate the WIMP signatures from the background
 19 by looking for an annual modulation in the rate, which arises due to the Earth's movement around the
 20 Sun. This effect causes the Earth to have a relative velocity with respect to the galaxy's reference frame,
 21 given by

$$v_E = 220 \text{ km/s} (1.05 + 0.07 \cos(2\pi(t - t_m))), \quad (2.16)$$

22 where the time is in units of years and t_m is approximately the beginning of June. As a result, a small
 23 variation of about 7% in the WIMP flux can be measured in the direct detection rate.

24 Currently, there is some tension between the results obtained by the different experiments, as some
 25 observations can be interpreted as dark matter signals, while other experiments are ruling out those mod-
 26 els. The DAMA experiment for example observes an annual modulation in the event rate, pointing to the
 27 existence of WIMPs scattering elastically off the sodium and iodine nuclei in the detector [47]. Other
 28 experiments, such as SuperCDMS [48], EDELWEISS-III [49], CRESST-II [50], XENON100 [51], have
 29 seen no evidence for dark matter so far and placed limits on many dark matter models, creating a tension
 30 with the observed signal at DAMA. For WIMP masses above a few GeV, the strongest limit of direct
 31 detection experiments for spin-independent interactions is currently given by LUX [52]. For a spin-
 32 dependent WIMP-proton cross section, the most stringent limit is set by the PICO experiment [53], while
 33 the PandaX experiment places the strongest limit on the WIMP-neutron cross section [54]. An overview
 34 of the existing limits and signal observations is given in Figure 2.7, showing the mentioned experiments,
 35 and a more complete review of the existing direct detection results is given in [55].

36 2.2.3.2 Indirect detection experiments

37 The indirect detection of dark matter is performed by looking for radiation produced in dark matter
 38 annihilations. A reasonable place to look at would then be in regions with large dark matter densities and
 39 thus larger annihilation rates, which will result in a higher flux of the studied radiation. Some examples
 40 are dense regions of the galactic halo such as the galactic centre, or objects like the Sun or the Earth,
 41 which could also capture dark matter particles through scattering with nucleons in their core. In the latter
 42 case, only neutrinos would be able to escape those dense objects. Other annihilation products include
 43 gamma rays, positrons, and antiprotons.

44 In order to observe gamma rays directly, the detectors must be placed in space, as photons of the
 45 relevant energy range (GeV to TeV) interact with matter via e^+e^- pair production and cannot traverse
 46 more than a surface density of about 38 g cm^{-2} . The gamma rays will not reach the ground-based
 47 telescopes as the Earth's atmosphere is 1030 g cm^{-2} thick. Nevertheless, efforts are being made to
 48 observe gamma rays indirectly via ground-based experiments as well, by detecting the secondary particles
 49 and the Cherenkov light produced by their passage through the Earth's atmosphere. In the energy range
 50 between approximately 100 MeV and 100 GeV, gamma ray telescopes on satellites such as the Fermi

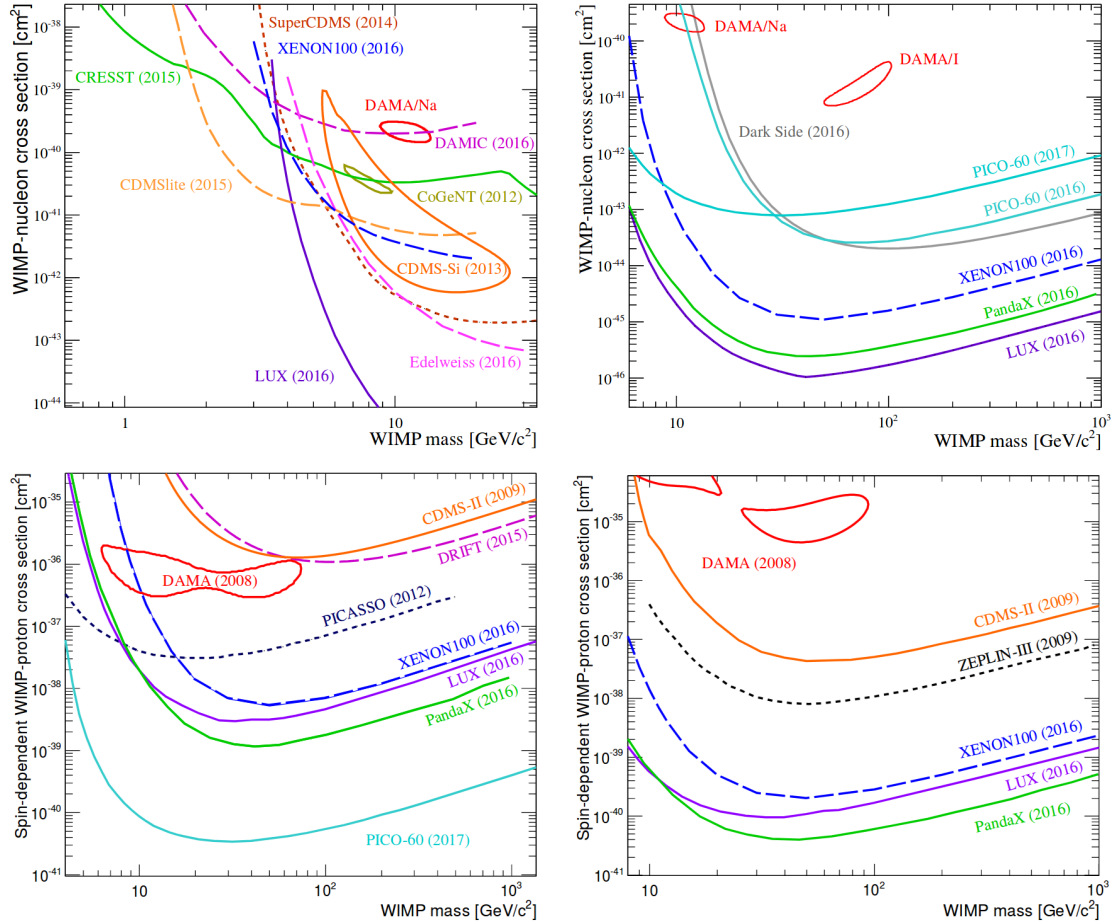


Figure 2.7: Overview of the current limits for spin-independent WIMP-nucleon interactions at low (top left) and high (top right) WIMP masses, spin-dependent WIMP-proton interactions (bottom left), and spin-dependent WIMP-neutron interactions (bottom right). The observed signals from DAMA, CoGeNT, and CDMS-Si are shown as well. Figure taken from [55].

1 Large Area Telescope [56] are being used. Above 100 GeV, the ground-based Imaging Air Cherenkov
 2 Telescopes such as HESS [57], MAGIC [58], and VERITAS [59] become more adequate.

3 Neutrinos can also be produced in the annihilation of dark matter particles, but they are considerably
 4 more difficult to detect than gamma rays due to their weak interaction with ordinary matter. They are
 5 not easily absorbed, which makes it possible to observe them with underground, low-background ex-
 6 periments. Very energetic neutrinos, in the GeV-TeV range, are most easily observed by detecting the
 7 Cherenkov light from muons produced through charge current interactions of the neutrinos inside of or
 8 close to the detector volume. Two very large neutrino detectors are ANTARES in the Mediterranean
 9 Sea [60] and IceCube at the South Pole [61].

10 Additionally, evidence for dark matter annihilations can also be found by studying the spectra of
 11 cosmic positrons and antiprotons. Contrary to neutrinos and gamma rays, these charged particles do not
 12 point to their source, as their trajectory is modified by the presence of galactic magnetic fields. Currently,
 13 the main detector for positrons and antiprotons is AMS [62], which is operating on the International Space
 14 Station. Until 2016, PAMELA [63] was also active on board of the Resurs-DK1 satellite.

15 Finally, radio emissions from the galactic halo, and in particular from the galactic centre, can also
 16 provide evidence for dark matter annihilation. Electrons and protons produced in dark matter annihi-
 17 lations will emit synchrotron radiation at radio wavelengths as they move through galactic magnetic fields.
 18 This type of searches is performed with radio telescopes and belongs to the realm of classical astronomy.

2.2.3.3 Collider experiments

Since dark matter particles are usually assumed to be neutral and to interact only weakly with ordinary matter, they are expected to pass through the detectors at colliders without leaving a signal, similar to neutrinos. These particles can however still be searched for at colliders as well, when they are produced in association with other visible particles which are detected as jets or charged leptons. The dark matter particles are then observed as missing energy, as they create an imbalance in the net momentum in the transverse plane perpendicular to the colliding beams, which should be zero. One of these flagship analyses is the monojet analysis, looking for dark matter produced together with one or more jets [64, 65]. Similarly, many more searches are performed at the CMS and ATLAS experiments at the LHC by looking for signatures containing missing energy. Recent summaries are given in [66] and [67].

Additionally, other signatures without missing energy can also be used to search for dark matter. If the dark matter particle is produced in a cascade of decays for example, different signatures can be obtained, such as displaced vertices [68], disappearing tracks [69], and displaced lepton-jets [70]. Furthermore, in dijet searches [71–73], resonances in the mass spectrum are being looked for, as this could point to the existence of a new dark matter mediator. If the dark matter particles couple to quarks via a dark matter mediator, this mediator can either decay to a pair of dark matter particles or a pair of Standard model quarks which can be observed as a pair of jets. Finally, for some particular types of dark matter candidates, such as strongly interacting massive particles (SIMPs) [74] or heavy stable neutral particles (HSCPs) [75, 76], more unusual signatures are expected. This is currently a developing area of dark matter research, and more and more searches looking for new signatures are appearing.

In Figures 2.8 and 2.9, recent limits from dark matter searches at the CMS experiment are compared to the direct detection results, for spin-dependent and spin-independent interactions, respectively.

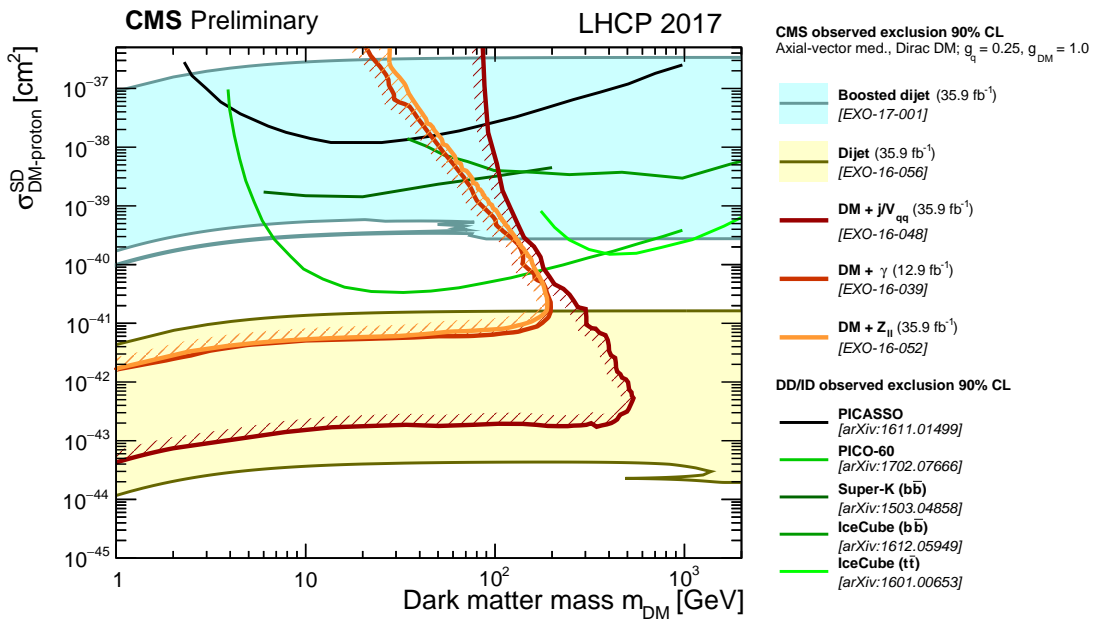


Figure 2.8: A comparison of CMS results to direct detection experiments in the $m_{\text{DM}} - \sigma_{\text{SD}}$ plane. The limits are shown at 90% CL. The shown CMS contours are for an axial-vector mediator with Dirac dark matter and couplings $g_q = 0.25$ and $g_{\text{DM}} = 1.0$. The spin-dependent exclusion contours are compared with limits from the PICASSO and PICO experiments, the IceCube limit for the $t\bar{t}$ and $b\bar{b}$ annihilation channels, and the Super-Kamiokande limit for the $b\bar{b}$ annihilation channel. It should be noted that the CMS limits do not include a constraint on the relic density and also the absolute exclusion of the different CMS searches as well as their relative importance will strongly depend on the chosen coupling and model scenario. Therefore, the shown CMS exclusion regions in this plot are not applicable to other choices of coupling values or models. Figure taken from [77].

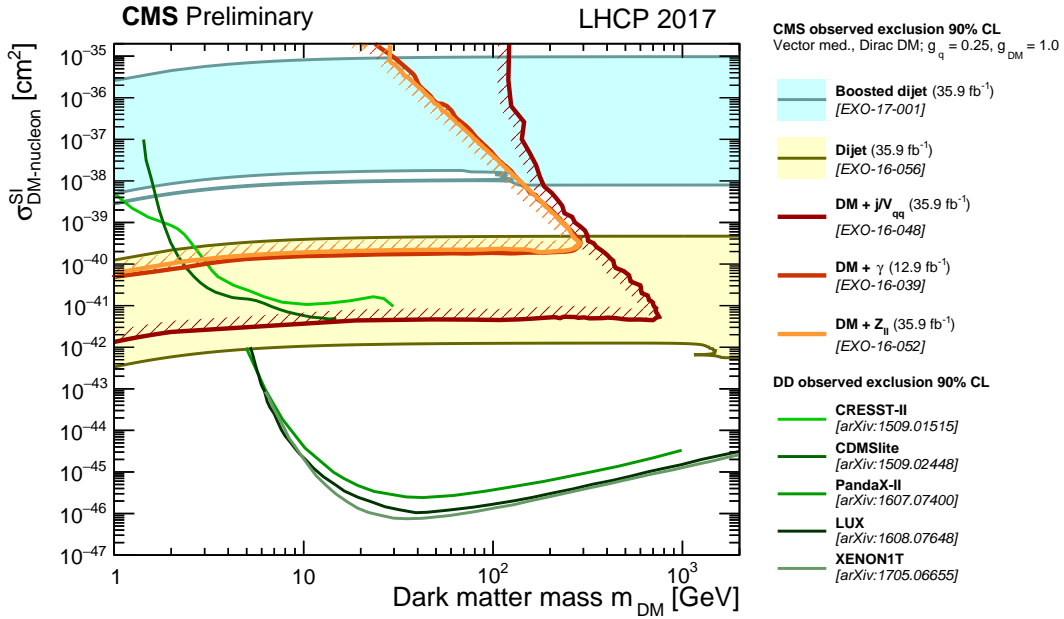


Figure 2.9: A comparison of CMS results to direct detection experiments in the $m_{\text{DM}} - \sigma_{\text{SI}}$ plane. The limits are shown at 90% CL. The shown CMS contours are for a vector mediator with Dirac dark matter and couplings $g_q = 0.25$ and $g_{\text{DM}} = 1.0$. The spin-independent exclusion contours are compared with the XENON1T 2017, LUX 2016, PandaX-II 2016, CDMSlite 2015 and CRESST-II 2015 limits, which constitutes the strongest documented constraints in the shown mass range. It should be noted that the CMS limits do not include a constraint on the relic density and also the absolute exclusion of the different CMS searches as well as their relative importance will strongly depend on the chosen coupling and model scenario. Therefore, the shown CMS exclusion regions in this plot are not applicable to other choices of coupling values or models. Figure taken from [77].

2.2.4 From EFTs to simplified models

In order to efficiently look for dark matter at colliders, effective field theories (EFTs) have been used extensively to model the dark matter signal. The EFT models assume the dark matter production can be described as a contact interaction defined by an effective mass scale and coupling structure. This contact interaction is for example illustrated in Figure 2.10 for the monojet final state where the dark matter pair is produced in association with an initial state radiation jet. The resulting signal models can then be classified by coupling structure, and the effective scale Λ can be extracted for a specific model, defining both the coupling strength and the scale of the theory. An EFT is characterized by a total of 3 parameters, the dark matter mass, the EFT scale, and the EFT coupling structure. However, this approach has several limitations [78–80]. First, it implicitly assumes that the dark matter production happens through a heavy mediator, which is not resonantly enhanced at the LHC. Additionally, for low enough effective scales, the EFT breaks down. Finally, the incompleteness of the EFT makes a comparison with direct detection experiments difficult or inconsistent. Due to the limitations of EFTs, there has been a trend in the past few years to instead use simplified models which allow for a fair comparison to low energy underground direct detection experiments. In a simplified model the effective scale is then replaced by a physical mediator. The resulting models contain six parameters that can be scanned to search for dark matter, namely the coupling structure, the dark matter mass, the mediator scale, the couplings to the Standard Model and the dark matter, and the mediator width. This transition has been overseen by the joint ATLAS/CMS dark matter forum [81] by establishing a well defined set of benchmark models to enable the combination of different channels and the recasting of dark matter models against direct and indirect detection searches.

In the two dark matter searches covered in this thesis, the results have been interpreted in terms of simplified models. The monojet search described in Chapter 5 includes several simplified models recommended by the dark matter forum. Four types of mediators are considered, i.e. a vector, axial, scalar, and

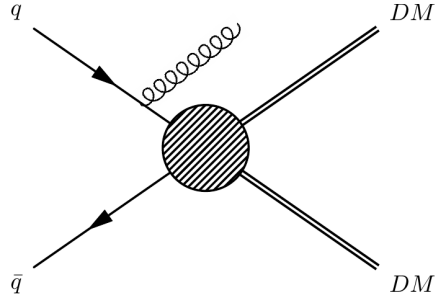


Figure 2.10: Illustration of EFT dark matter production in the monojet final state.

1 pseudoscalar mediator. In the case of a scalar or pseudoscalar coupling, the production mode is domi-
 2 nated by gluon fusion. As illustrated in the right diagram of Figure 2.11, the scalar is produced through
 3 a t or b quark loop. A Yukawa coupling is assumed for the coupling of the mediator to Standard Model
 4 particles, proportional to the mass of the particle. For a vector or axial mediator, the production happens
 5 through the fusion of two quarks into a heavy mediator, similarly to the Z and W boson production.
 6 The coupling to quarks and potentially leptons is taken to be unity, and universal for all flavours. For all
 7 mediator types, the coupling to the dark matter particles is assumed to be unity. In addition, the minimal
 8 width assumption is made, implying that the mediator couples to all Standard Model and the dark matter
 9 particle and no extra particles are introduced. If such particles would be present, the width would increase
 10 and the sensitivity of the analysis would be reduced. A scan is then performed over the mass of the dark
 11 matter candidate and the mass of the mediator.

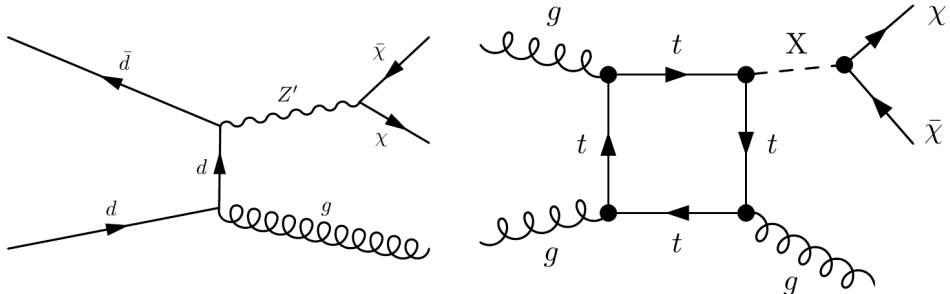


Figure 2.11: The vector (left) and scalar (right) production diagrams in the monojet final state.

12 staat enkel in de AN, niet in de PAS... Furthermore, some non-standard dark matter models are inves-
 13 tigated as well in the monojet analysis, namely a complete simplified scalar model, known as the inert two
 14 Higgs doublet model and a baryon number violating dark matter model which can explain electroweak
 15 baryogenesis [82,83], known as non-thermal dark matter. In contrast to the simplified models, these theo-
 16 ries are completed theories. The first consists of an extended scalar field theory, while the second consists
 17 of resonant production induced by flavour changing neutral currents.

18 The SIMP simplified model on which the trackless jets analysis detailed in Chapter 6 is a specific
 19 simplified model which is not part of the models recommended by the dark matter forum. It is described
 20 in more detail in Section 2.3.

21 **2.3 Strongly Interacting Massive Particles**

22 As no observation of dark matter has been made so far, despite many searches probing the more popular
 23 models described in the previous section, many scenarios now venture beyond minimal models or give up
 24 basic assumptions for the WIMP. In the following model, which is studied in this thesis, the interaction
 25 cross section of the dark matter with normal matter is so high that the particles are no longer WIMPs, but

so-called strongly interacting massive particles (SIMPs). This model can also be motivated by the long lasting interest for self-interacting dark matter (SIDM)⁴ particles with a large cross section [42], which could help to explain observations that present a challenge for the cold dark matter scenarios, such as the missing satellites or core-cusp problems [84–87]. While it is possible to create models with a strongly interacting hidden sector that is weakly coupled to the Standard Model particles, SIDM particles that interact rather strongly with the known matter particles can be considered as well.

2.3.1 The SIMP simplified model

In this simplified model, the dark matter particles χ can be produced at the LHC in pairs, through a new strong interaction with a new mediator ϕ , as illustrated in Figure 2.12. These SIMPs are neutral and stable, and are generated off-shell as the mediator is very light, of the order of the pion mass: $m_\phi = 140$ MeV. We only consider the case of fermionic candidates, since the bosonic form is ruled out by constraints coming from neutron stars and black holes, as is described in Section 2.3.2. Both the cases with a scalar or a vector mediator can be studied, and the corresponding interaction Lagrangian is

$$\mathcal{L}_{\text{int}} = \begin{cases} -g_\chi \phi \bar{\chi} \chi - g_q \phi \bar{q} q & \text{(scalar mediator)} \\ -\tilde{g}_\chi \phi_\mu \bar{\chi} \gamma^\mu \chi - \tilde{g}_q \phi_\mu \bar{q} \gamma^\mu q & \text{(vector mediator)} \end{cases} \quad (2.17)$$

with $g_\chi g_q, \tilde{g}_\chi \tilde{g}_q < 0$ to avoid the formation of bound states. For simplicity we assume that the SIMPs have a universal coupling to quarks, although a flavour dependent coupling could be preferred, as light SIMPs with a significant coupling to b or c quarks are probably constrained by B and D meson phenomenology. SIMPs lighter than about 5 GeV could for example appear in the decay of b or c quarks, and would be constrained by limits on the invisible decay of B and D mesons.

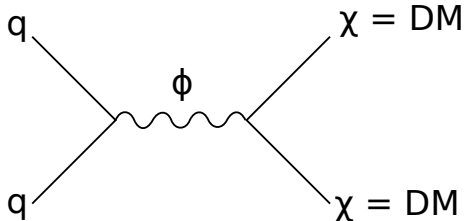


Figure 2.12: Feynman diagram showing the production of a SIMP pair, through a new low-mass mediator.

Introducing a new strong interaction between quarks can however modify nuclear potentials. In order to keep the impact small, the mediator is assumed to not modify nuclear potentials by more than $\mathcal{O}(10\%)$, such that $g_{\chi N} \lesssim 0.3 g_{\pi NN} \sim 3$ for a mediator with the mass of a pion, where $g_{\pi NN} \sim 13$ is the effective pseudoscalar pion-nucleon coupling [88]. The quoted values are however not very precise, as a large spread of values can be found in the literature for meson-nucleon effective couplings, sometimes differing by a factor 2 or more (see e.g. [89] for comparison). This shows the difficulty of dealing with strong interactions in the framework of effective field theories, which arise because contributions from many mesons need to be taken into account, each of them with a different coupling. No constraints on modified strong interactions at low energies seem to exist in literature so far, however searches at fixed-target experiments do place constraints on the existence of strongly interacting stable neutral particles.

In summary, the model has 4 free parameters: the two couplings, the mass of the mediator m_ϕ , and the mass of the SIMP m_χ . At the LHC, only the product of the couplings appears, while astrophysical observations constrain both the dark matter self-interaction and the interaction with the Standard Model.

⁴Incidentally, self-interacting and strongly interacting share the same abbreviation, such that SIDM can also stand for strongly interacting dark matter and SIMP for self-interacting massive particles in the literature.

2.3.2 Experimental constraints

Naively, one would expect such an unusual model with strong interactions not to be viable, as various types of experiments and observations set constraints on SIMPs as dark matter candidates. However, some of these limitations can be avoided by the assumptions in the model described above. The relevant existing measurements are described below, showing there is still a part of phase space which remained unexplored so far.

7 Bound states

Searches for heavy isotopes, in particular heavy water, constrain the formation of bound states between SIMPs and nucleons, ruling out particles with a mass below 10 TeV for the scenario with SIMPs as dominant contribution to dark matter. This constraint is evaded by assuming a purely repulsive SIMP-nucleon interaction with opposite sign couplings, as is specified in the Lagrangian (2.17). In the vector mediator case, vector mediators would however couple to the dark matter antiparticles with an opposite charge. This is avoided if no dark matter antiparticles are around, i.e. if the abundance of dark matter is asymmetric. A reason for having asymmetric SIMPs is that if they are the dominant source of dark matter, then the dark matter abundance is set by either an asymmetry or through a non-thermal mechanism. In the case of a symmetric SIMP candidate, the dark matter abundance is determined by thermal freeze-out, and it can only be a sub-dominant component. Additional constraints also exist on the dark matter self-interacting strength from halo shapes and merging galaxies such as the Bullet cluster [90, 91].

20 Earth heating

A second argument for an asymmetric abundance of SIMPs comes from experiments measuring the heat emitted from the Earth's core. For the typical SIMPs cross sections, the dark matter particles can be captured by the Earth and accumulate in its core over time. Annihilating SIMPs would then provide a substantial source of heat and could modify the Earth's heat flow. This can be measured by detectors in deep underground shafts [92] and rules out the scenario with symmetric SIMPs.

26 Neutron stars and black holes

In the asymmetric scenario, light scalar dark matter particles can however be collected in the cores of neutron stars and cause them to collapse into black holes. Bosonic dark matter candidates are therefore excluded, and we consider only fermionic candidates as mentioned previously.

30 Direct detection searches

Many bounds on the SIMP parameter space also come from the direct detection searches. Underground experiments, such as CDMS and XENON, place strong constraints at smaller cross sections, about 5 orders of magnitude below the SIMP cross section, as can be seen from Figure 2.13. At the higher cross sections considered here, the SIMPs are stopped by the Earth's atmosphere, and they cannot reach the underground detectors. At higher altitudes however, space or airborne experiments such as RSS [93], a balloon-based experiment with a silicon semiconductor detector, and XQC [94], a sounding rocket experiment, exclude SIMPs in some regions of phase space. More details on these constraints can be found in [92], where they have been extensively reviewed.

39 Nucleosynthesis and cosmic rays

There are also bounds from primordial nucleosynthesis and cosmic rays, reviewed in [95] and [96]. The protons in cosmic rays can scatter off dark matter particles and create neutral pions, which decay to photons and could be detected in gamma ray telescopes. Although limits have been placed on dark matter-nucleon interactions [96], these constraints depend on many assumptions and adopt a form of the dark matter density near the galactic core. Since the considered model describes a nonstandard form of dark matter with a relatively strong interaction with baryons, these densities may be considerably different.

47 CMB and large scale structure

Observations of the CMB anisotropies and the large scale structure power spectrum, including from

the Lyman- α data [97, 98] additionally also place strong constraints on interactions between dark matter and baryons.

Fixed-target experiments

Finally, a relatively old fixed-target experiment led in 1976 at FNAL with a beam of neutral particles produced by 300 GeV protons hitting a beryllium target was used to look for massive, strongly interacting, neutral particles [99]. The mass of the particles was determined using their flight time and their kinetic energy which was measured in a calorimeter. Neutral particles with a mass larger than 2 GeV were searched for, in order to discriminate the candidates from the background of neutrons and lighter hadronic states, up to $m_\chi \lesssim \sqrt{E/2} \approx 12$ GeV, limited by the beam energy of $E = 300$ GeV. Single particle production was considered, but the results apply to pair production as well when they are translated into the case where 2 neutral particles are boosted and fly away in the same direction. The search showed no significant excess above the expected background and limits were placed on the invariant production cross section per nucleon versus the neutral particle interaction cross section. As an example, for an interaction cross section of 1 mb, a limit on the total production cross section of about 2.5×10^{-35} cm 2 = 25 pb is found, and this limit is reported by the Particle Data Group [100]. Comparing the considered SIMP model to this result by simulating the pair production at $\sqrt{s} = 25$ GeV, one can conclude that SIMPs between 2 and about 6 GeV are already excluded by this experiment [101].

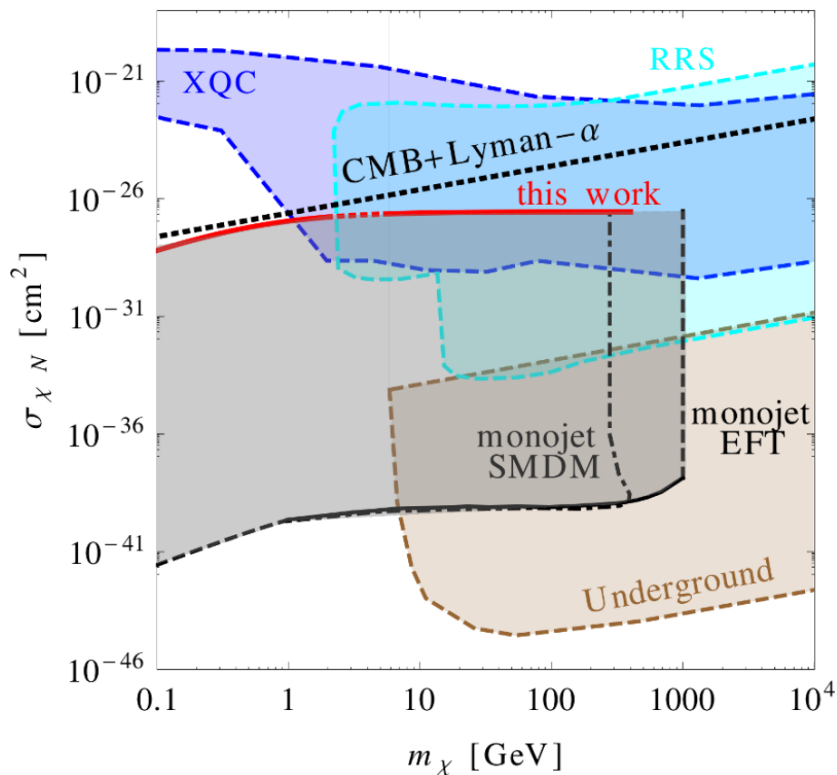


Figure 2.13: Summary plot showing the SIMP model (red) in comparison with the most important applicable constraints, coming from the LHC monojet analyses (black), the atmospheric XQC and RRS experiments (blue), underground experiments (brown), and the CMB observations and Lyman- α data (black dashed line). Figure taken from [101].

3

The LHC and the CMS Detector

In order to investigate the currently unsolved mysteries of particle physics, such as the existence of dark matter, many experiments can be conducted, among other things at particle colliders. The largest particle accelerator in the world is the LHC, located at the European Organization for Nuclear Research (CERN) in Geneva, Switzerland. At this accelerator, protons are being accelerated at energies up to 6.5 TeV, giving rise to a record centre-of-mass energy of 13 TeV in the proton collisions. Using data from the collisions generated at the interaction points along the accelerator ring, the Standard Model can be tested in many ways and searches for particles beyond the Standard Model can be performed.

In Section 3.1 more details are given about the LHC and the 4 main experiments situated at the interaction points. In particular, the general-purpose Compact Muon Solenoid (CMS) detector is described in Section 3.2.

3.1 The Large Hadron Collider at CERN

The LHC was built in the already existing Large Electron Positron (LEP) collider tunnel, which was excavated in the 1980's and has a circumference of 27.6 km. Contrary to the LEP collider, the LHC accelerates particles of the same charge, namely protons or lead ions. Much higher luminosities can therefore be reached, since only particles are used and the generation of antiparticles is not needed. This was the limiting factor at the Tevatron, where protons and antiprotons were used. Additionally, at the probed energies the colliding particles are not the protons or ions, but their constituents, which carry a varying fraction of the total momentum. This makes the LHC an ideal instrument for exploration at higher energies, as the collisions naturally cover a wide energy range.

3.1.1 The LHC injector chain

The protons (or lead ions) can not directly be injected in the LHC, but need to be accelerated gradually in several pre-accelerators, as illustrated in Figure 3.1. For the proton beams, the LHC injection chain starts at a bottle of hydrogen, where protons are stripped from the hydrogen atoms and accelerated up to 50 MeV by a linear accelerator (LINAC2). The protons are then transferred to a chain of circular accelerators, starting with the Proton Synchrotron Booster (PSB) which accelerates them to an energy of 1.4 GeV. Next, the protons go through the Proton Synchrotron (PS) and are delivered to the Super Proton Synchrotron (SPS) at an energy of 26 GeV. Finally, the protons are injected in the LHC in opposite direction with an energy of 450 GeV.

The lead ions are first accelerated in a different linear accelerator, LINAC3, before being injected in the Low Energy Ion Ring (LEIR) at an energy of 4.5 MeV per nucleon. Here the ions are accelerated

1 to an energy of 72 MeV per nucleon, and they then follow the same path as the protons through the PS,
 2 where they are accelerated to 5.9 GeV and stripped from the last of their electrons, and the SPS, where
 3 they are accelerated to 177 GeV. The record centre-of-mass energy for heavy ion collisions at the LHC
 4 so far has been 5.02 TeV and 8.16 TeV, for lead-lead (Pb-Pb) and proton-lead (p-Pb) collisions in 2015
 5 and 2016, respectively.

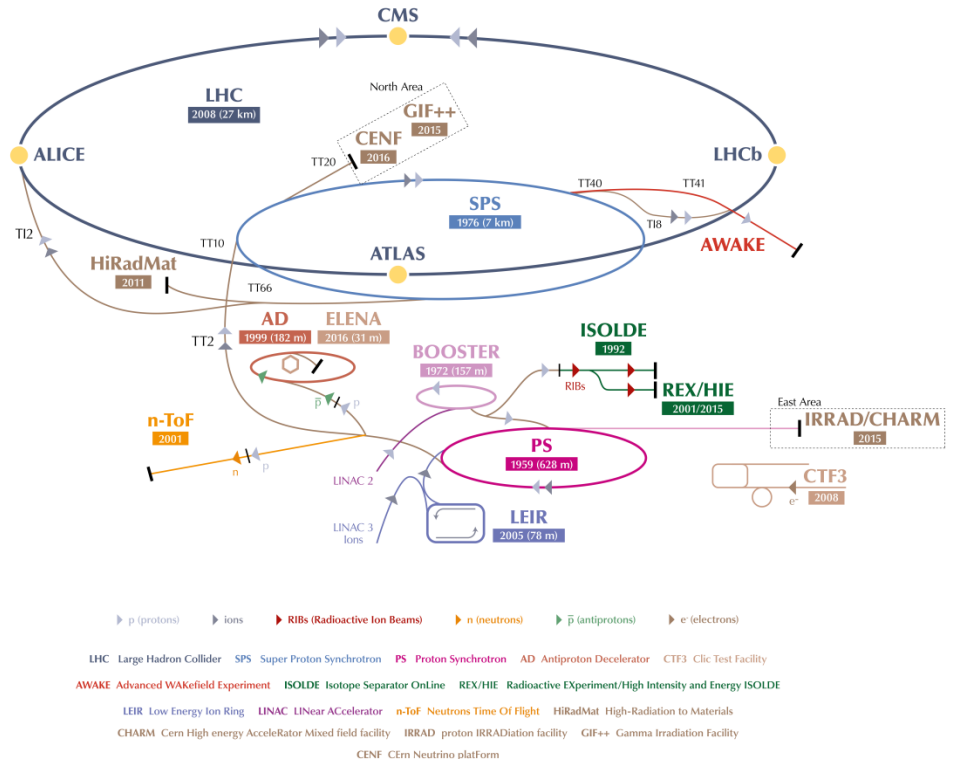


Figure 3.1: Schematic view of the various linear and circular accelerators of the CERN accelerator complex, including the LHC injection chain. Figure taken from [102].

6 3.1.2 The Large Hadron Collider

7 The most relevant specifications for a particle physics accelerator are the maximum energy and the lumi-
8 nosity that can be reached. High energy is necessary in order to be able to create new heavy particles,
9 which are for example predicted in many theories beyond the Standard Model.

The protons are kept on the correct orbit by the 1232 LHC dipole magnets. These magnets are cooled down to 1.9 K with liquid Helium and supplied with a current of 12 kA to reach the design field of 8.33 T. This limits the maximum beam momentum of the accelerator to

$$p = B/\rho = 8.33 \text{ T}/2804 \text{ m} = 7 \text{ TeV/c}, \quad (3.1)$$

¹³ with ρ the bending radius of the tunnel. The protons are accelerated up to the desired energy by radio-
¹⁴ frequency (RF) cavities, which produce an oscillating electric field.

15 A high event rate or luminosity \mathcal{L} is equally important, to obtain a sufficiently high number of collisions.
 16 For a process with cross section σ , this rate is

$$\frac{dN}{dt} = \mathcal{L}\sigma. \quad (3.2)$$

In order to achieve the high design luminosity of $10^{34} \text{ cm}^{-2}\text{s}^{-1}$ in the LHC, the protons are concentrated in bunches which are focused by strong quadrupole magnets around the interaction regions. The RF

frequency is 400 MHz, which corresponds to a wavelength of 75 cm and confines the protons into buckets of 2.5 ns. The LHC circumference would then allow for 35640 buckets in total, which would result in bunch crossings spaced by only 37.5 cm. A more realistic spacing is 25 ns, corresponding to one bunch per 10 RF buckets. Additionally, 225 ns gaps are present between the bunch trains, corresponding to the rise time of the injection kicker magnets. One gap of 3 μ s is necessary as well to allow clean beam dumps. These requirements limit the number of bunches to a maximum of 2808.

After almost 25 years of design and construction, the LHC was completed in 2008 and the commissioning of the machine started. However, during a powering test on 19 September of the same year an electric arc developed inside a bus bar which led to a large release of helium and a pressure wave that caused extensive mechanical damage to the affected LHC sector. This incident delayed the first collisions, with one bunch per beam and at a beam energy of 900 GeV, until late 2009. During 2010 and 2011 a centre-of-mass energy of 7 TeV was used for the collisions, which was then increased to 8 TeV in 2012. The instantaneous luminosity was also increased, starting from $2 \times 10^{32} \text{ cm}^{-2}\text{s}^{-1}$ in 2010 to more than $6 \times 10^{33} \text{ cm}^{-2}\text{s}^{-1}$ in 2012. During the 3 years of data-taking in Run 1, data corresponding to an integrated luminosity of 45.0 pb^{-1} , 6.1 fb^{-1} , and 23.3 fb^{-1} , respectively, were delivered. After Run 1, a long shutdown (LS1) of 2 years followed, which was used to correct the problems that were discovered in the aftermath of the incident at the startup in 2008, and to upgrade and consolidate the experiments located on the LHC ring.

In 2015, the LHC restarted operations with Run 2, at an even higher centre-of-mass energy of 13 TeV. During 2016 the design luminosity of $10^{34} \text{ cm}^{-2}\text{s}^{-1}$ was exceeded and a total of 41 fb^{-1} of data were delivered. A comparison of the delivered integrated luminosity per year is shown in Figure 3.2.

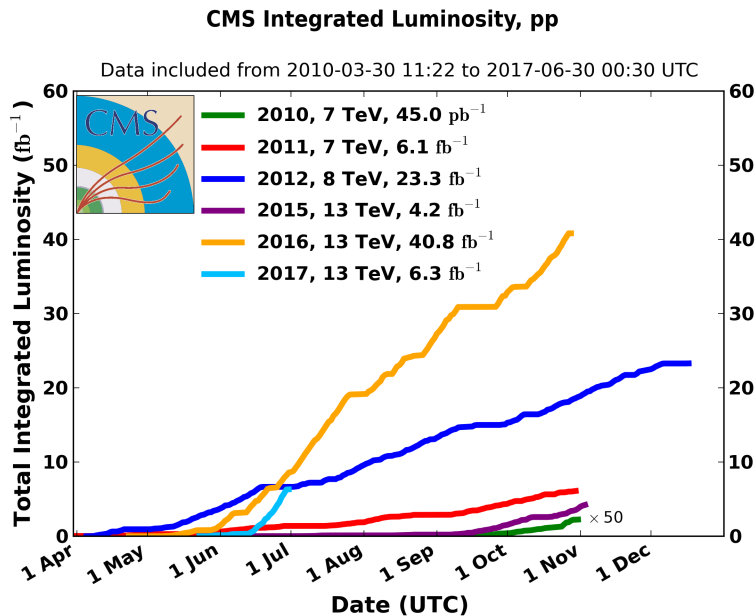


Figure 3.2: Overview of the integrated luminosity delivered to the CMS detector during Run 1 (2010 to 2012) and Run 2 (2015 to 2017).

3.1.3 The experiments at the LHC

There are four interaction points (IPs) where the proton or lead ion beams of the LHC can collide, and around each of these points large particle detectors were built in order to record the generated collisions. The ATLAS and CMS detectors, located at IP1 and IP5, are both high luminosity general-purpose detectors and consist of several layers surrounding the IP in an onion-like structure to avoid particles escaping detection. These detectors can cover a wide range of high energy physics, from precision measurements of the Standard Model to searches beyond the Standard Model. At IP2 the ALICE detector is specialized in heavy ion collisions with low instantaneous luminosities, around $10^{27} \text{ cm}^{-2}\text{s}^{-1}$. With

this detector information is gathered about the quark-gluon plasma, a state of matter that exists at extremely high temperatures and densities where quarks and gluons are no longer confined in hadrons. The fourth main detector, LHCb, is located at IP8 and requires instantaneous luminosities of the order of a few $10^{32} \text{ cm}^{-2} \text{ s}^{-1}$. Using this detector b quarks are being studied, focusing among other things on the matter-antimatter asymmetry in the universe.

3.2 The CMS detector

The searches described in this thesis were conducted using data collected with the CMS detector, a general-purpose detector located on the LHC ring. It consists of the typical components of a particle physics detector, namely a tracker, an electromagnetic calorimeter (ECAL), a hadronic calorimeter (HCAL), a solenoidal magnet, and muon detectors. One peculiar aspect is however that both calorimeters are situated inside the superconducting magnet. This design was chosen in order to improve the energy resolution by reducing the amount of material in front of the calorimeters. The overall detector has a length of 21.6 m, a diameter of 14.6 m and a total weight of 12500 t. A schematic overview is shown in Figure 3.3.

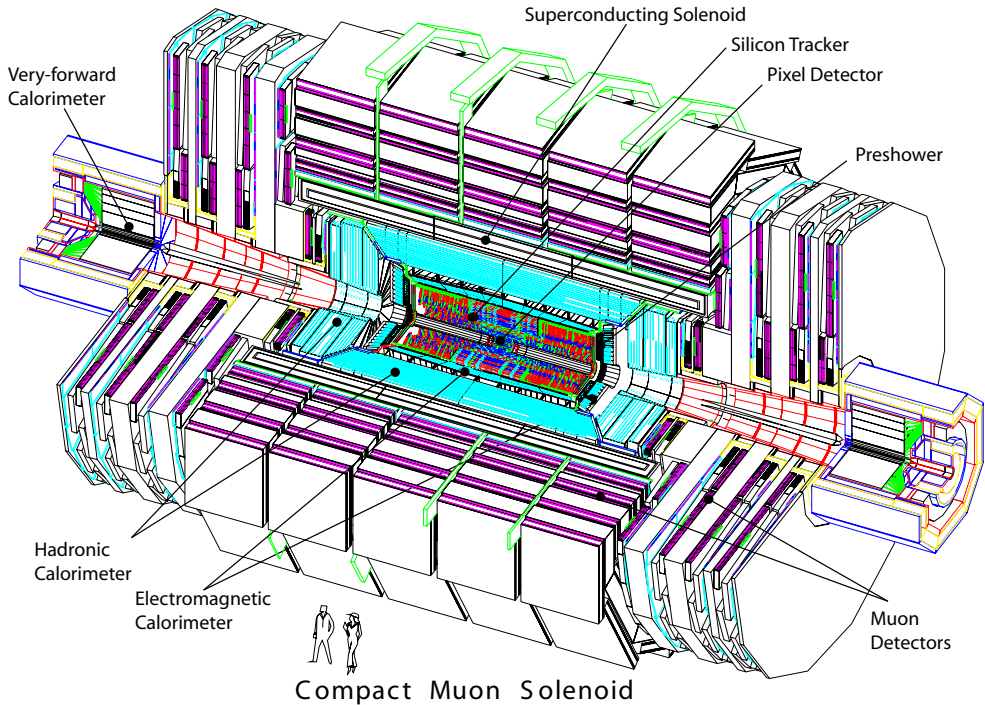


Figure 3.3: The CMS detector, consisting of the pixel and strip tracker, the electromagnetic calorimeter (ECAL) with preshower, the hadronic calorimeter (HCAL) with its forward component, and the muon systems. Figure taken from [103].

The CMS coordinate system places the origin at the nominal collision point. The x axis is perpendicular to the beam and points towards the centre of the LHC ring, the y axis is vertical and pointing upwards, and the z axis is defined anticlockwise along the beam direction. The azimuthal angle ϕ is then defined in the xy plane, relative to the x axis and the polar angle θ is measured with respect to the z axis. In general, the polar angle is converted into the pseudorapidity

$$\eta = -\ln \left(\tan \frac{\theta}{2} \right) \quad (3.3)$$

for convenience, since differences in pseudorapidity are invariant under Lorentz boosts along the z axis. A pseudorapidity of 0 corresponds to the direction perpendicular to the beam ($\theta = \pi/2$), and an infinite pseudorapidity corresponds to the direction parallel to the beam ($\theta = 0$).

1 Due to the conservation of momentum before and after the collision, the momenta of the particles in
 2 the final state of a collision should be balanced in the transverse plane. Another variable that is therefore
 3 often used in particle physics is the transverse momentum of a particle, defined as

$$p_T = p \cdot \sin \theta. \quad (3.4)$$

4 **3.2.1 The tracker**

5 The innermost part of the CMS detector, closest to the IP, is the tracking system, which is designed to
 6 provide a precise measurement of the trajectories of charged particles. This all-silicon detector is divided
 7 into a pixel and a strip detector, with a layout as shown in Figure 3.4. The inner part, consisting of pixel
 8 modules, provides very precise 3D hits, which are important for vertex reconstruction and track seeding.
 9 This allows to have a precise measurement of secondary vertices and track impact parameters, necessary
 10 for the efficient identification of e.g. heavy flavour particles. As the hit occupancy is lower in the outer
 11 part of the detector, a larger cell size can be afforded, and silicon strips are used instead of pixels. This
 12 strip detector provides a large lever arm and a link to the calorimeters and the muon system. The tracker
 13 covers a pseudorapidity range $|\eta| < 2.5$.

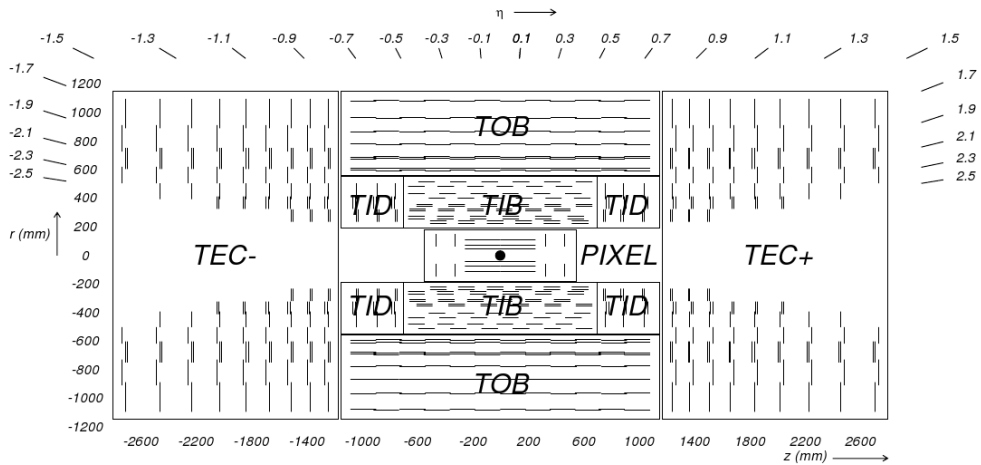


Figure 3.4: A transverse view of the pixel and strip tracker detectors. Figure taken from [103].

14 **3.2.1.1 The pixel tracker**

15 The pixel tracker was replaced during the extended technical stop in 2016 and 2017 [104], as a part of
 16 the CMS Phase 1 upgrades. As the data used for this thesis were recorded before that, only the so-called
 17 Phase 0 detector is described here.

18 For the pixel modules n+ pixels on n-substrate are used, allowing the sensors to also work in under-
 19 depletion after type inversion. The 1440 modules are arranged in several cylindrical layers and disks, as
 20 illustrated in Figure 3.4. The barrel, consisting of 3 pixel layers surrounding the beam pipe at radii of 4.4,
 21 7.3 and 10.2 cm, is complemented by the forward pixel detector, composed of 2 endcap disks on each
 22 side extending from 6 to 15 cm in radius. The barrel and the forward parts contain respectively 48 million
 23 and 18 million pixels with a size of $100 \times 150 \mu\text{m}^2$, covering a total area of 1.06 m^2 .

24 In the barrel, the magnetic field of CMS is perpendicular to the drift of the electrons to the collecting
 25 pixels, which results in a Lorentz drift. This drift leads to a spread of the charge over several pixels.
 26 Since the read-out of the modules is analogue, an improved spatial resolution can therefore be achieved
 27 with charge interpolation. In the forward pixel detector the drift of the electrons would be parallel to the
 28 magnetic field so in order to profit from the Lorentz angle, the modules are tilted by 20° in a turbine-
 29 like arrangement, as can be seen in Figure 3.5. A spatial resolution of $10 \mu\text{m}$ ($30 \mu\text{m}$) can be achieved
 30 in the local directions x (y) of the module, respectively. In the barrel x is the longitudinal direction
 31 perpendicular to the beam and y is the longitudinal direction parallel to the beam.

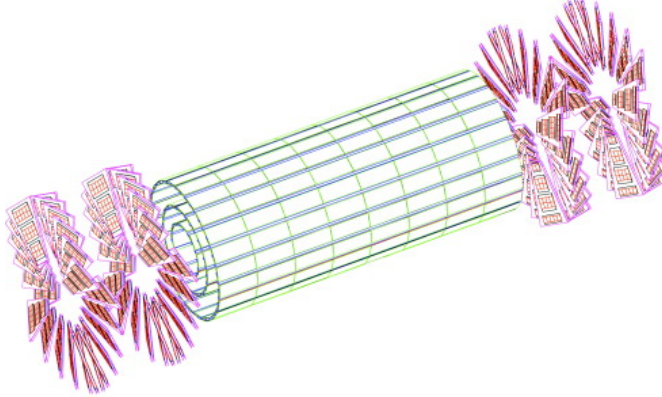


Figure 3.5: A 3D view of the barrel and forward pixel detector. Figure taken from [105].

1 The signals from the pixel sensors are read out by custom read-out chips (ROCs), which amplify
 2 and store the signals, and already apply zero-suppression on-detector. The data rate from the detector
 3 to the Front End Drivers (FEDs) is therefore not constant for every event. Additionally, if there are
 4 too many hits on a pixel module for a given event, they can not all be stored on the finite buffer of the
 5 ROC. Consequently, as the instantaneous luminosity increases the pixel modules start to show a “dynamic
 6 inefficiency” which is most pronounced in the first layer, closest to the beampipe. This was one of the
 7 main motivations for the Phase 1 upgrade of the pixel detector.

8 **3.2.1.2 The strip tracker**

9 The outer part of the tracker consists of 15 148 strip modules, which are distributed among multiple
 10 barrel layers and endcap disks and make up a total active area of 198 m^2 . The inner part is composed of
 11 4 Tracker Inner Barrel (TIB) layers with 3 Tracker Inner Disks (TID) on each side. Surrounding these
 12 are 6 Tracker Outer Barrel (TOB) layers and the 2 Tracker EndCaps (TEC), which are composed of 9
 13 disks. This geometric arrangement is shown in Figure 3.4, with double lines to indicate back-to-back
 14 modules. These so-called double-sided modules are mounted with a stereo angle of 100 mrad to improve
 15 the 3D point resolution by providing a measurement of the z and r coordinate in the barrel and disks,
 16 respectively. The choice of strip pitches is driven by the two particle separation capability and two-hit
 17 resolution, and ranges from $80 \mu\text{m}$ to $205 \mu\text{m}$. The length of the strips varies from 63 mm to 117 mm,
 18 minimizing the occupancy and noise levels.

19 In the TOB and the 3 outermost rings of the TEC two silicon sensors are daisy chained, while single
 20 sensors are used in the inner part. This is done to limit the number of read-out channels, since the area
 21 that had to be instrumented is larger in the outer region. The larger cell size can be afforded due to the
 22 lower occupancy in the outer part. However, the noise of the sensors also increases with strip length, so
 23 thicker silicon sensors, $500 \mu\text{m}$ compared to $320 \mu\text{m}$ in the inner part, are used in order to collect more
 24 signal per traversing particle.

25 The strip sensors are single sided p-on-n type silicon. The signals from the sensors are amplified,
 26 shaped, and stored by 4 or 6 custom APV25 chips per module. When the trigger has made a positive
 27 decision, the analogue signals from two APV25 chips are multiplexed and sent to the FED boards in the
 28 service cavern via optical fibres, where they are converted to digital signals. The FEDs then perform
 29 pedestal and common mode subtraction as well as cluster finding. Additionally, the data is sparsified
 30 in these off-detector electronics, before being sent to the CMS central data acquisition (DAQ). Due to
 31 charge sharing, this analogue read-out scheme also results in an improved spatial resolution of 15 to 40
 32 μm , depending on the position of the modules and the strip pitch.

33 **3.2.2 The electromagnetic calorimeter**

34 Surrounding the tracker, the CMS electromagnetic calorimeter (ECAL) is designed to measure the en-
 35 ergy of photons and electrons. It is composed of 75 848 lead tungstate (PbWO_4) crystals arranged in a

1 cylindrical barrel and 2 endcaps. The barrel crystals measure $22 \times 22 \text{ mm}^2$ at the front face of crystal,
 2 and $26 \times 26 \text{ mm}^2$ at the rear face, which corresponds to approximately 0.0174×0.0174 in $\eta\phi$. The
 3 length of the crystal is 230 mm, corresponding to 25.8 radiation lengths. In the endcaps, the crystals have
 4 a rear face cross section of $30 \times 30 \text{ mm}^2$, front face cross section of $28.62 \times 28.62 \text{ mm}^2$, and a length of
 5 220 mm, corresponding to 24.7 radiation lengths.

6 The high density material was chosen due to its short radiation length and small Moli  re radius,
 7 resulting in a small spread of the electromagnetic shower generated by an incoming photon or electron.
 8 This allows for a fine granularity, a better shower separation, and a compact calorimeter. Additionally,
 9 this scintillating material has a fast response, as about 80% of the light is emitted during the first 25 ns.
 10 The scintillation light is collected by photodetectors, digitized, and read out.

11 The layout of the ECAL is shown in Figure 3.6, with the barrel (EB) extending up to $|\eta| < 1.470$
 12 and the endcaps (EE) on each side covering the range $1.479 < |\eta| < 3.0$. A preshower detector (ES)
 13 is positioned in front of the endcap crystals, covering the pseudorapidity range between $|\eta| = 1.653$
 14 and $|\eta| = 2.6$. This detector consists of a layer of lead which initiates an electromagnetic shower from
 15 incoming photons or electrons, and a layer of silicon sensors which measures the deposited energy. The
 16 main goal of this 20 cm thick detector is to discriminate between photons and neutral pions.

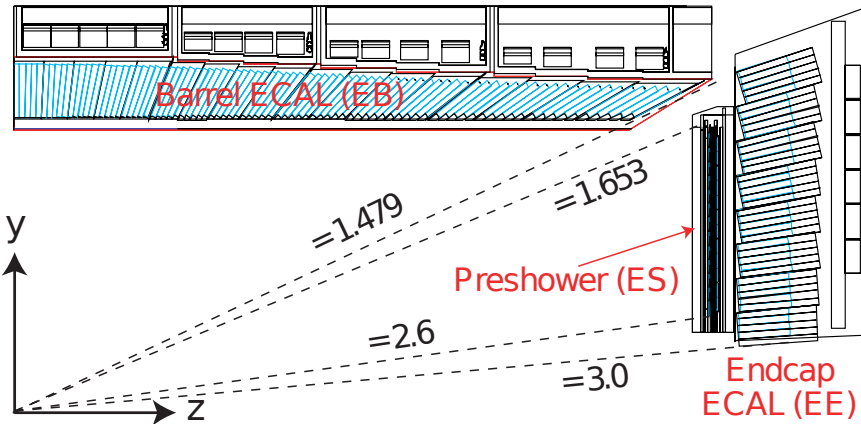


Figure 3.6: A transverse view parallel to the beamline showing one quarter of the ECAL, with its barrel (EB), endcap (EE), and preshower (ES) detectors. Figure taken from [105]

17 The energy resolution of calorimeters can be parametrized by the following stochastic (S), noise (N),
 18 and constant (C) terms:

$$\left(\frac{\sigma}{E}\right)^2 = \left(\frac{S}{\sqrt{E}}\right)^2 + \left(\frac{N}{E}\right)^2 + C^2 \quad (3.5)$$

19 The stochastic term represents contributions from the shower containment, the number of photoelectrons
 20 and the fluctuations in the gain process. The noise term takes into account all noise components, such as
 21 electronics and digitization noise. Finally, the constant term characterizes among others energy leakage
 22 from the back of the calorimeter crystals and non-uniformities of the longitudinal light collection. The
 23 latter term dominates the energy resolution for high-energy electron and photon showers. Figure 3.7
 24 shows the energy dependence of this resolution for incident electrons as measured in a beam test, as well
 25 as the determined stochastic, noise, and constant terms obtained by fitting equation 3.5 to the data.

26 A more recent measurement of the energy resolution was performed using electrons from Z boson
 27 decays in collision data. In the central region, up to $|\eta| < 0.8$, it was measured to be better than 2%. Out-
 28 side of this region, in the more forward direction, the energy resolution is 2-5% [106]. The reconstruction
 29 of the electrons and photons will be discussed in Section 4.3.2.

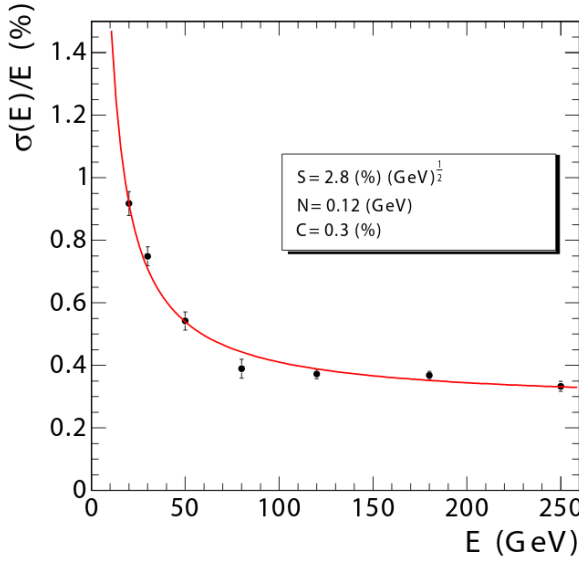


Figure 3.7: The ECAL energy resolution as a function of the electron energy, measured from a beam test. The stochastic (S), noise (N), and constant (C) are given as well. Figure taken from [103].

3.2.3 The hadronic calorimeter

The hadronic calorimeter (HCAL) surrounds the ECAL with the aim to measure the energy of charged and neutral hadrons. The missing transverse energy can then be inferred from this measurement together with the measured energy in the ECAL, in order to identify neutrinos or exotic particles. The HCAL consists of brass absorber plates interleaved with plastic scintillator tiles.

Figure 3.8 shows a longitudinal quarter view of the different HCAL components. A cylindrical barrel (HB) covers the region up to $|\eta| < 1.4$ and is complemented by endcaps (HE) on each side, extending the pseudorapidity range to $|\eta| < 3.0$. In the central region, the stopping power of the ECAL and HCAL barrel is not sufficient to contain the entire hadron showers. The HCAL was therefore extended outside the solenoid with an outer calorimeter (HO), which uses the magnet coil as absorber and consists of scintillators. Two layers are positioned at $\eta = 0$, where the absorber depth is minimal, and only 1 layer is used for the 2 rings on each side of the central ring. Finally, a forward calorimeter (HF) is positioned at 11.2 m from the IP covering $3.0 < |\eta| < 5.2$. Unlike the other HCAL components, this detector consists of iron and quartz fibres. Cherenkov-based, radiation-hard technology, since it is exposed to very large particle fluxes.

The optical signals from the scintillators in the HB and HE are converted to electrical signals by multichannel hybrid photodiodes, while silicon photomultipliers (SiPMs) are used in the HO. In the HF, the Cherenkov light emitted in the quartz fibres is detected by standard photomultiplier tubes (PMTs), since the magnetic field is much smaller in this region.

The expected transverse energy resolution for jets is shown in Figure 3.9 for various pseudorapidity regions: barrel jets ($|\eta| < 1.4$), endcap jets ($1.4 < |\eta| < 3.0$), and very forward jets ($3.0 < |\eta| < 5.0$). Details about the reconstruction of jets from calorimeter and tracking information will be given in Section 4.3.7.

3.2.4 The muon system

The outermost detector, located entirely on the outside of the solenoid, is a dedicated muon detection system. The purpose of this subsystem is muon identification, momentum measurement, and triggering. As illustrated in Figure 3.10, the layers of muon chambers are embedded in the iron yoke constraining the magnetic field lines. The strong magnetic field completely saturates the return yoke with a field of about 2 T, in opposite direction with respect to the field inside the magnet.

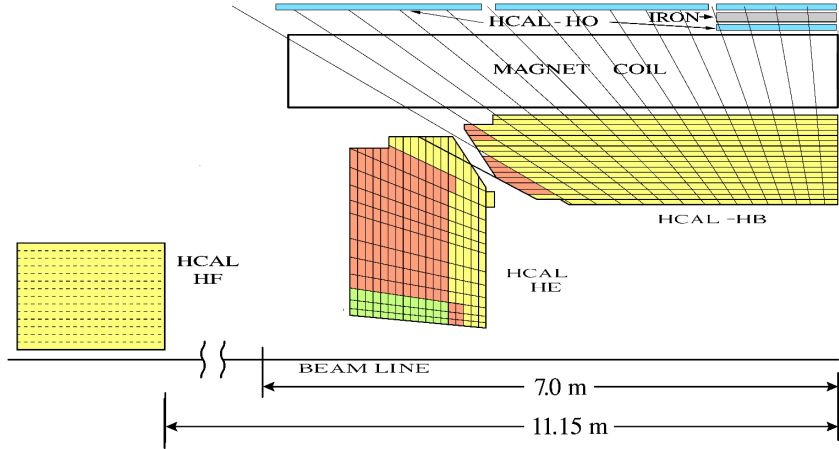


Figure 3.8: A quarter view of the hadronic calorimeter (HCAL), parallel to the beamline. The barrel (HB), endcap (HE), outer (HO), and forward (HF) detectors are indicated. Figure taken from [103].

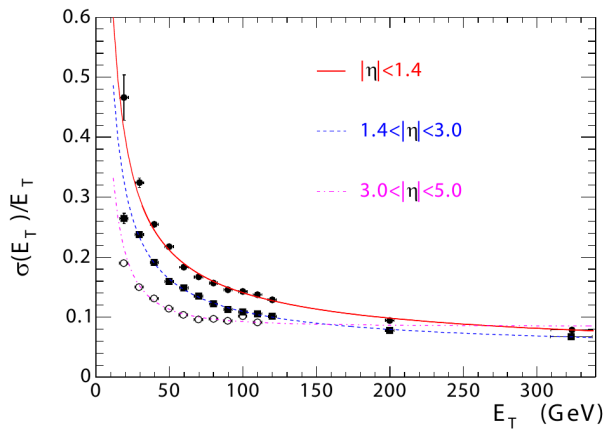


Figure 3.9: The jet transverse energy resolution as a function of the jet transverse energy, for barrel jets ($|\eta| < 1.4$), endcap jets ($1.4 < |\eta| < 3.0$), and very forward jets ($3.0 < |\eta| < 5.0$). Figure taken from [103].

1 Three different types of gaseous detectors are used. In the barrel, 4 layers of Drift Tubes (DT) are
 2 installed, covering the pseudorapidity range up to $|\eta| < 1.2$. Due to the higher flux and the larger and non-
 3 uniform magnetic field at larger pseudorapidities, Cathode Strip Chambers (CSC) are used in the endcap
 4 region ($0.9 < |\eta| < 2.4$). The DTs are designed for the low muon rates that are expected in the barrel
 5 and thus have a slower response time than the CSCs. Resistive Plate Chambers (RPCs) complement the
 6 DT and CSC systems in the pseudorapidity region up to $|\eta| < 1.8$. They provide a fast response, with a
 7 good time resolution but a worse spatial resolution than the DTs or CSCs. The RPCs are therefore very
 8 well suited to trigger on muons.

9 The offline reconstruction efficiency of simulated events containing one muon is typically between
 10 95% and 99%, except for the regions between 2 DT wheels ($|\eta| = 0.25$ and $|\eta| = 0.8$) and the transition
 11 region between the DTs and CSCs ($|\eta| = 1.2$), where the efficiency drops to 92%. The reconstruction of
 12 muons using the information from the tracker and the muon detectors will be detailed in Section 4.3.4.
 13 For low pseudorapidities and small momenta, the offline momentum resolution of the standalone muon
 14 system is about 9%. At momenta around 1 TeV, the resolution varies from 15% to 40%, depending on
 15 the pseudorapidity. As demonstrated in Figure 3.11, performing a global momentum fit using the tracker
 16 as well improves the resolution by an order of magnitude at low muon momenta. At high momenta the
 17 resolution of the full system is about 5%.

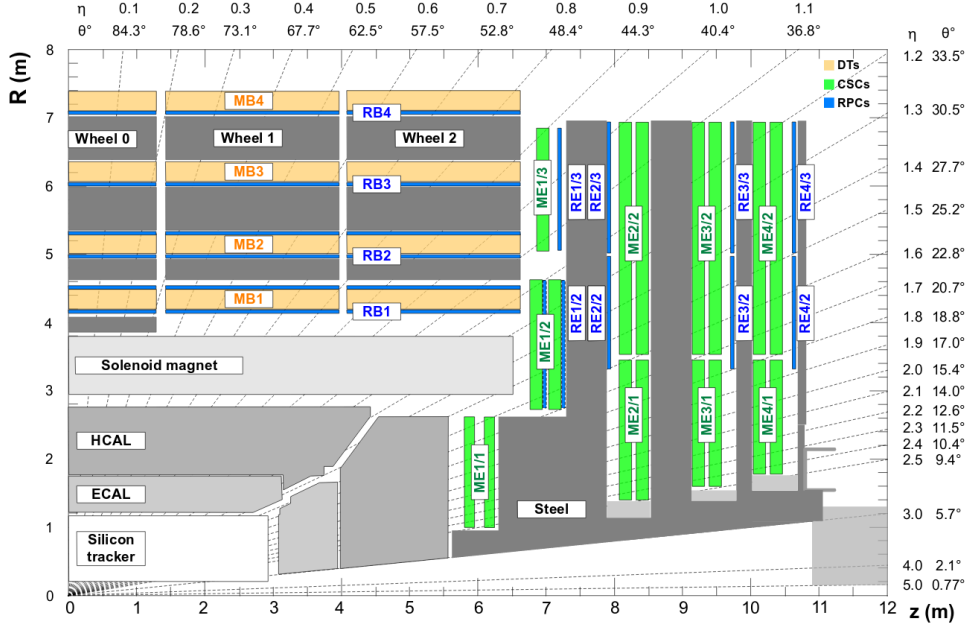


Figure 3.10: A transverse view of one quarter of CMS showing the position of the 3 types of muon detectors. The Drift Tubes (DT) are located in the barrel, the Cathode Strip Chambers (CSC) in the endcaps, and the Resistive Plate Chambers (RPC) in both regions up to $|\eta| < 1.8$. Figure taken from [107].

3.2.5 Trigger and data acquisition

Collisions are provided by the LHC at high interaction rates, with an interval of 25 ns between bunch crossings. This corresponds to a frequency of 40 MHz. Additionally, multiple collisions occur at the same time, depending on the luminosity. Since it is impossible to store and process the large amount of data produced in the collisions at this high rate, a severe rate reduction is needed. This rate reduction is performed by the trigger system, which decides whether to store or reject an event. Since this decision process is constrained in time, the computing time is optimized by rejecting uninteresting events as quickly as possible. The rate is reduced to 1 kHz in two steps by the Level-1 (L1) Trigger and the High-Level Trigger (HLT).

The L1 Trigger decision is based on information from the calorimeters and muon systems, following the structure illustrated in Figure 3.12. At the lowest level, the Local Triggers are based on energy deposits in calorimeter towers and track segments or hit patterns in the muon system. Regional triggers, indicated as Calo Trigger Layer 1 and Muon Track-Finder Layer in the figure, then combine this information and use pattern logic to determine trigger objects such as jet or muon candidates in separated spatial regions. The candidates are ranked based on their energy or momentum and quality, reflecting the level of confidence assigned to the L1 parameter measurements. Finally, the Calo Trigger Layer 2 and the Global Muon Trigger (GMT) determine the highest-rank calorimeter and muon objects across the whole detector and transfer them to the Global Trigger, which makes the final decision to accept or reject an event. Following this procedure, the L1 Trigger thresholds are tuned to reduce the event rate to 100 kHz. The L1 Trigger is composed of custom electronics located partially on the detectors, and partially in the underground service cavern. The L1 decision needs to be made and distributed to the detector front-end electronics within 3.8 μ s [108].

The readout of the data proceeds as illustrated in Figure 3.13. When an event is accepted by the L1 Trigger, the data from about 740 FEDs is read out by the Readout Units (RUs). For so-called *legacy* systems, i.e. systems which are using VME-based hardware from the initial installation, the FEDs are read out by custom Front-End-Readout-Link (FRL) cards, while for systems that changed their readout architecture from the VME standard to the newer μ TCA standard during or after LS1 they are read out via the newer Front-End-Readout-Optical-Link (FEROL) cards. The event fragments are then sent over

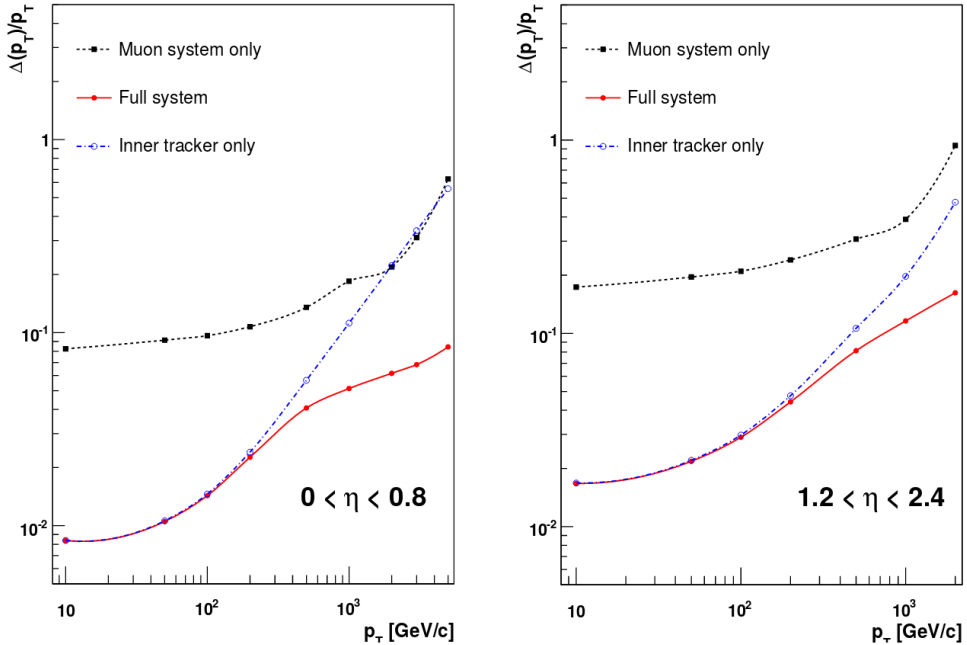


Figure 3.11: The muon transverse momentum resolution as a function of transverse momentum for low (left) and (high) pseudorapidities. The resolution is shown for the muon system and the tracker separately, and for the full system. Figure taken from [103].

the event-builder switch to the Builder Units (BUs), which assemble the events. Next, the events are distributed to the Filter Units (FUs) by a large switch network.

The HLT software system is implemented in this filter farm, which uses more than 15000 CPU cores for the final event selection. In this second step, the HLT reduces the event rate further to 1 kHz. The complete read-out data, including information from the pixel and strip tracker, are available for this step. New objects can therefore be reconstructed such as e.g. tau leptons and b-jets, as is done in the offline software, but speed-optimized.

3.2.6 CMS performance in Run 2

The number of collisions recorded at the experiments will differ from the amount delivered by the LHC. Data loss can be caused by e.g. problems with a particular subdetector, the trigger rate, the data acquisition, or the infrastructure. During Run 2, CMS achieved a data taking efficiency of 89% and 92% in 2015 and 2016, respectively. The comparison between the delivered and recorded cumulative integrated luminosity in 2016 is shown in Figure 3.14. Subsequently, the recorded data is certified by the offline Data Quality Monitoring (DQM), to ensure that the data are suited for physics analysis.

3.2.6.1 Pre-amplifier saturation in the APV25 chip

During Run 2, the instantaneous luminosity delivered by the LHC increased continuously, and even exceeded the design luminosity of $10^{34} \text{ cm}^{-2}\text{s}^{-1}$ in 2016. As the luminosity increased, a dynamic inefficiency appeared in the strip tracker, which was most noticeable in the first layer of the TOB. The symptoms were a change in the signal-to-noise ratio and loss of hits. As can be seen from Figure 3.15, the most probable value (MPV) of the signal-to-noise ratio is shifted towards lower values and the low tail increased as well. The loss of hits is clearly visible in Figure 3.16, showing the change in number of hits per track for increasing instantaneous luminosities. The run periods indicated in the plot refer to a subset of the data taken over the course of the year. Run period boundaries are typically defined by changes in the LHC running conditions, changes to the detector configuration or calibration, or other parameters. The number of hits decreases for later run periods such as D and F, as the instantaneous

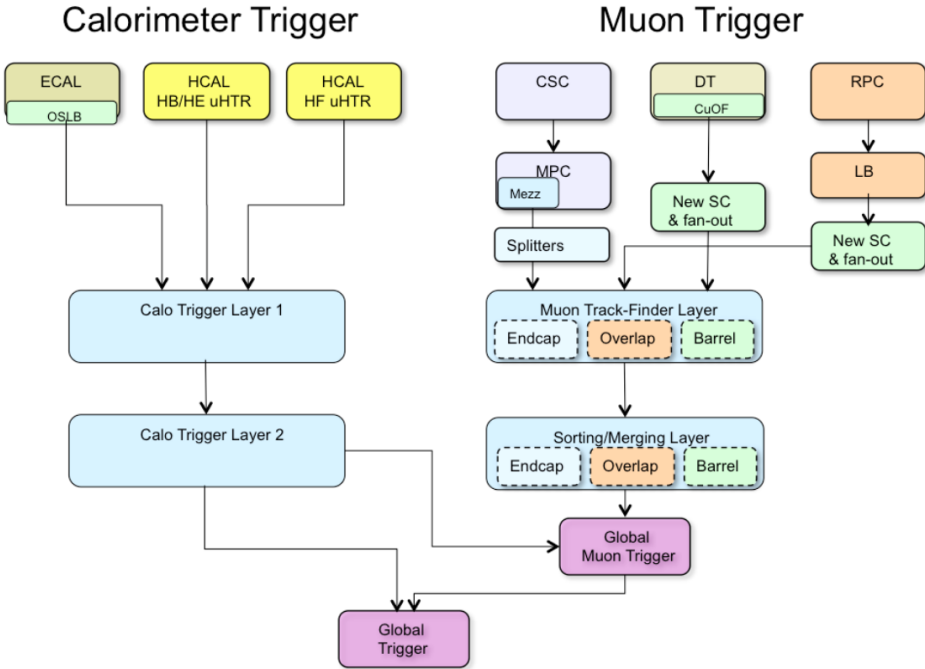


Figure 3.12: Schematic overview of the L1 Trigger. Figure taken from [108]

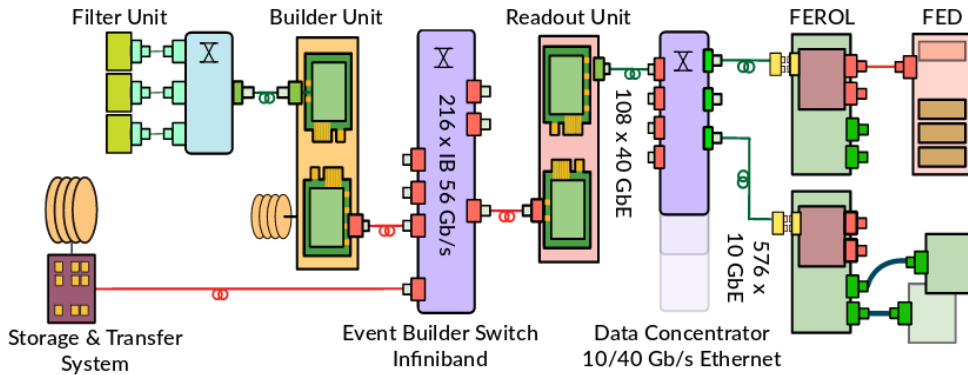


Figure 3.13: Schematic of the data acquisition (DAQ) system. Figure taken from [109]

luminosity increases. This loss of hits results in less and shorter tracks.

The origin of this inefficiency was eventually tracked down to saturation effects in the pre-amplifier of the APV25 chip. The pre-amplifier decay time changes significantly with temperature. As the operating temperature of the strip tracker was lowered from +4°C to -15°C coolant temperature during LS1, the decay time was no longer sufficient to cope with the high luminosities. The dynamic inefficiency was cured in August 2016 by changing the pre-amplifier drain speed. This lead among others to the recovery of the muon efficiency, which showed a large drop for the highest luminosities before the change and an essentially flat behaviour afterwards, as demonstrated in Figure 3.17.

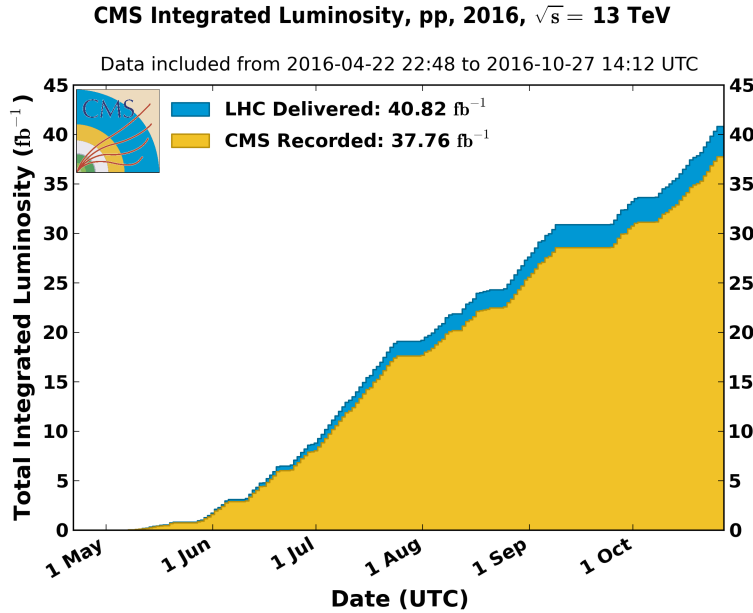


Figure 3.14: The cumulative distribution of the instantaneous luminosity delivered by the LHC (blue) and recorded by CMS (yellow) in 2016.

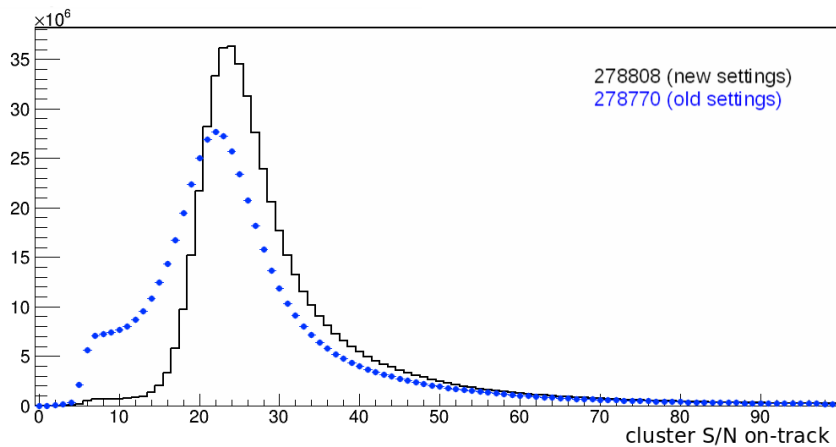


Figure 3.15: The signal-to-noise ratio for clusters on reconstructed tracks in the first layer of the TOB for a run before (blue) and after (black) the change of pre-amplifier drain speed.

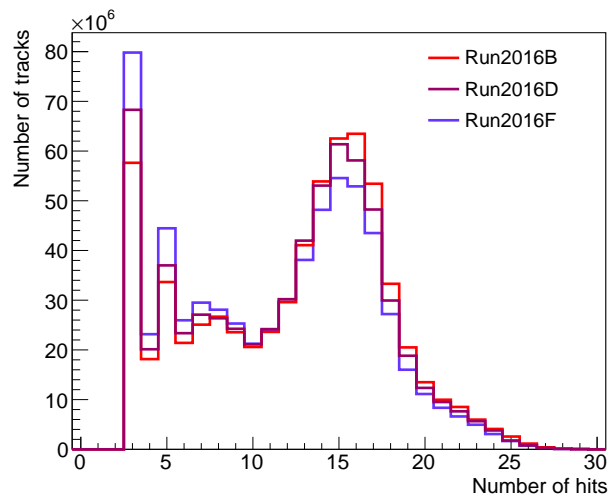


Figure 3.16: The number of hits per track for run periods B, D, and F, showing the effect of the increasing instantaneous luminosity.

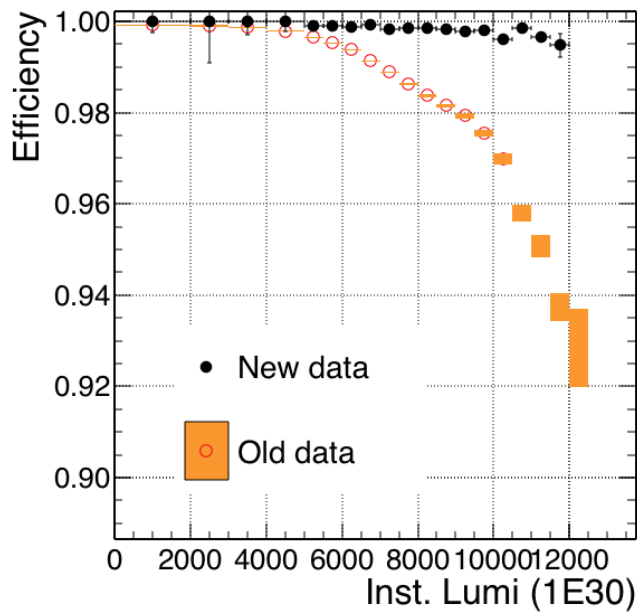


Figure 3.17: The muon efficiency as a function of the instantaneous luminosity for before (orange) and after (black) the change of pre-amplifier drain speed which cured the dynamic inefficiency.

4

1

2

Event Simulation and Reconstruction

3 In order to use the recorded data, the obtained signals coming from various parts of the detector must be
4 reconstructed to be able to identify the particles in the event. Additionally, to compare the experimental
5 results with theory, events are generated and the resulting signals in the detector are simulated, as detailed
6 in Sections 4.1 and 4.2, respectively. The event reconstruction is detailed in Section 4.3. Finally, some
7 details about the simulation of SIMPs are given in Section 4.4.

8 4.1 Event generation

9 The event structure at the LHC is complicated by the composite nature of protons, as demonstrated in
10 Figure 4.1. This sketch shows the hard interaction in red, with a tree-like structure surrounding it, repre-
11 senting the ensuing shower. In this hard scattering, the quark or gluon constituents of the protons, called
12 partons, will interact according to a so-called parton distribution function (PDF), which is determined
13 by the parton’s momentum fraction and the momentum transfer. Due to their colour charge, the partons
14 involved in the hard interaction will induce parton showers consisting of a cascade of radiation from QCD
15 processes. This is shown in blue for the incoming partons and in red for the outgoing partons. The pro-
16 duced partons will also hadronize due to colour confinement, as illustrated in green, with hadron decays
17 in dark green and radiated photons in yellow. Finally, the purple interaction represents a second interac-
18 tion between the proton remnants. Next to interactions between the proton remnants, additional activity
19 in the event can come from multiple parton interactions and pileup. All these aspects must be taken into
20 account when generating events, as detailed below.

21 Hard scattering

22 In the hard interaction, two partons of the colliding protons, will interact with a certain proba-
23 bility at a given momentum transfer. This is parametrized by the PDFs $f(x, Q^2)$, were x is the
24 proton’s momentum fraction and Q^2 is the momentum transfer scale. Experimentally determined
25 PDFs are available from various groups, including e.g. CTEQ [111], MRST/MSTW [112], and
26 NNPDF [113]. An example of such PDFs obtained by the NNPDF group is shown in Figure 4.2.
27 The PDFs are then convoluted with the matrix element of the hard scattering, which is the pro-
28 cess of interest where the two colliding partons create high-energetic final state particles. This is
29 done using an event generator, such as MADGRAPH5_aMC@NLO [114] and POWHEG [115].
30 With MADGRAPH5_aMC@NLO the matrix element can be calculated at tree-level or leading or-
31 der (LO), and since the addition of aMC@NLO at next-to-leading order (NLO) as well. This
32 generator was used to produce most of the background processes for the Monojet analysis detailed
33 in Chapter 5 and for the SIMP signal used in Chapter 6. POWHEG is able to generate events using

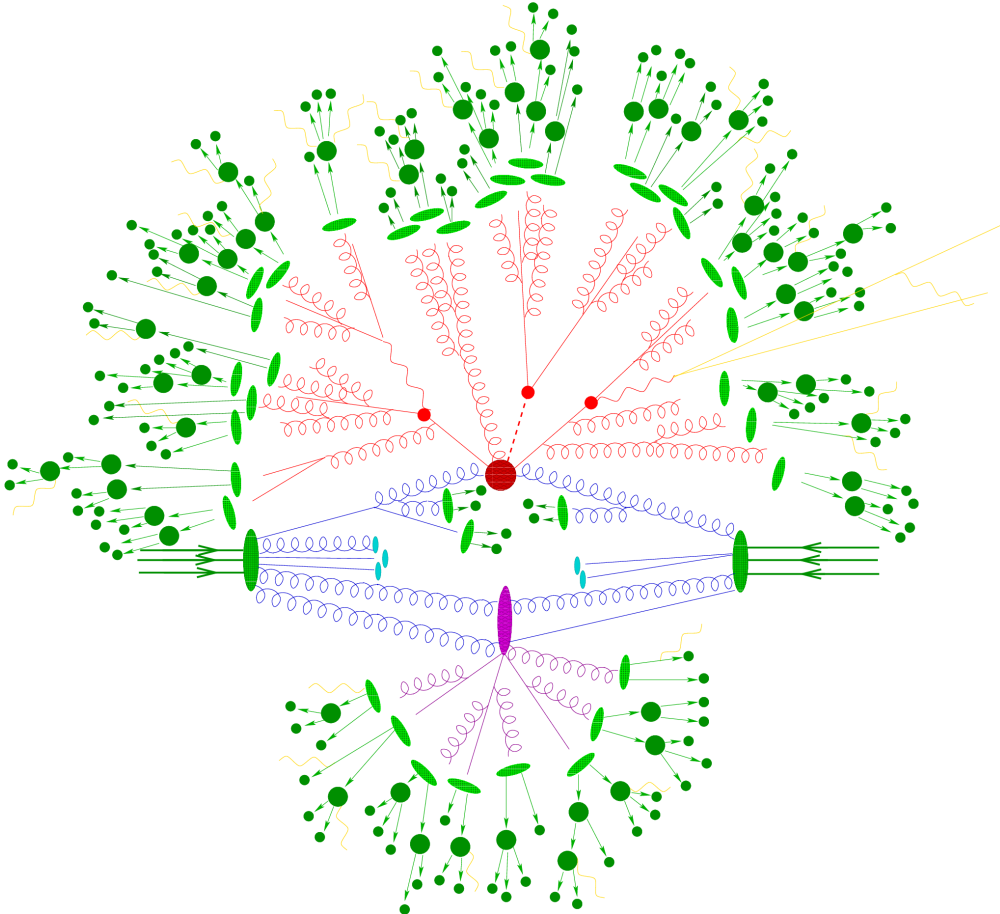


Figure 4.1: Illustration of an event showing the hard scattering, parton shower, hadronization, and underlying event. Figure taken from [110].

1 NLO computations, but only for a relatively limited number of physics processes. This generator
 2 was used to produce the monojet signal samples and the background processes from single-top
 3 production. Since NLO calculations are more time-consuming, one can instead use the less precise
 4 method of scaling a LO cross section to the NLO level by using a so-called k-factor, defined as the
 5 ratio of the NLO and LO cross sections. However, these k-factors often need to be determined as
 6 a function of the relevant kinematic variables as they depend on the kinematic phase space and the
 7 probed energy scale.

8 **Parton showering**

9 Since the colliding partons have a colour charge, the hard scattering will be accompanied by a
 10 cascade of radiation from QCD processes. The partons will for example radiate soft gluons or
 11 split into two collinear partons. This radiation can originate from the incoming partons, which is
 12 referred to as initial state radiation (ISR), or the outgoing partons in the final state, the so-called final
 13 state radiation (FSR). The perturbative evolution of the cascade can be modelled using the DGLAP
 14 (Dokshitzer-Gribov-Lipatov-Altarelli-Parisi) equations [116–118]. These equations describe the
 15 time evolution of the probability of a ‘mother’ parton to split into ‘daughter’ partons at an energy
 16 scale Q^2 . The momentum of the mother is then divided among the daughter partons, which can in
 17 turn split into other partons at a lower Q^2 scale. The cascade continues down to an energy scale
 18 Λ_{QCD} where the strong coupling constant becomes unity. The resulting number of jets can vary
 19 depending on the modelled process, as shown in Figure 4.3. Still need to describe figure, but it
 20 shows the opposite as expected for vector and scalar

21 **Hadronization**

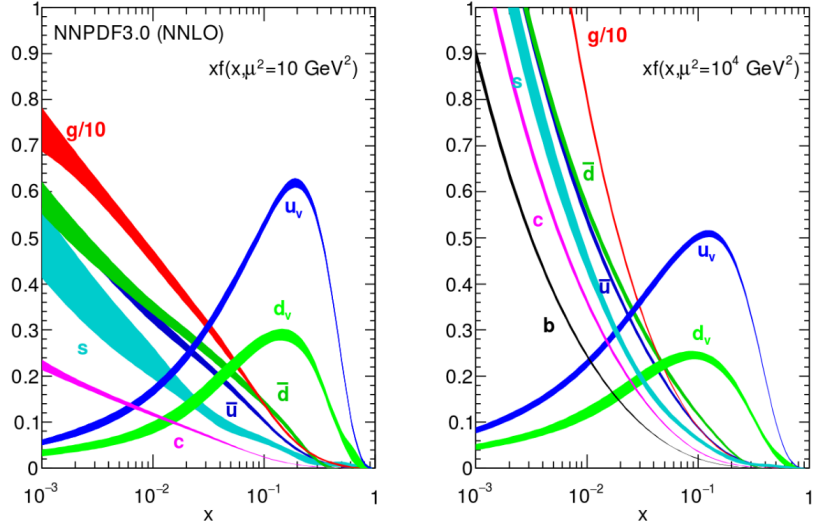


Figure 4.2: The parton distribution functions times the momentum fraction x at energy scales 10 GeV^2 (left) and $10\,000 \text{ GeV}^2$ (right), obtained in NNLO NNPDF3.0 global analysis. Figures taken from [113].

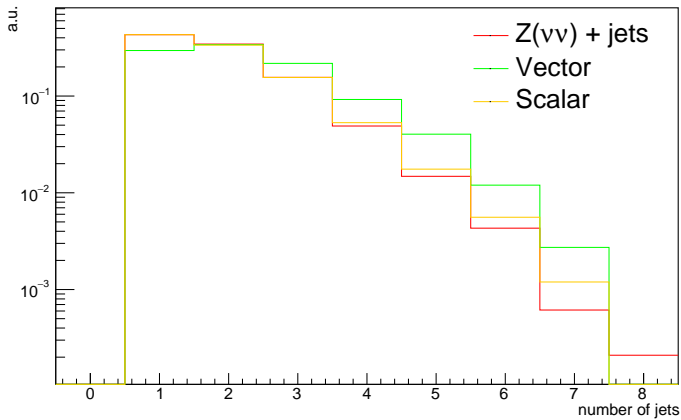


Figure 4.3: .

1 The next step after the showering is the hadronization of the coloured particles produced in the
 2 parton shower, transforming them into colour-neutral hadrons. Since this happens at low energy
 3 scales where the perturbative approach of QCD is not valid, phenomenological models have to
 4 be used. For most of the processes considered in this thesis, the showering and hadronization is
 5 done with PYTHIA 8 [119], using a standard set of parameters which were tuned to reproduce the
 6 experimental data. In PYTHIA, the string Lund model [120] is used, based on string fragmentation.
 7 This model starts from the idea of a string connecting a quark q and an antiquark \bar{q} , following
 8 the assumption of linear confinement. As the two quarks move away from each other, the string
 9 stretches and the potential energy stored in the string increases. The increase in potential energy is
 10 assumed to be proportional to the distance between the quarks. When the energy becomes sufficient
 11 to produce a new pair of quarks $q'\bar{q}'$ with mass m , the string breaks and the original quark pair is
 12 split into two new pairs, $q\bar{q}'$ and $q'\bar{q}$. If the invariant mass of the new strings is large enough, the
 13 same process is repeated, leading to a new break-up. This procedure continues until only colour-
 14 neutral hadrons with an on-shell mass remain.

15 Additional activity in the event

16 In addition to ISR and FSR, also beam remnants and multiple parton interactions give rise to ad-

ditional activity in the event, referred to as the underlying event. After the partons participating in the hard scattering are extracted, the remainder of the protons have a non-zero colour charge. The creation of additional hadrons during the hadronization is therefore possible. Multiple parton interactions represent additional interactions which can take place between other incoming partons. As the probability for an additional hard interaction to occur is rather small, the activity from multiple parton interaction is typically much less energetic than the hard interaction, producing mostly low energetic hadrons. Finally, additional collisions between other protons in the same bunch crossing or from a previous bunch crossing, respectively referred to as in-time and out-of-time pileup, add extra activity in the event. The pileup distribution is for example shown in Figure 4.4 for QCD dijet events recorded in 2016, and is compared to simulated QCD events. This shows that there were about 20 collisions per bunch crossing on average. Typically, the simulation does not completely agree with the data and needs to be reweighted in order to match the data.

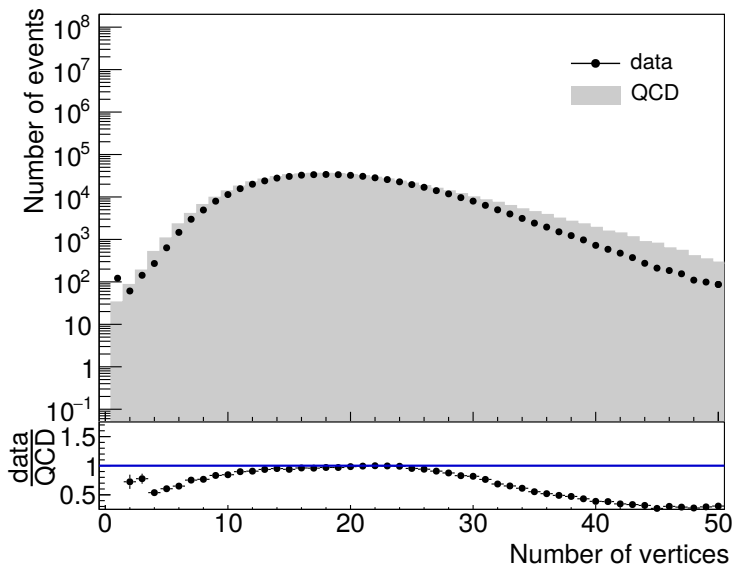


Figure 4.4: The pileup distribution of QCD dijet events recorded in 2016 compared to simulated QCD events.

4.1.1 Simulation of the monojet signals

In the monojet analysis, the simplified models described in Section 2.2.4 are considered. The used signal samples were generated with POWHEG, which can generate NLO vector and axial mediator production and LO scalar and pseudoscalar production. The samples were also produced at LO with MCFM [121] as a cross check. The scanned mediator masses are $m_\phi = 10, 20, 50, 100, 200, 300, 500, 1000, 2000, 10\,000 \text{ GeV}$, for dark matter masses of $m_\chi = 1, 10, 50, 100, 150, 500, 1000 \text{ GeV}$, with $m_\chi \leq m_\phi$.

4.2 Detector simulation

After being generated, the collision events are passed on to the CMS detector simulation, which is based on the GEANT 4 [122] simulation toolkit. This toolkit provides a description of the interaction between particles and the detector material, including effects such as bremsstrahlung of charged particles, photon conversions, energy loss of charged particles by ionization, and the showering of electrons, photons and hadrons in the calorimeters due to interaction with the material. The CMS simulation package contains the geometry of the detector with all the sensitive layers designed to detect the traversing particles, as well

as the dead material regions consisting of e.g. support structures, cables and cooling pipes. A precise map of the magnetic field is also included in order to simulate the curvature of the charged particles correctly.

Next, the impact of the detector, coming from the electronic response produced by the hits in the active detector material, the digitization, the data transmission, and any reconstruction performed in the electronics such as zero-suppression or cluster reconstruction, is simulated. In this way, an event content similar to the output of the real detector is obtained. At this point the effect of pileup is also included by adding detector hits of generated proton-proton interactions on top of the hits resulting from the main interaction. Most of the simulated event samples used in this thesis are processed using this detector simulation. However, the interaction of new particles that can arise from specific theory models is not always readily described in GEANT. This is the case for the signal samples used in the analysis described in Chapter 6, so an additional step was needed in order to simulate strongly interacting massive particles (SIMPs) in the CMS detector, described in Section 4.4.

4.3 Event reconstruction

Once the detector response has been simulated, the obtained events can be reconstructed. The same method is applied for these simulated events and for data coming from the detector. First, the reconstruction of tracks is performed, with a specific track reconstruction for electrons and muons. Furthermore, the calorimeter deposits, generated by electrons, photons, and hadrons, are grouped into clusters. Additionally, the reconstruction is further improved by using the so-called particle flow (PF) algorithm. This algorithm greatly improves the performance for jet and hadronic τ decay reconstruction, missing transverse energy momentum determination, as well as electron and muon identification. Finally, the obtained particle flow (PF) candidates are clustered into jets, and the missing transverse energy can be derived.

4.3.1 Track and vertex reconstruction

The tracks of charged particles going through the CMS tracker are reconstructed with an iterative tracking approach. This is used to cope with the high occupancy and consequently high combinatorics. Additionally, the first iterations search for tracks with less possible combinations, such as tracks with many pixel hits or a high momentum. After every iteration, the hits associated with the found track are removed to reduce the combinatorics. Each iteration consists of four steps:

1. **Seed generation.** In this first step hits are combined into seeds for the subsequent track finding. In the initial iterations pixel triplets are used, then pixel pairs, in order to take gaps or non-working modules into account. Next, mixed pixel/strip triplets are taken, and finally strip-only seeds are used. These additional iterations improve the acceptance in p_T and in displacement with respect to the primary vertex.
2. **Track finding.** The seeds are used as starting point for a Kalman filter algorithm. This method extrapolates the seed trajectory outward to the next layer, taking into account potential energy loss and multiple scattering. If compatible hits are found in the next layer, the parameters of the trajectory are updated. This process continues until the outermost layer of the tracking system. Using this method, a given seed can generate multiple tracks, or different tracks can share hits. A trajectory cleaner therefore determines the fraction of hits the tracks have in common and discards the track with the lowest number of hits when there are too many shared hits. If both tracks have the same number of hits, the track with the largest χ^2 value is removed.
3. **Track fitting.** The track parameters are then refitted using a Kalman filter and smoother, taking all hits determined in the track finding step into account.
4. **Track selection.** Finally, the tracks are selected based on quality requirements, such as the number of layers that have hits, the χ^2/dof , and the distance to a primary vertex. This greatly reduces the fraction of reconstructed tracks that are fake.

The performance of the track reconstruction is excellent, and a high track-finding efficiency is obtained [123] while keeping the rate of fake tracks negligible. The highest tracking efficiency is obtained for muons, which traverse the full detector volume and have an improved momentum resolution due to tracking information from the muon detectors giving a long lever arm. For isolated muons with p_T between 1 and 100 GeV the tracking efficiency is higher than 99% for the entire η coverage of the tracker, as can be seen from the left plot in Figure 4.5. The p_T resolution is about 2-3% for a muon with $p_T = 100$ GeV up to $|\eta| < 1.6$, but worsens for higher pseudorapidities. Different types of particles interact differently with the detector material. Charged hadrons, for example, are also subject to elastic and inelastic nuclear interactions and have a tracking efficiency of 80-95% depending on pseudorapidity and transverse momentum, as shown in the right plot of Figure 4.5.

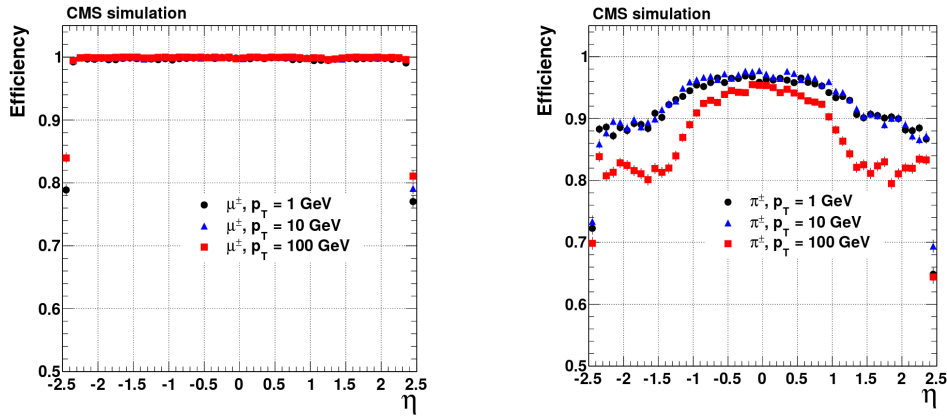


Figure 4.5: The muon efficiency (left) and pion efficiency (right) as a function of pseudorapidity, for multiple transverse momenta. Figures taken from [123]

Finally, the primary vertex is reconstructed from the tracks. Since the collisions happen between bunches of protons, multiple protons will be colliding at the same time. The extra collisions, next to the potentially interesting collision, are referred to as pile-up interactions. The particles generated in these collisions are all detected simultaneously and form a challenge to disentangle them from the particles coming from the to be studied interaction.

The reconstruction is done in 2 steps: first the tracks that appear to originate from the same interaction vertex are clustered, then a fitting procedure computes the vertex parameters and assigns a weight to each associated track, reflecting the probability that it corresponds to the considered vertex. Figure 4.6 shows the reconstruction efficiency and the resolution of the primary vertex. The more tracks, the better the vertex is constrained and thus the better the resolution.

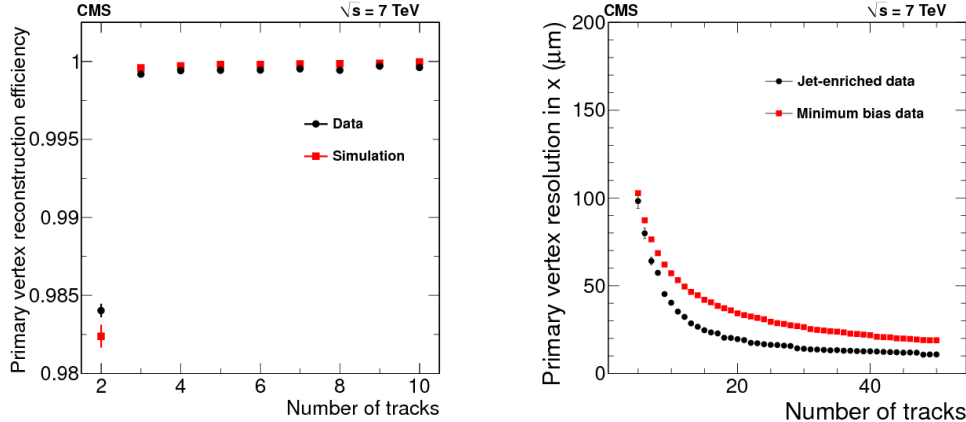


Figure 4.6: The primary vertex reconstruction efficiency (left) and resolution (right) as a function of the number of tracks associated to it. Figures taken from [123]

1 The vertex with the highest $\sum p_T^2$ is chosen as primary vertex, where the sum runs over the tracks
 2 associated to the vertex following the application of a deterministic annealing filter which assigns weights
 3 to sufficiently high-quality tracks that enter the vertex fit [123]. While in events with jets many tens of
 4 high-momentum tracks can usually be associated to a primary vertex, thus making primary vertex finding
 5 almost fully efficient and pure, in the case of a pair of neutral jets, produced for example by SIMPs, this is
 6 not the case any more. The underlying event and potentially initial state QCD radiation can still provide
 7 some tracks, but in extreme cases a wrong vertex is chosen, arising from a hard pileup collision.

8 **4.3.2 Electron and isolated photon reconstruction**

9 Electrons are reconstructed using information from both the tracker and the calorimeters. Due to the large
 10 amount of material present in the tracker, electrons will emit bremsstrahlung photons, and photons will
 11 often convert into e^+e^- pairs, which can again radiate bremsstrahlung photons.

12 For electrons, a Gaussian-sum filter (GSF) [124] candidate is taken as starting point. This GSF can-
 13 didate is obtained using 2 different methods to reconstruct the electron track from the hits in the tracker,
 14 which should gather all radiated energy from the electron. First, the ECAL-based approach is used,
 15 grouping ECAL clusters into superclusters. These superclusters collect the energy of the electron and the
 16 bremsstrahlung photons in a small η window and a large ϕ window, taking the bending of the electron
 17 track in the magnetic field into account. The supercluster energy and position is then used to estimate
 18 the position of the corresponding hits in the tracker layers. Subsequently, the tracker-based approach
 19 is used to find electrons missed by the ECAL-based method. In this case, the tracks from the iterative
 20 tracking with transverse momentum larger than 2 GeV are used. Additional requirements are placed on
 21 the number of hits and the χ^2 of the fit, and the specific electron tracking is performed, using a GSF fit,
 22 which is more adapted to electrons than the Kalman filter used in the iterative tracking, as it describes the
 23 energy loss in each tracker layer. The electron seeds obtained with both methods are merged and used as
 24 input for the full electron tracking. The obtained electron tracks are then linked to ECAL clusters by the
 25 PF algorithm, as described in Section 4.3.6. In the case of isolated photons, a candidate is seeded from
 26 an ECAL supercluster with transverse energy larger than 10 GeV which is not linked to a GSF track.

27 The total energy of the accumulated ECAL clusters is corrected for the energy that was lost in the
 28 process of reconstruction, using analytical functions of the energy and pseudorapidity. The applied cor-
 29 rections can be as large as 25%, at low transverse momentum and at $|\eta| = 1.5$, where the material density
 30 in the tracker is largest. The energy of the electron is then obtained from a combination of the corrected
 31 energy and the momentum of the GSF track, while the direction of the electron is taken from the GSF
 32 track. For photons, the corrected energy and the direction of the supercluster are used.

33 **4.3.3 Electron and photon identification**

34 In general, the electron and photon candidates must satisfy identification criteria to be retained. In the case
 35 of electrons two methods for identification are available: a cut-based identification or a boosted decision
 36 tree (BDT) combining fourteen variables including the amount of energy radiated and the ratio between
 37 the energies gathered in HCAL and ECAL. In the monojet analysis described in Chapter 5, the former is
 38 used. In method, four different working points are defined, denoted as “tight”, “medium”, “loose”, and
 39 “veto”, with varying signal efficiency and background rejection. For the electron veto the loose selection
 40 is used, while a tight identification is required on one electron to select the events in the dielectron and
 41 single electron control regions.

42 Similarly, for the photons, both a cut-based identification and a multivariate analysis can be used.
 43 Both for the monojet and the SIMP analysis, described in Chapters 5 and 6, the cut-based identification
 44 is used. Three standard working points are provided, denoted as “loose”, “medium”, and “tight”, with
 45 an average efficiency of 70%, 80%, and 90%, respectively. In both analyses, the loose identification is
 46 used for the photon veto. In the SIMP analysis, the event is only rejected when the identified photon is
 47 within a cone of $\Delta R < 0.1$ of one of the two leading jets. Additionally, the photon veto is extended to
 48 reject events containing jets with a large photon energy fraction and unidentified photons. This happens
 49 for instance when there is a photon conversion in the tracker. The event is therefore rejected when the

variable	loose		tight	
	barrel	endcaps	barrel	endcaps
full 5x5 $\sigma_{in\eta in\eta}$	< 0.0114	< 0.0352	< 0.0101	< 0.0279
$ \Delta\eta_{in} $	< 0.0152	< 0.0113	< 0.00926	< 0.00724
$ \Delta\phi_{in} $	< 0.216	< 0.237	< 0.0336	< 0.0918
H/E	< 0.181	< 0.116	< 0.0597	< 0.0615
relative isolation	< 0.126	< 0.144	< 0.0354	< 0.0646
1/E - 1/p	< 0.207	< 0.174	< 0.012	< 0.00999
$ d_{xy}(\text{vtx}) $	< 0.0564	< 0.222	< 0.0111	< 0.0351
$ d_z(\text{vtx}) $	< 0.472	< 0.921	< 0.0466	< 0.417
expected inner missing hits	≤ 2	≤ 3	≤ 2	≤ 1
pass conversion veto	yes	yes	yes	yes

Table 4.1: Loose and tight electron identification criteria. The isolation is computed in a cone of $\Delta R < 0.3$ around the electron.

jet photon energy fraction is larger than 0.8, the photon is not identified by the loose criteria, and the conversion is matched to the photon within $\Delta R < 0.2$ and has $p_{T,\text{conv}}/p_{T,\gamma} > 0.3$. Lastly, the two jets are also required to have a neutral electromagnetic energy fraction lower than 0.9, corresponding to one of the standard tight jet identification requirements mentioned in Section 4.3.7. The full jet ID is not applied, since the requirements on e.g. the neutral hadronic energy fraction and the charged multiplicity would reject the signal events. Finally, the monojet analysis uses a photon + jets control region as well. These events are selected by applying the tight photon identification.

variable	loose		tight
	barrel	endcaps	barrel
full 5x5 $\sigma_{in\eta in\eta}$	< 0.0102	< 0.0274	< 0.0102
H/E	< 0.05	< 0.05	< 0.05
charged hadron isolation	< 3.32	< 1.97	< 1.37
neutral hadron isolation	$< 1.92 + 0.014 \times p_T$ $+ 1.9 \times 10^{-5} \times p_T^2$	$< 11.86 + 0.0139 \times p_T$ $+ 2.5 \times 10^{-5} \times p_T^2$	$< 1.06 + 0.014 \times p_T$ $+ 1.9 \times 10^{-5} \times p_T^2$
photon isolation	$< 0.81 + 0.0053 \times p_T$	$< 0.83 + 0.0034 \times p_T$	$< 0.28 + 0.0053 \times p_T$
conversion safe electron veto	yes	yes	yes

Table 4.2: Loose and tight photon identification criteria. The isolation is computed in a cone of $\Delta R < 0.3$ around the photon.

4.3.4 Muon reconstruction

Muon tracking is performed using 2 complementary approaches. The first method starts from standalone muons, which are reconstructed from hits in the muon detectors only using pattern recognition. The standalone muons are then matched to tracks in the tracker, and the hits are combined to form a global muon track. This global muon fit improves the momentum resolution compared to the tracker-only fit at muon momenta larger than 200 GeV.

For momenta below 10 GeV, muons often fail the global muon conditions which require the muon to penetrate through more than one muon detector plane, due to the large multiple scattering in the return yoke. In this case, tracker-only muon reconstruction is more efficient since it only requires one muon segment. Each track in the tracker with a transverse momentum larger than 0.5 GeV and a total momentum larger than 2.5 GeV is therefore extrapolated to the muon system and if at least one matching track segment is found, it is retained as muon candidate.

Within the geometrical acceptance of the muon system about 99% of the muons are reconstructed, either as global muon or as tracker muon and frequently as both. Global and tracker muons that share the same track inside the tracker are merged into a single candidate. Muons that are only reconstructed as standalone muons have a worse momentum resolution compared to the global and tracker muons. These standalone muons are however only considered in the further reconstruction when the fit is of high quality

and is associated with a large number of hits in the muon system.

Charged hadrons can be misreconstructed as muons if e.g. a part of the hadron shower reaches the muon system. In order to improve the muon identification, the PF muon identification algorithm described in Section 4.3.6 also matches energy deposits in the ECAL and HCAL with the muon track.

4.3.5 Muon identification

When using muons for physics analysis, some identification criteria are generally applied in order to ensure the quality of the muons. There are several levels of identification, denoted as “tight”, “medium”, and “loose”, which provide a trade-off between muon identification efficiency and misidentification. In general, the tight and loose identification are the most widely used identification criteria.

The loose identification only requires the muons to be either global or tracker-only muons, and to be identified as a PF muon. As a result, it is highly efficient for both prompt muons and muons from quark decays. In analyses with prompt muons, this identification is therefore often complemented by an impact parameter cut.

For the tight identification, the muon is required to be a global muon and to pass the PF muon identification. The normalized χ^2 of the global muon track fit should be smaller than 10 to suppress hadronic punch through and muons from decays in flight. To further suppress these contributions at least one muon chamber hit should be included in the global muon track fit and muon segments should be found in at least two muon stations. Cosmic muons and tracks from pileup are suppressed by requiring the tracker track to have $d_{xy} < 2$ mm and $d_z < 5$ mm, with d_{xy} the traverse impact parameter and d_z the longitudinal distance with respect to the primary vertex. Finally, at least one pixel hit is required, as well as hits in at least 5 tracker layers, in order to guarantee a good p_T measurement.

In the case of the monojet analysis described in Chapter 5, the loose muon identification is used to select muons for the muon veto. An additional isolation cut is of 0.2 applied in order to select only prompt muons. The isolation value is computed as the sum of the transverse momenta of all charged hadrons associated to the primary vertex, neutral hadrons, and photons in a cone of $\Delta R < 0.4$ around the muon, relative to the p_T of the muon. The tight muon identification is used as well, to select events in the dimuon and single muon control regions.

4.3.6 Particle flow

The particle flow (PF) algorithm [125] reconstructs so-called particle flow candidates by combining information from all different CMS subdetectors, linking different elements, such as tracks in the tracker, calorimeter clusters, and muon tracks. A global picture of the event is thus formed, where each particle is uniquely identified. The obtained collection of particle candidates is subsequently used to reconstruct jets and tau leptons, and to determine the missing transverse energy.

In a first step, the PF algorithm identifies charged particle tracks, as defined in Section 4.3.1 for all tracks, and in Sections 4.3.2 and 4.3.4 for electron and muon tracks in particular. At the same time, the calorimeter clusters are reconstructed with a clustering algorithm designed specifically for the PF event reconstruction. In this algorithm, cluster seeds are first identified as local energy maxima with respect to the four or eight closest cells, if the energy deposited in the cell is above a given seed threshold. The clusters are then formed by accumulating neighbouring cells with an energy above a given cell threshold, suppressing noise.

The PF elements in the different subdetectors are then connected by a link algorithm which avoids any double counting. The link algorithm produces blocks of associated elements, quantifying the quality of the link by defining a geometrical distance between the elements. When an element is linked to multiple other elements, only the link with the shortest distance is kept. More precisely, a link between a track in the tracker and a calorimeter cluster is made by extrapolating it from the last hit in the tracker to the calorimeters. The distance between the position of the extrapolated track and the cluster in the (η, ϕ) plane is then used to define the link distance. At the interaction points between the track and the tracker layers, tangents to the GSF tracks are extrapolated to the ECAL in order to collect the energy of photons radiated by electron bremsstrahlung. A dedicated conversion finder was also developed to

1 identify bremsstrahlung and prompt photon conversions into e^+e^- pairs. Links between calorimeter
 2 clusters are established outside of the tracker acceptance, or between the preshower and ECAL clusters in
 3 the preshower acceptance. In this case the link distance is also defined as the distance between the position
 4 of the clusters. Charged particle tracks can also be linked by a common secondary vertex. Finally, the PF
 5 muon identification algorithm associates the muon tracks to the muon energy deposits in the ECAL and
 6 HCAL, to improve the muon identification performance.

7 In a next step, the PF blocks obtained by linking the multiple PF elements, are classified as muons,
 8 electrons, or isolated photons. The corresponding elements are then excluded from further consideration.
 9 Once electrons, muons, and isolated photons have been identified, the remaining elements are identified
 10 as charged hadrons, neutral hadrons, or photons produced in jets. Within the tracker acceptance, the
 11 ECAL clusters not linked to any track are classified as photons, while the clusters in the HCAL without
 12 a matched track are labelled as neutral hadrons. Outside of the tracker acceptance, charged and neutral
 13 hadrons can not be distinguished. ECAL clusters linked to an HCAL cluster are then assumed to arise
 14 from the same hadron shower, and the estimated energy for these particles is the sum of the energy
 15 deposited in the ECAL and the HCAL. The ECAL clusters that are not linked to an HCAL cluster are
 16 classified as photons.

17 4.3.7 Jet reconstruction

18 Jets are reconstructed with the anti- k_T algorithm [126], which clusters either the generated particles from
 19 event simulation, or the particles reconstructed by the PF algorithm (PF jets), or the energy deposits in
 20 the calorimeters (Calo jets). This procedure takes into account the transverse momentum p_T , also called
 21 k_T , of the particles and the distance between particles, defined as

$$\Delta R_{ij} = \sqrt{(\eta_i - \eta_j)^2 + (\phi_i - \phi_j)^2}. \quad (4.1)$$

22 The strategy consists of the following steps:

23 1. For every pair of particles i and j , a distance d_{ij} defined as

$$d_{ij} = \min \left(\frac{1}{p_{Ti}^2}, \frac{1}{p_{Tj}^2} \right) \frac{\Delta R_{ij}^2}{R^2} \quad (4.2)$$

24 is calculated.

25 2. For every particle i , a distance d_{iB} to the beam pipe is calculated with

$$d_{iB} = 1/p_{Ti}^2. \quad (4.3)$$

26 3. The minimum of d_{ij} and d_{iB} is then determined.

27 4. If it is d_{ij} , particles i and j are recombined into a new particle by adding the four-momenta of the
 28 particles. If it is d_{iB} , particle i is declared to be a jet and it is removed from the list of particles.

29 5. This is repeated until no particles remain.

30 In this clustering algorithm, the parameter R determines what is called a jet. If a particle i has
 31 no other particles within a distance R , d_{iB} will be smaller than d_{ij} and the particle will become a jet.
 32 A consequence of this is that an arbitrarily soft particle can become a jet, and therefore a minimum
 33 transverse momentum for a jet to be of interest is defined.

34 The anti- k_T algorithm favours clustering around hard particles, and the jets then grow outward from
 35 this seed. This gives rise to circular jets, with a cone size that is proportional to R . Since it still involves
 36 a combination of energy and angle in the distance measure, this is a collinear-safe growth, meaning that
 37 the jet will not change when one of the particles of the jet is split collinearly. This algorithm is also
 38 infrared-safe, i.e. the same set of jets is obtained when soft particles are emitted.

A reliable determination of the jet energy is not straightforward, since many effects can distort the energy estimation, such as the calorimeter response, the limited particle reconstruction efficiency, the underlying event, the pileup, and the charged particles bending out of the jet cone due to the strong magnetic field. The pileup is mitigated by applying charged hadron subtraction (CHS), which consists of removing charged hadrons associated with vertices other than the primary vertex from the list of PF candidates. Additionally, the jet energy is corrected using a factorized approach, as illustrated in Figure 4.7, with the following steps:

- **Pileup correction (L1).** The first level of jet energy corrections is applied event-by-event and jet-by-jet, and is determined from simulation. It is dependent on the pseudorapidity and transverse momentum of the jet, the average p_T density in the event, and the effective jet area. This effective area is determined by injecting a large number of very soft particles in the event before the jet clustering. The spread of the soft particles in each jet then defines the jet area. When these corrections are applied on data, residual corrections are also applied to take into account the difference between the simulated events and the data.
 - **Relative η and absolute p_T corrections (L2L3).** These corrections are also obtained from simulations and correct for the non-uniform response of the calorimeters in η and p_T . They are determined by comparing the reconstructed p_T to the one obtained from the jets built from the generated particles. These corrections have the largest impact on the jet energy.
 - **Residual η and p_T corrections (L2L3Residual).** Since the L2L3 correction is derived from simulation, additional residual corrections are needed in order to correct for the remaining small differences between the jet response in data and simulation. These corrections are typically of the order of a few percent.

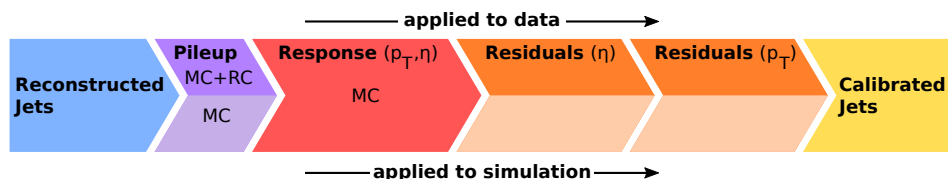


Figure 4.7: Graphical overview of the factorized approach used at CMS to apply jet energy corrections.

23 Optionally, a set of identification criteria are applied on the PF jets. A jet is required to consist of
 24 at least two particles. For jets in the region $|\eta| < 2.7$, the fraction of energy coming from either neutral
 25 hadrons or photons should not exceed 99%. Additionally, for jets restricted to the tracker acceptance
 26 ($|\eta| < 2.4$), there should at least be some energy deposited in the HCAL, the jet should contain 1 or more
 27 charged constituent, and the fraction of energy corresponding to electrons or photons should not exceed
 28 99%.

Moreover, jets from pileup can be identified as well. This pileup jet identification relies on the topology of the jet shape which is used to disentangle jets coming from the overlap of multiple interaction and real hard jets, the object multiplicity, and the compatibility of the tracks in the jets with the primary vertex. This last property of pileup jets can evidently only be exploited for jets within the tracker acceptance.

4.3.8 Identification of b-jets

For the identification of jets originating from b quarks, the long lifetime of the b hadrons arising from the hadronization of b quarks is exploited. The b hadrons will therefore decay at a position that is displaced with respect to the primary interaction vertex. The b -jets can then be identified by looking for the presence of displaced tracks from which a secondary vertex may be reconstructed. Additionally, the b hadrons have a probability of 20% to decay into muons or electrons. Consequently, the presence of these charged leptons can be used as well for b -jet identification techniques.

Within the CMS collaboration, two different algorithms are being used during Run 2, namely the Jet Probability and the Combined Secondary Vertex taggers [127]. In this thesis, the latter is used to

1 identify b-jets, combining the information from displaced tracks and secondary vertices in a multivariate
 2 technique. Jets are then identified or “tagged” as b-jets by applying a cut on the discriminator output.
 3 Three standard operating points are defined, denoted as “loose”, “medium”, and “tight”, corresponding
 4 to a misidentification probability of 10%, 1%, and 0.1% for light jets with $p_T > 30$ GeV, respectively.

5 **4.3.9 Reconstruction of tau leptons**

6 Tau leptons can decay into either a charged lepton and two neutrinos, or a few hadrons and one neutrino.
 7 The hadronic decays of the tau lepton can be separated from quark or gluon jets by analysing the
 8 decay products. With the PF algorithm, it is possible to resolve the particles originating from the tau
 9 decay and to determine its isolation. Hadronic tau decays are reconstructed using the hadrons-plus-strips
 10 (HPS) algorithm [128] by using those particles as input. The jet constituent particles are combined into
 11 candidates compatible with one of the main hadronic tau decay modes, $\tau^- \rightarrow h^-\nu_\tau$, $\tau^- \rightarrow h^-\pi^0\nu_\tau$,
 12 $\tau^- \rightarrow h^-\pi^0\pi^0\nu_\tau$, and $\tau^- \rightarrow h^-h^+h^-\nu_\tau$. This PF reconstruction of the tau decay products has signifi-
 13 cantly improved the reconstruction and identification of the tau leptons compared to the previous method
 14 which only took the energy deposits in the calorimeters into account.

15 **4.3.10 Missing transverse momentum reconstruction**

16 While most particles produced in the collisions can be reconstructed from the hits and energy deposits
 17 in the detector, some collision products might not leave energy deposits in tracker, calorimeters or muon
 18 system. This makes an accurate reconstruction of this type of particles impossible, and an alternative
 19 method is used, based on indirect observations. As the detector is hermetically closed such that all
 20 other particles in the event can be detected, the missing transverse momentum can be determined. This
 21 momentum then corresponds to all undetected particles in the event, and can be calculated from the
 22 vectorial sum of the transverse momenta of all the observed final state particles:

$$\vec{E}_T^{miss} = - \sum \vec{p}_T, \quad (4.4)$$

23 where the sum runs over all reconstructed PF particles. The variable that is generally used in particle
 24 physics analyses is the norm of the missing transverse momentum:

$$E_T^{miss} = |\vec{E}_T^{miss}|. \quad (4.5)$$

25 A notable example of particles leaving no hits or energy deposits behind are neutrinos, as they are
 26 neutral and weakly interacting and will therefore traverse the entire detector unhindered. Other hypothet-
 27 ical neutral weakly interacting particles, which are being searched for in many physics analyses, would
 28 escape the detector without producing hits as well.

29 **4.4 Simulation and reconstruction of the SIMP signal**

30 For the generation of the SIMP signal, the model Lagrangian given in equation 2.17 is implemented
 31 in FEYNRULES 2.0 [129]. The matrix element is then calculated at LO and events are generated us-
 32 ing MADGRAPH 5. The subsequent parton shower and hadronization is done with PYTHIA 8, using tune
 33 CUEP8M1. Several samples were produced, with SIMP mass $m_\chi = 1, 10, 100, 200, 400, 700, 1000$ GeV.
 34 The corresponding production cross sections are given in Table 4.3. Next, the events are then simulated
 35 in the CMS detector using GEANT. However, the SIMPs are not included in the simulation, as these new
 36 particles are unknown in GEANT and their interaction with matter has not been implemented yet. In order
 37 to simulate the new dark matter candidates in the CMS detector two new approaches were implemented.

38 In the first approach, the SIMPs were incorporated by adding an additional step to the standard re-
 39 construction described in Section 4.3. In this additional step the SIMPs are directly converted to neutral
 40 PF candidates and merged with the rest of the PF candidates. Additionally, the new PF candidates are
 41 smeared with jet energy resolution (JER) distributions obtained from a sample produced using neutrons
 42 instead of SIMPs. Neutrons were chosen because of their resemblance to the SIMPs as single neutral
 43 particles generating a hadronic shower.

m_χ [GeV]	$\sigma_{\bar{\chi}\chi}$ [pb]
1	4.46
10	4.40
100	2.55
200	0.790
400	0.0743
700	0.00485
1000	0.000571

Table 4.3: Production cross section for each SIMP mass, after $|\eta_\chi| < 2.5$ and $p_T^\chi > 200$ GeV generator level cuts.

1 Order to produce this sample, the same additional custom step is applied, but in this case the neutrons
2 will also be correctly reconstructed by the standard reconstruction. The reconstructed PF candidates that
3 are matched to the generated neutrons are therefore removed before injecting the converted generated
4 neutrons to the collection of PF candidates. The applied JER distributions are derived by comparing
5 the resulting uncorrected PF jets with the corresponding neutrons in sample produced with the standard
6 reconstruction using the full GEANT simulation. The resolution is computed in bins of η and p_T , and
7 an example is shown in Figure 4.8 for central neutrons with low and high transverse momentum.
8 After applying this smearing, the P2PF jets are processed with the standard sequence of CHS, jet
9 clustering, L1FastJet, and L2/L3 corrections described in Section 4.3.7.

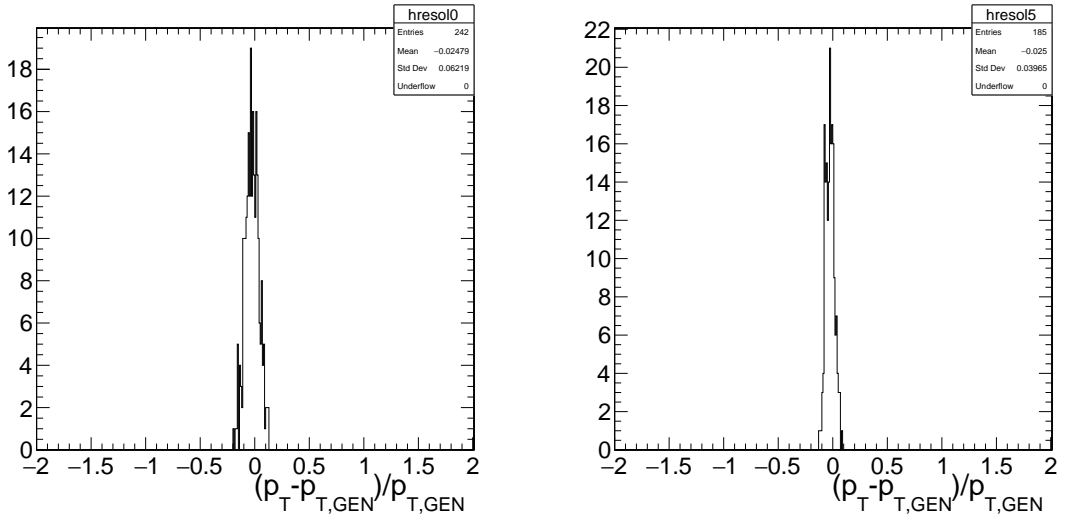


Figure 4.8: The jet energy resolution of neutrons with $0 < |\eta| < 0.5$ and $200 \text{ GeV} < p_T < 300 \text{ GeV}$ (left) or $700 \text{ GeV} < p_T < 800 \text{ GeV}$ (right).

10 In order to validate this method, the custom and standard neutron samples are used to compare the
11 two leading generator-level jets to the new jets from the custom sample, denoted as P2PF jets, and the PF
12 jets from the standard sample. This is illustrated in Figure 4.9, where the p_T of the generated neutrons is
13 shown on the horizontal axis, and the p_T of the reconstructed jet is shown on the vertical axis. The left
14 plot shows the standard neutron sample produced with the full GEANT simulation, while the right plot
15 shows the custom neutron sample where the neutron was directly converted into a neutral PF candidate.
16 The JER distributions are also compared in Figure 4.10 and fitted with a Crystal Ball function, showing
17 compatible parameters.

18 This demonstrates that the procedure, where the JER distributions derived from a neutron sample are
19 used to smear the PF candidates from generator-level SIMPs, can sufficiently accurately simulate SIMPs
20 in a realistic detector, assuming SIMPs are neutron-like. However, since this procedure directly converts
21 the generated SIMPs into PF candidates, the SIMPs do not interact in the Tracker and the resulting jets

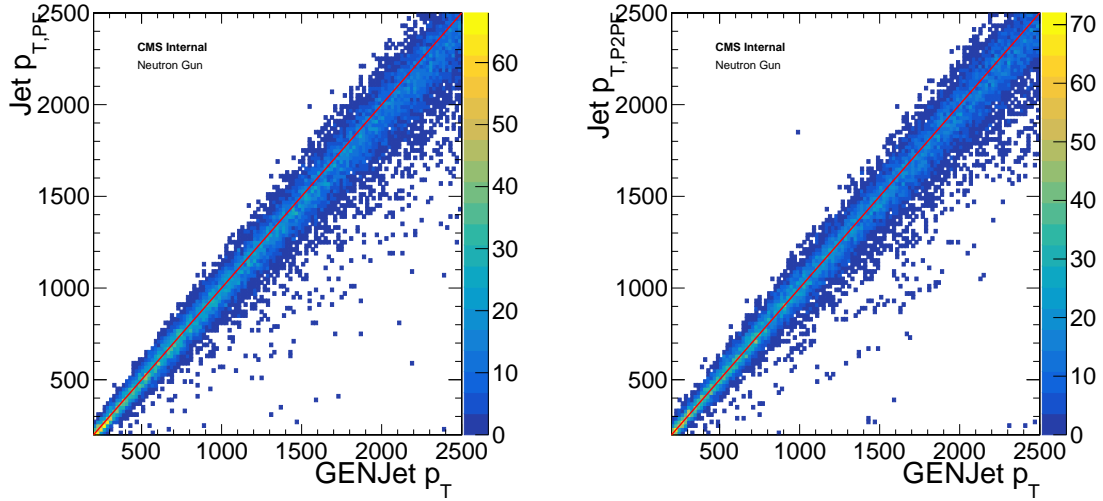


Figure 4.9: Comparison of the transverse momentum of the generator-level jets to the PF jets (left) and P2PF jets (right) in the region $0 < |\eta| < 0.5$ with jet energy resolution smearing, using a neutron sample.

1 have a very steeply falling charged hadron energy fraction (CHF) distribution. This gives an optimistic
2 image, which translates in a maximal signal efficiency.

3 The SIMP signal simulation and reconstruction was therefore further improved by moving to the sec-
4 ond approach. In this method, the generated SIMP particles are not converted into neutral PF candidates,
5 but they are instead replaced by neutrons, keeping the SIMP kinematics. The standard reconstruction and
6 full GEANT simulation can then be applied, since the neutrons are correctly recognized and simulated.
7 In this case, interactions will happen inside the Tracker as well and the resulting jets will contain a larger
8 CHF, as is shown in Figure 4.11.

9 This method gives a good approximation of a SIMP signal, since the shower generated by the SIMP
10 is in principle contained inside the calorimeters, as the model described in Section 2.3 is constructed so
11 that for a specific choice of couplings the SIMPs may be detected as a regular hadrons. Although the
12 considered SIMP-nucleon interaction is repulsive, this does not differ considerably from known attrac-
13 tive interactions at the probed high energies. The incoming SIMP hits a nucleon at rest in the calorimeter,
14 breaking it up, and because of the large incoming momentum, there is a boost forward into the calorimeter
15 and the shower starts. The cross section would therefore be identical for a repulsive or attractive interac-
16 tion and the effect on the shower is negligible since the scattering angle is very small due to the momentum
17 boost. Furthermore, the higher the momentum of the SIMP, the shorter the distance it travels to deposit
18 its characteristic momentum. With the considered couplings, the depth containing a SIMP with 500 GeV
19 momentum is below 1 m, within the calorimeter. Most of the energy will therefore be deposited in the
20 first interaction with the material. Given the expected forward energy flow in the calorimeter shower, and
21 the shower containment achieved by the choice of couplings in the simplified model, the shower induced
22 by the SIMP interaction can to first order be modelled by the interaction of a high-momentum neutral
23 hadron, like a neutron.

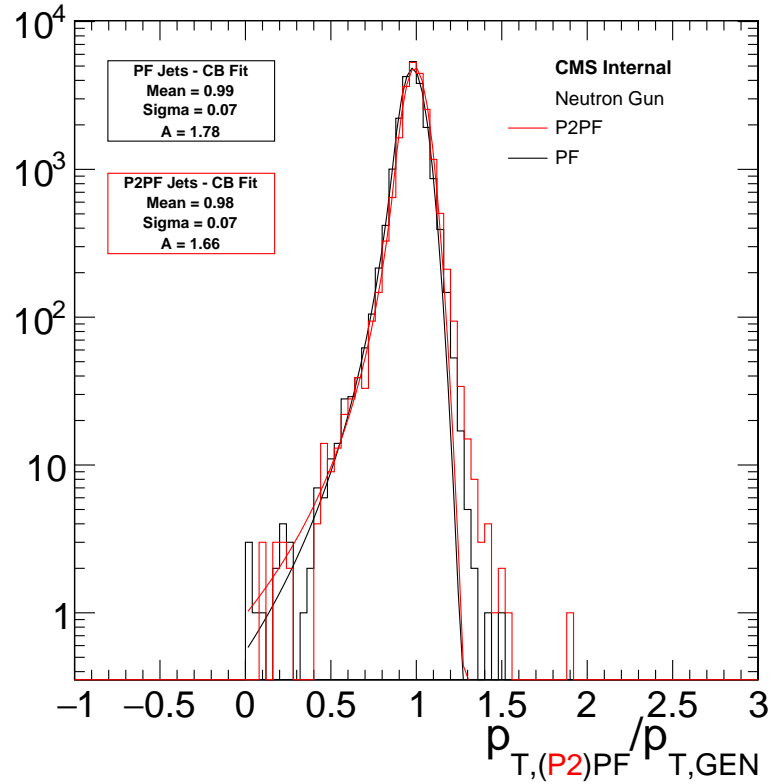


Figure 4.10: The jet energy resolution of the corrected P2PF jets (red) and PF jets (black), fitted with a Crystal Ball function.

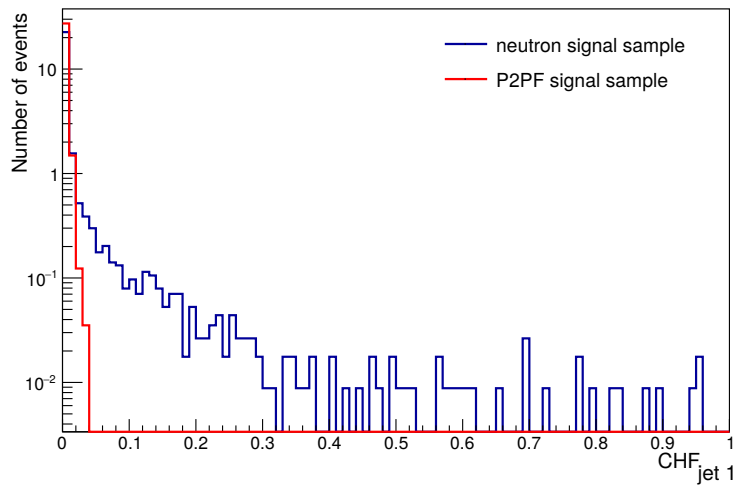


Figure 4.11: CHF distribution of the leading jet, for a signal sample produced with the first approach (red) and the corresponding sample produced using the second method (blue).

5

1

2

The Monojet Analysis

3 As has been described in Chapter 2, there are many searches for dark matter both at particle accelerators
4 and elsewhere. At the LHC, one very promising channel is the monojet search, where the detection of
5 dark matter is done by looking for missing energy in association with one or more jets. The dark matter
6 particles are expected to pass through the detector without leaving any signal since they are neutral and
7 only interact very weakly. They can however be detected indirectly as missing energy when they recoil
8 off one or more jets coming from initial state radiation.

9 First, the used physics objects are described in Section 5.1. Next, the selection of the events using the
10 trigger is described in Section 5.2, and the subsequent event selection performed with fully reconstructed
11 events is detailed in Section 5.3. The estimation of the background and the included systematic uncer-
12 tainties are described Section 5.4 and 5.5, respectively. In Section 5.6, the obtained results are shown.
13 The improvements achieved by going from the analysis strategy used in 2015 to the 2016 version are
14 detailed in Section 5.7. Finally, the results are interpreted in terms of the considered dark matter models
15 in Section 5.8.

16 **5.1 Physics object reconstruction**

17 While jets are evidently important objects in this analysis, other physics objects are used as well. Leptons
18 and photons are for example vetoed in order to reject backgrounds, and are used to define the many
19 control regions used for the background prediction.

20 **5.1.1 Jets**

21 The method described in Section 4.3.7 is used to reconstruct the used PF jets, and the jet energy cor-
22 rections are applied as well. Furthermore, the jets are required to have $p_T > 30 \text{ GeV}$, and to pass the
23 loose jet identification and pileup jet identification described in Section 4.3.7. Additionally a jet cleaning
24 is applied by requiring a jet charged hadron energy fraction CHF > 0.1 and a jet neutral hadron energy
25 fraction NHF < 0.8 . The jets are also tagged as b-jets using the Combined Secondary Vertex algorithm
26 described in Section 4.3.8, with the loose working point.

27 **5.1.2 Leptons**

28 Electrons are considered for the lepton veto if they pass the loose electron selection, described in Sec-
29 tion 4.3.3, and have $p_T > 10 \text{ GeV}$ and $|\eta| < 2.5$. Similarly, muons are required to pass the loose muon
30 identification described in Section 4.3.5 and to have $p_T > 10 \text{ GeV}$ and $|\eta| < 2.4$. In the case of tau lep-
31 tons, they are required to have $p_T > 15 \text{ GeV}$ and $|\eta| < 2.3$. They should also pass the tau identification

1 criteria, which require a jet with an identified subset of particles with a mass consistent with the decay
 2 products of a hadronic tau and which are isolated with a pileup corrected isolation cut requiring less than
 3 5 GeV of energy deposits within a radial cone of $\Delta R < 0.3$.

4 The selection of electrons and muons for the dielectron, dimuon, single electron, and single muon
 5 control regions is however stricter. In this case, at least one electron or muon is required to pass the tight
 6 identification.

7 5.1.3 Photons

8 Photons are required to have $p_T > 15$ GeV, $|\eta| < 2.5$, and to pass the loose identification criteria
 9 described in Section 4.3.3, in order to be considered for the photon veto. For the photon + jets control
 10 region, photons are required to pass the tight photon identification in order to be considered.

11 5.2 Trigger selection

12 In order to select events that have the Monojet signature displayed in Figure 5.1, the trigger requires either
 13 $E_T^{miss} > 90$ GeV, where E_T^{miss} is the magnitude of the negative vectorial sum of the p_T of all particles at
 14 trigger level, or $H_T^{miss} > 90$ GeV, where H_T^{miss} is calculated as the magnitude of the negative vectorial
 15 sum of the momenta of all jets with $p_T > 20$ GeV. In order to avoid collecting noise events, tight
 16 requirements are placed on the jets used in the H_T^{miss} computation. Jet energy correction are already
 17 applied at the HLT-level and the jet NHF is required to be smaller than 0.9. Muons are not taken into
 18 account to compute E_T^{miss} and H_T^{miss} , so that the same trigger can be used to select the events for the
 19 muon control regions used for the background prediction.

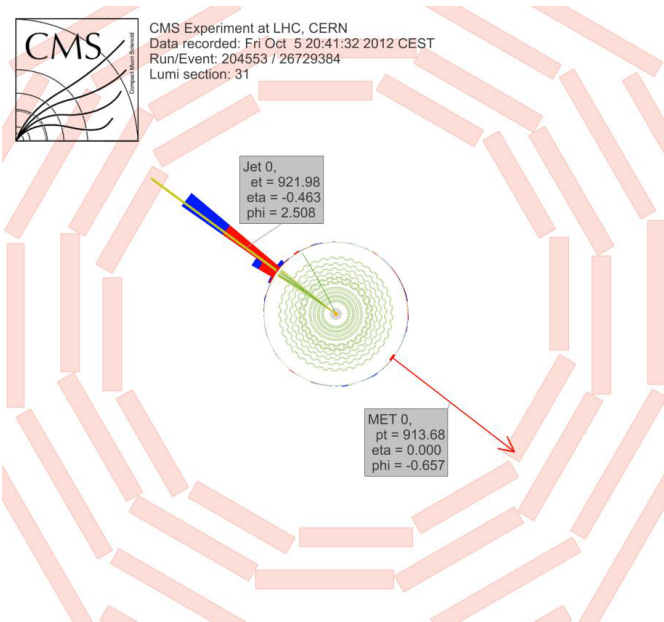


Figure 5.1: Event display showing the monojet final state.

20 This trigger is evaluated using events passing the single electron trigger with a threshold of $p_T >$
 21 23 GeV, and applying an extra offline selection requiring an electron with $p_T > 40$ GeV passing the
 22 tight identification and a jet with $p_T > 100$ GeV and $|\eta| < 2.5$. The trigger efficiency is computed by
 23 determining the fraction of events passing the signal triggers, as a function of the recoil. The efficiency is
 24 above 98% for events passing the analysis selection described below, as shown in Figure 5.2.

25 For the electron control regions, a single electron trigger was used with a threshold at $p_T > 27$ GeV.
 26 The efficiency of this trigger is determined as a function of p_T and η . This is done by tagging one
 27 electron and probing a second one, while requiring the invariant mass of this pair to correspond to the

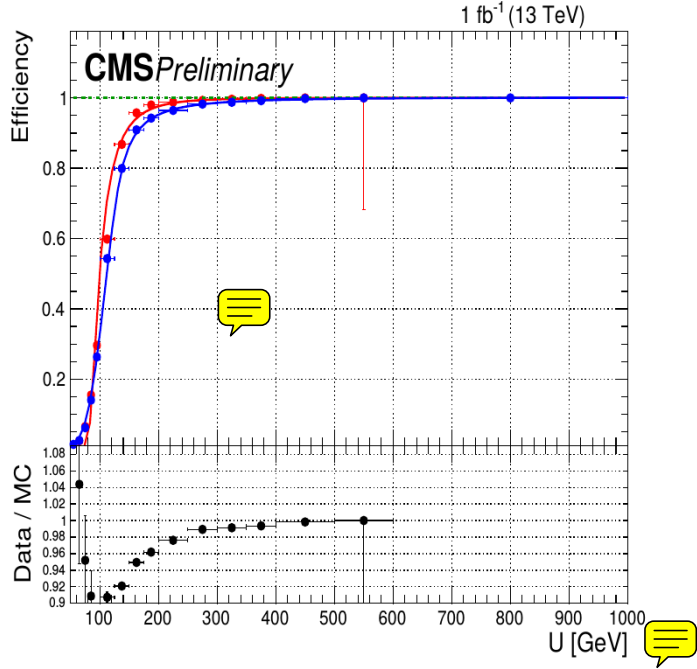


Figure 5.2: The efficiency of the used signal triggers as a function of the recoil, in MC (red) and data (blue).

1 Z boson mass. This tag-and-probe method ensures that backgrounds are removed and allows to measure
 2 the efficiency by simply taking the fraction of probes that passes the single electron trigger. The obtained
 3 trigger turn on curves as a function of the electron transverse momentum are shown in Figure 5.3 for the
 4 two η bins.

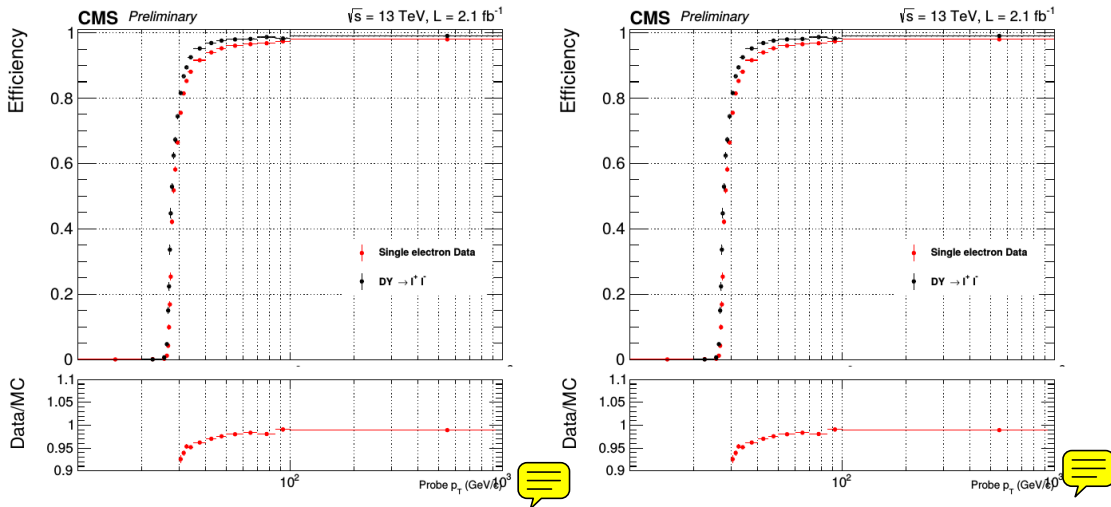


Figure 5.3: The efficiency of the single electron trigger in data (red) and MC (black) for $|\eta| < 1.4442$ (left) and $1.566 < |\eta| < 2.5$ (right).

5 Finally, the events in the photon control region are selected with a single photon trigger requiring an
 6 isolated photon with $p_T > 175$ GeV. The performance of this trigger is measured using data selected
 7 with a looser single photon trigger.

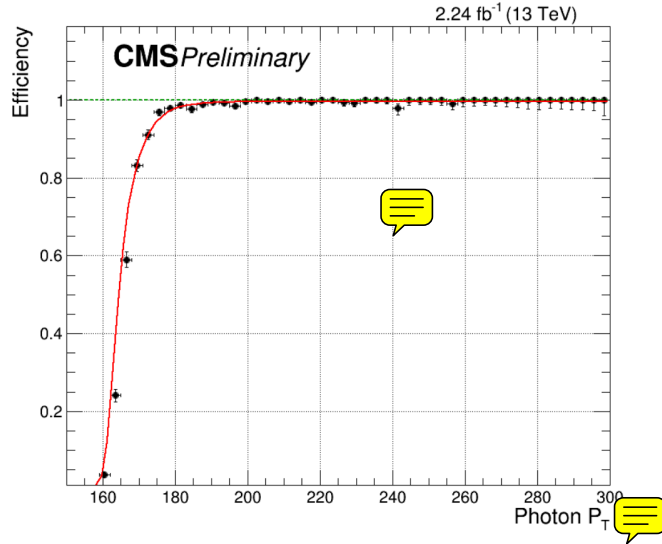


Figure 5.4: The efficiency of the single photon trigger measured in data.

5.3 Event selection

Once the events have been fully reconstructed and the jets in the event have been corrected as described in Section 4.3.7, an event selection is applied by requiring the missing transverse energy E_T^{miss} defined in Section 4.3.10 to be larger than 200 GeV in order to be consistent with the trigger turn-on. Additionally, the leading jet is required to have $p_T > 100$ GeV, and $|\eta| < 2.5$. A cut on the difference in azimuthal angle between the E_T^{miss} and the first four leading jets of $\Delta\phi(jet, E_T^{miss}) > 0.5$ is also applied to suppress the QCD background from mismeasurements of jet momentum or detector noise. The events are further cleaned by applying quality filters to remove events with badly reconstructed missing transverse energy. Finally, events containing a lepton, a photon, or a b-jet are vetoed as well. Figure 5.5 shows the E_T^{miss} distribution for the data and background prediction, after applying the described selection.

The leptons are vetoed to suppress the electroweak backgrounds, such as $W(l\nu) + \text{jets}$ and semileptonic diboson decays, while the photon veto is added to suppress the $Z(\nu\nu) + \text{photon} + \text{jets}$ and $W(l\nu) + \text{photon} + \text{jets}$ background processes, and to ensure there is no overlap with a similar dark matter search which investigates the final state consisting of missing energy and a photon. This rejects less than 1% of the signal. Finally, the b-jet veto reduces the top background by a factor 3 and only reduces the signal by 5 to 10%, depending on the type and mass of the mediator. No additional veto on the number of jets is applied.

5.4 Background estimation

The dominant background comes from $Z + \text{jet events}$ where the Z boson decays to two neutrinos. This produces the same signature of jets with missing energy as the signal, and results in an irreducible background. The second largest background consists of $W + \text{jets}$ events with a leptonically decaying W boson. This background is already suppressed by the lepton veto, but a fraction of these events remain when the lepton is either not identified or outside of the detector acceptance. The remaining background events come from top quark decays, which are suppressed by the b-jet veto, semileptonic diboson (WW , WZ , and ZZ) decays, and QCD multijet events. The two main background contributions are estimated from five control regions in data consisting of dimuon, dielectron, single muon, single electron, and photon + jets events. The E_T^{miss} in these control regions is redefined in order to imitate the E_T^{miss} shape in the signal region. This hadronic recoil U is obtained by removing the leptons or the photon from the E_T^{miss} computation. The contributions from top quark decays and semileptonic diboson decays are estimated using simulated samples, while the QCD multijet background is estimated using a data-driven approach.

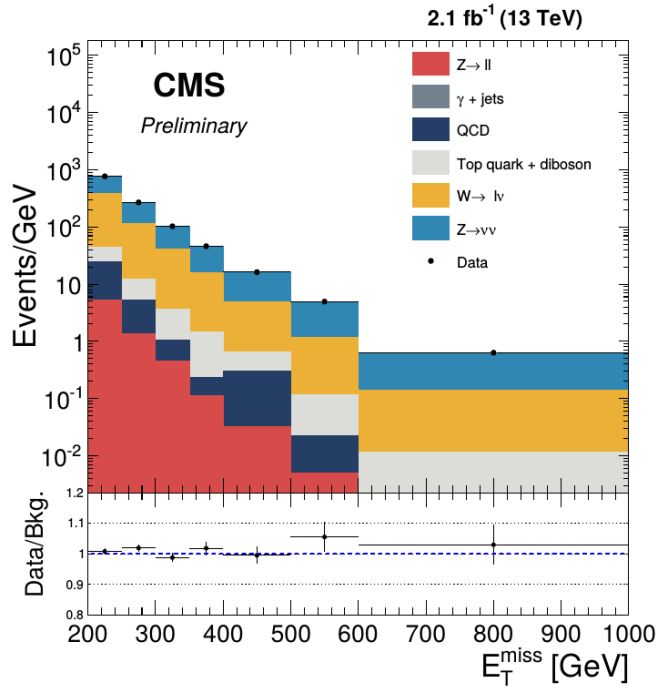


Figure 5.5: The missing transverse energy distribution after applying the described event selection, for the data and the predicted backgrounds.

5.4.1 The Z and W background estimation

The yield of $Z(\nu\nu)$ and $W(l\nu) + \text{jets}$ events in the signal region is estimated from five control regions by using the ratio between data and MC in the control region, per bin of the recoil distribution. For the prediction using $Z \rightarrow \mu\mu$ events in the dimuon control region for example, the predicted yield of $Z \rightarrow \nu\nu$ events is given by

$$N_{Z(\nu\nu)} = \frac{N_{Z(\mu\mu)}^{data}}{N_{Z(\mu\mu)}^{MC}} N_{Z(\nu\nu)}^{MC} \quad (5.1)$$

$$= \frac{N_{\mu\mu}^{data} - N_{Bkgd}}{N_{Z(\mu\mu)}^{MC}} N_{Z(\nu\nu)}^{MC} \quad (5.2)$$

$$= \frac{N_{\mu\mu}^{data} - N_{Bkgd}}{N_{Z(\mu\mu)}^{MC}} R_{Z(\mu\mu) \rightarrow Z(\nu\nu)} N_{Z(\mu\mu)}^{MC} \quad (5.3)$$

- 2 The transfer factors, denoted by R , are derived from simulation and take into account the impact of lepton
 3 acceptance and efficiency, as well as the additional E_T^{miss} requirement for the single electron control
 4 region. They also include the difference in branching ratio and the relation between the differential cross
 5 sections of the photon, W , and Z boson production as a function of the boson p_T . The transfer factors
 6 are computed as a function of the recoil, and are shown for the five different control regions in Figure 5.6.
 7 Furthermore, the Z/W ratio shown in the bottom right plot of Figure 5.6 provides an additional constraint
 8 since the single lepton control regions are also used to estimate the $Z(\nu\nu) + \text{jets}$ background.

9 The simulated samples used for the background estimation are generated at leading order (LO) using
 10 the **MADGRAPH generator**, and corrected to next-to-leading order (NLO). These corrections introduce an
 11 additional systematic uncertainty, but are crucial in order correctly represent the data, since the simulation
 12 is approximately 40% higher than the data when using only LO calculations. The NLO QCD k-factors
 13 are derived from samples generated at NLO with **MADGRAPH5_aMC@NLO**, while the electroweak k-
 14 factors are obtained from theoretical calculations [130–133]. The differential cross section as a function
 15 of the boson p_T is shown in Figure 5.7 for photon, W , and Z production, and the obtained k-factors

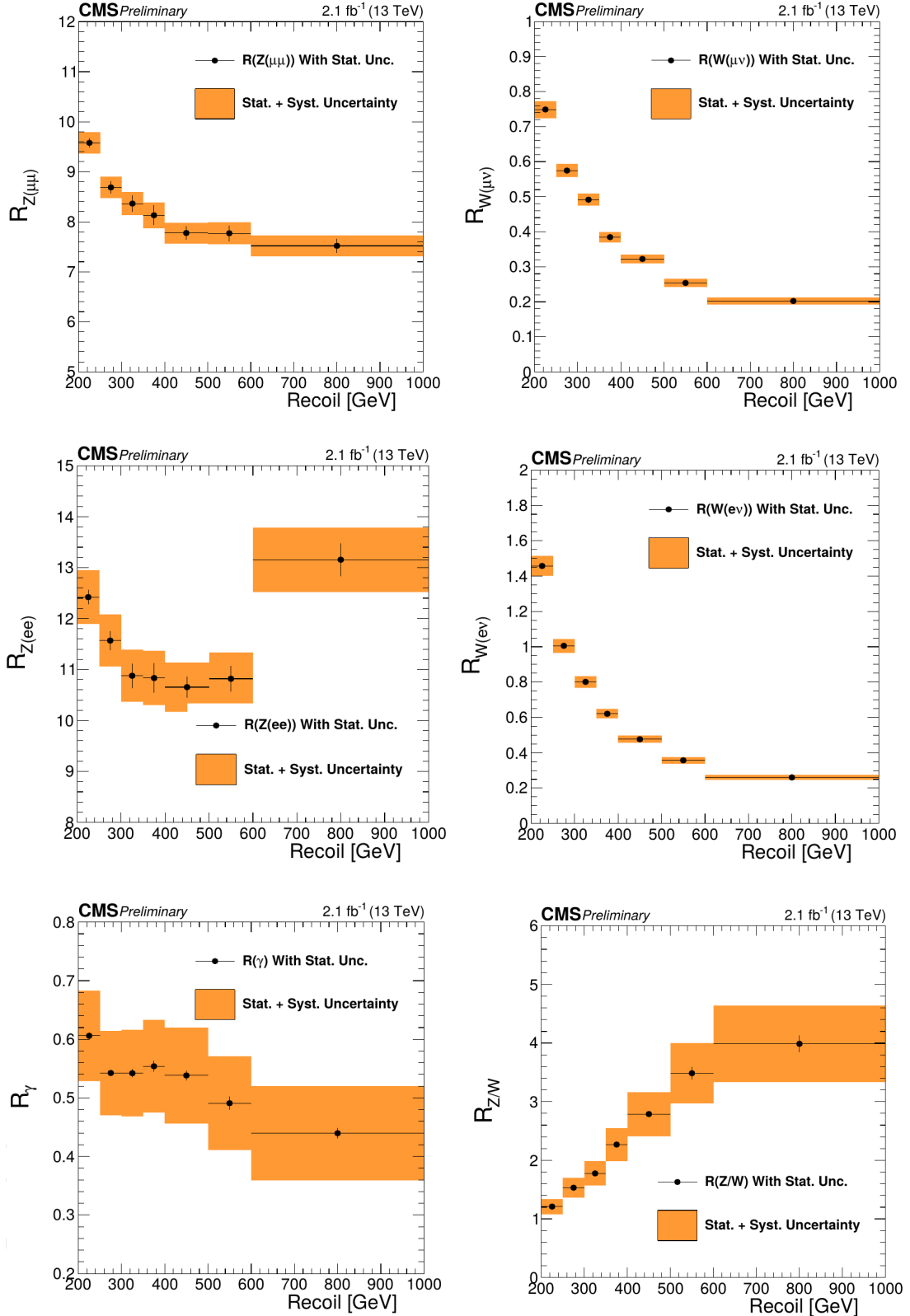


Figure 5.6: Transfer factors for the dimuon (top left), single muon (top right), dielectron (middle left), single electron (middle right), and photon + jets (bottom left) control regions. The ratio of the Z and W transfer factors is shown in the bottom right plot.

1 are displayed in the ratio plots. More details on the different control regions are given in the following
 2 ~~description~~.

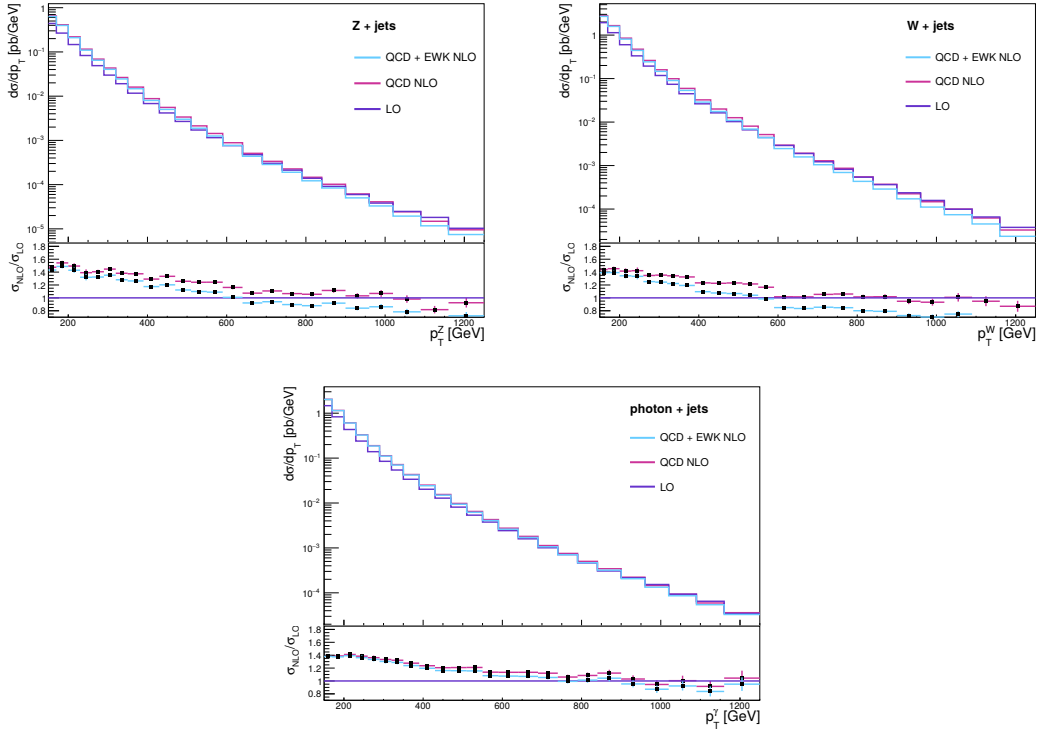


Figure 5.7: The differential cross section as a function of the boson p_T for photon, W , and Z production, with the resulting k -factors in the ratio plots.

Dimuon control region

The traditional control region for the Z boson background is the dimuon control region. This region is dominated by $Z \rightarrow \mu\mu$ events, which are very similar to the $Z(\nu\nu) + \text{jets}$ background events, the only difference being the decay mode. The production mode and kinematics in the control region are very similar, as well as the acceptance. However, the branching ratio of the Z boson into two muons is 6 times smaller than the branching ratio to **two neutrinos**. As a result, the dimuon control region contains about 10 times less Z boson events than the signal region. In order to improve this statistical limitation, other control regions have been added as well.

In the dimuon control region the events are selected using the monojet triggers and applying the same requirements as described in Section 5.3 for the signal region, using the recoil instead of the missing transverse energy, except for the muon veto. **Additionally, exactly two muons with opposite charge and with $p_T > 10$ GeV should be identified using the loose identification. The leading muon should have a transverse momentum large than 20 GeV, and at least one muon should pass the tight selection requirements.** Finally, the dimuon mass should be between 60 and 120 GeV, corresponding to the Z boson mass.

Single muon control region

In order to model the second largest background, coming from $W(l\nu) + \text{jets}$ events, a single muon control region is **typically** used. This control region is in addition also used to constrain the $Z(\nu\nu) + \text{jets}$ background. The events in the single muon control region are required to pass the monojet triggers and event selection replacing the E_T^{miss} by the recoil obtained by removing the muon, except for the muon veto. One muon should then pass the tight selection requirements and have $p_T > 20$ GeV.

1 **Dielectron control region**

2 The dielectron control region is used to constrain the $Z \rightarrow \nu\nu$ background. The events are selected
 3 by the single electron triggers. Similarly to the dimuon control region, the events are required to
 4 pass the monojet selection, except for the electron veto. Instead, exactly two electrons with $p_T >$
 5 10 GeV are required to pass the loose identification described in Section 4.3.3. In addition, at least
 6 one electron should pass the tight selection requirements, and the leading electron is required to
 7 have $p_T > 40$ GeV in order to be consistent with the single electron trigger. Finally, the dielectron
 8 mass should be between 60 and 120 GeV, in order to be consistent with a Z boson decay. The
 9 jump that can be observed in the last bin of the resulting transfer factor in the middle left plot of
 10 Figure 5.6 is due to the isolation requirement of the single electron trigger. This was verified by
 11 removing the trigger selection in MC, yielding a flat transfer factor.

12 **Single electron control region**

13 The single electron control region is used to constrain the $W(l\nu) + \text{jets}$ background. In the single
 14 electron control region, the events are required to have one electron with $p_T > 40$ GeV passing
 15 the tight selection requirements, analogously to the single muon control region. In this region, a
 16 large amount of QCD background is however present. In order to reject most of those events, an
 17 additional cut on the E_T^{miss} , which includes the single electron, is added at 50 GeV. This reduces
 18 the QCD background by an order of magnitude.

19 **Photon + jets control region**

20 Due to its large yield, photon + jets control region provides the dominant constraint on the high- p_T
 21 part of the $Z(\nu\nu) + \text{jets}$ background. The selection of these events is done using the single photon
 22 triggers and applying the monojet selection, except for the photon veto. One photon is then required
 23 to pass the tight identification and to have $p_T > 175$ GeV. Additionally, it should be reconstructed
 24 inside the ECAL barrel ($|\eta| < 1.4442$) in order to achieve a high purity of 95%. Events with
 25 more than one photon passing the loose identification requirements described in Section 4.3.3 are
 26 rejected.

27 **5.4.2 The QCD background estimation**

28 While QCD multijet background events are generally well balanced in the transverse plane, missing trans-
 29 verse energy can arise in the event due to jet energy mismeasurements, punch-through, uninstrumented or
 30 defective regions in the detector, hot spots, or neutrinos from decays of heavy-flavour mesons. Although
 31 these effects are very rare, the QCD production cross section is gigantic and some events can be selected
 32 at high missing transverse energy. The event selection detailed in Section 5.3 was designed to suppress
 33 contributions from the QCD multijet background, reducing it to the percent level. However, this back-
 34 ground is not well reproduced in the simulation, and thus requires a background estimation using a data
 35 control region.

36 The yield is predicted by combining two different approaches, namely the “rebalance and smear”
 37 technique and the $\Delta\phi$ extrapolation method. The rebalance and smear technique uses a kinematic fit with
 38 the constraint that no missing transverse energy is present in the event. The event is then rebalanced by
 39 varying each jet and the remaining hadronic recoil within their computed uncertainties. The resulting
 40 jets are then smeared with the measured jet resolution, and the prediction for the QCD E_T^{miss} distribu-
 41 tion is obtained. For the $\Delta\phi$ extrapolation method, the QCD background is estimated in the region with
 42 an inverted $\Delta\phi$ selection cut, $\min \Delta\phi(\text{jet}, E_T^{\text{miss}}) < 0.5$, and then translated to the signal region us-
 43 ing transfer factors derived from simulated events. The obtained estimation using this method yields a
 44 contribution that is a factor 2 larger than the prediction from simulation, which agrees well with the the
 45 rebalance and smear technique, as can be seen in Figure 5.8.

46 **5.4.3 Simulation-based background estimation**

47 Contributions are also expected from diboson production, from t quark decays, both from $t\bar{t}$ and single
 48 top production, and from $Z(l\ell) + \text{jets}$ events where the leptons are not detected. These backgrounds are

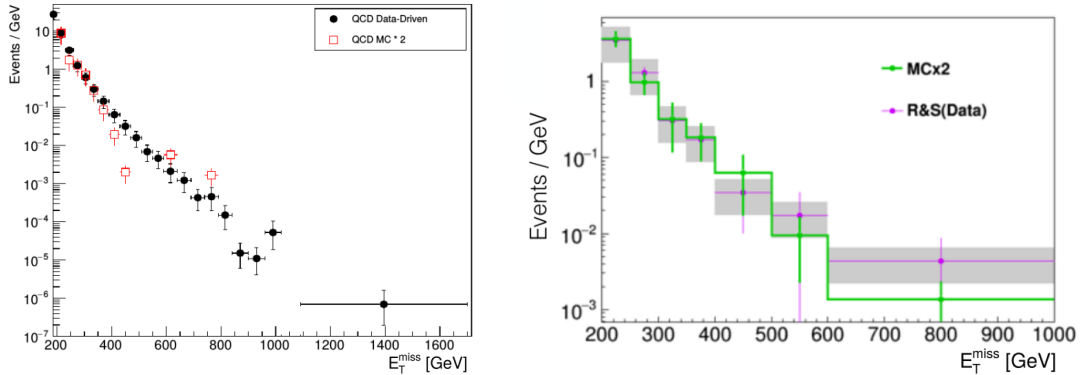


Figure 5.8: Predicted E_T^{miss} distribution of the QCD multijet background obtained using the $\Delta\phi$ extrapolation method (left) and the rebalance and smear technique (right), using data (black) and MC simulations (red). The simulation is scaled by a factor 2.

1 estimated from MC simulations.

2 Top quarks typically decay into a W boson and a b quark. When the W boson decays leptonically,
 3 a neutrino is produced, generating genuine missing transverse energy. If the event is not removed by the
 4 b -jet veto and the lepton is not identified, this type of events contributes to the background in the signal
 5 region. However, due to the small production cross section and the applied event selection, only a small
 6 fraction of these events are selected. In order to estimate the contribution of this background, a $t\bar{t}$ sample
 7 has been produced at LO with MADGRAPH, and single top events were generated with PowHEG at NLO.

8 When one of the weak bosons produced in diboson events decays leptonically, generating one or more
 9 neutrinos, and the other one decays hadronically, jets and missing transverse energy are produced. The
 10 samples used to estimate this background have been produced using PYTHIA.

11 Finally, when the leptons in $Z(l\bar{l}) + \text{jets}$ events are lost or out of the detector acceptance, these events
 12 can mimic the monojet signature as well. MC samples have been generated at LO using MADGRAPH in
 13 several bins of H_T in order to estimate the contribution from this sub-dominant background.

14 5.5 Systematic uncertainties

15 For the main backgrounds, multiple systematic uncertainties on the transfer factors are taken into account.
 16 Experimental uncertainties are added for the muon efficiency, the electron efficiency, the lepton veto, the
 17 photon efficiency, and the photon purity in the photon + jets sample.

18 Uncertainties are also added from theory, to take into account variations of the factorization and renor-
 19 malization scales, PDF uncertainties, and the NLO electroweak corrections. The former 3 uncertainties
 20 are shown in Figure 5.9 for the $Z + \text{jets}$, $W + \text{jets}$, and photon + jets samples. The uncertainties are then
 21 propagated to the transfer factors, and are displayed in Figure 5.10. To evaluate the PDF uncertainty, the
 22 samples are reweighted with event-by-event scale factors representing the shift in the kinematic distribu-
 23 tions from variations in the PDF. The transfer factors are then produced for each variation, and the RMS
 24 of the variation is taken as PDF uncertainty. Similarly, the renormalization and factorization scales are
 25 varied up and down by a factor 2, and the uncertainties are derived from the resulting transfer factors. For
 26 the electroweak corrections, the full correction is taken as an uncertainty.

27 For the remaining sub-dominant backgrounds, systematic uncertainties are included to take into ac-
 28 count the uncertainties from the jet energy scale and the jet energy resolution of the jets. Additionally,
 29 systematic uncertainties of 10%, 29%, and 50% are added to account for the uncertainty on the pro-
 30 duction cross section of the top, diboson, and QCD processes, respectively. For the top backgrounds,
 31 a systematic uncertainty of 4% is included as well, due to the uncertainty on the b -tagging applied for
 32 the b -jet veto. Finally, a systematic uncertainty of 5.5% is added for all backgrounds derived from MC
 33 simulations, to take into account the luminosity measurement.

34 Lastly, for the signal models, systematic uncertainties are included for the luminosity and to take

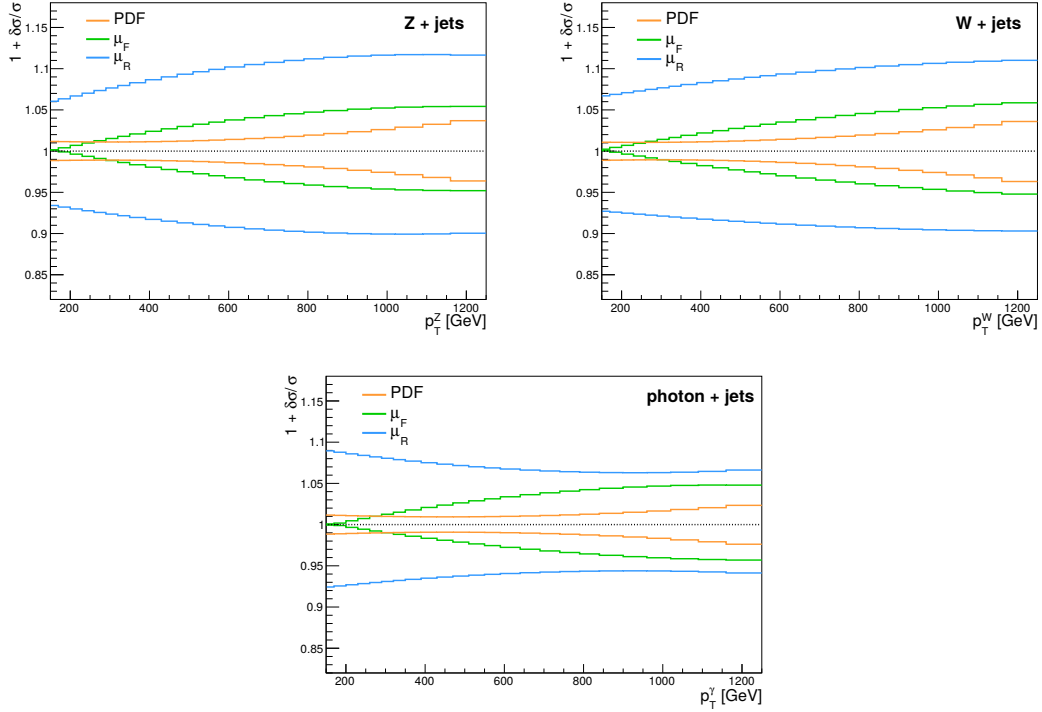


Figure 5.9: The PDF, renormalization, and factorization scale uncertainties for the $Z + \text{jets}$ (top left), $W + \text{jets}$ (top right), and photon + jets (bottom) samples. The uncertainties from the renormalization and factorization scales are obtained by separately varying them up and down by a factor 2.

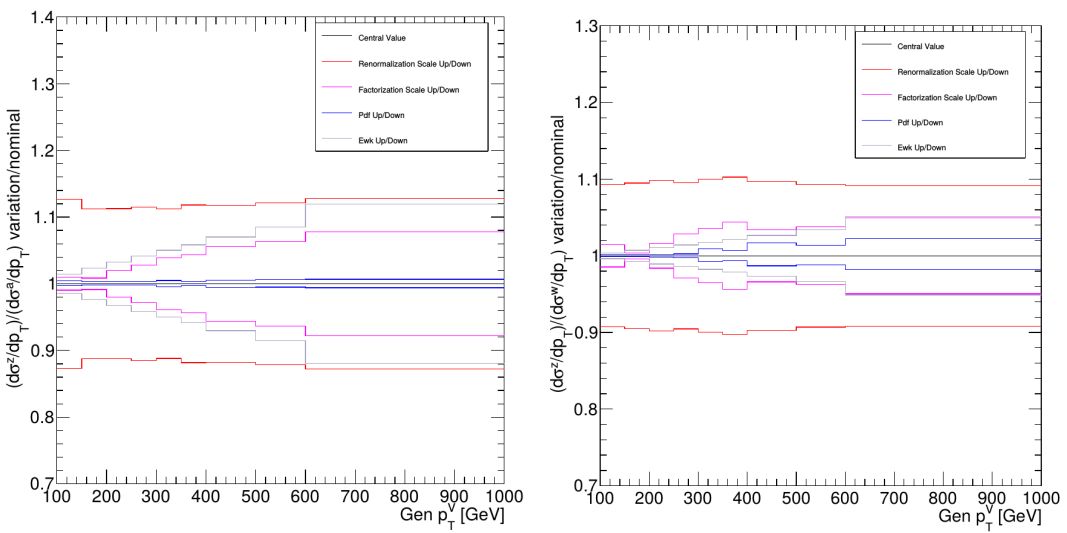


Figure 5.10: The theoretical uncertainties on the Z/γ (left) and Z/W (right) transfer factors.

1 into account the uncertainties from the jet energy scale and the jet energy resolution. The systematic un-
 2 certainties coming from variations of the factorization and renormalization scales and PDF uncertainties
 3 amount to 20% for the vector and axial signal samples and 30% for the scalar and pseudoscalar signals.

4 **5.6 Results**

5 The results are extracted by performing a binned fit to the missing energy spectrum, fitting simultane-
 6 ously over the five control regions and the signal region, under a given signal hypothesis. This is done
 7 using the CL_S criterion [134, 135], using the asymptotic approximation of the test statistic distributions
 8 implemented in the RooStat-based Combine tool and modelling the systematic uncertainties described in
 9 Section 5.5 as nuisance parameters. The nuisance parameter uncertainties are propagated as shape and
 10 normalization variations of the $Z(\nu\nu) + \text{jets}$ and $W(l\nu) + \text{jets}$ background. In Figure 5.11, the nuisance
 11 parameters and their uncertainties are shown before and after the fit to the data in the control regions.
 12 Before the fit they are all centred at 0 and have an uncertainty of 1. After the fit, the two largest pulls
 13 originate from the statistical uncertainty on the Z/W transfer factor and the uncertainty on the muon
 14 scale factor, but no significant tension is present in the fit and most nuisance parameters are not pulled or
 15 constrained by the fit.

16 Figures 5.12 and 5.13 show the recoil distributions in the different control regions, before and after the
 17 fit. The photon + jets control region, which has the largest yields, drives the fit and the post-fit prediction
 18 therefore corresponds well with the data. A good agreement is observed in all control regions, and the
 19 overall change in the transfer factors is relatively small.

20 Table 5.1 gives the background prediction for the various background processes in bins of missing
 21 transverse energy, using a background-only fit. Correspondingly, the fit under the background-only hy-
 22 pothesis is shown in Figure 5.14 and a good agreement is observed between the data and the prediction.
 23 The uncertainty on the recoil is below 10% for all bins.

Process	E_T^{miss} [200 – 250] GeV	E_T^{miss} [250 – 300] GeV	E_T^{miss} [300 – 350] GeV	E_T^{miss} [350 – 400] GeV	E_T^{miss} [400 – 500] GeV	E_T^{miss} [500 – 600] GeV	E_T^{miss} [> 600] GeV
$Z(\nu\nu) + \text{jets}$	19521	7473	3085	1447	1126	350	184
$W(l\nu) + \text{jets}$	15422	4793	1728	650	428	104	47.9
$Z(l\bar{l}) + \text{jets}$	259	67	22.4	5.1	3.0	0.44	0.12
Top	715	240	73.8	32.5	18.3	2.9	2.5
Dibosons	148	38	8.2	2.3	0.61	0.66	0.07
QCD	773	346	157	77	64	19.5	15.8
Total	36837 ± 246	12958 ± 115	5075 ± 63	2214 ± 38	1639 ± 33	478 ± 14	250 ± 12
Observed	36858	13010	4981	2248	1614	484	260

Table 5.1: Post-fit background predictions in the signal region and observed yield. The predictions and uncertainties are obtained from the background-only simultaneous fit in the signal and control regions.

24 **5.7 Improvements going from the 2015 to 2016 analysis**

25 An substantial difference going from the 2015 to the 2016 analysis is of course the increase in collected
 26 data, which allowed to reduce the statistical uncertainties and set stronger limits on the considered models.
 27 In the first Run 2 iteration of this analysis only 2.1 fb^{-1} of data was used, while 12.9 fb^{-1} were available
 28 for the second iteration in 2016.

29 An important addition the first Run 2 iteration of this analysis is the extension to the mono-V channel,
 30 which can give rise to a monojet-like signature. At high p_T , the production of a W or Z boson which
 31 then decays hadronically, can be effectively reconstructed as a single jet of large cone radius. However,
 32 in this section the focus will be on the improvements added to the monojet channel of the 2016 analysis,
 33 compared to the 2015 analysis.

34 One of the improvements that were added is the use of MC samples generated at leading order for the
 35 estimation of the main backgrounds. This was possible by generating samples that are binned in photon,

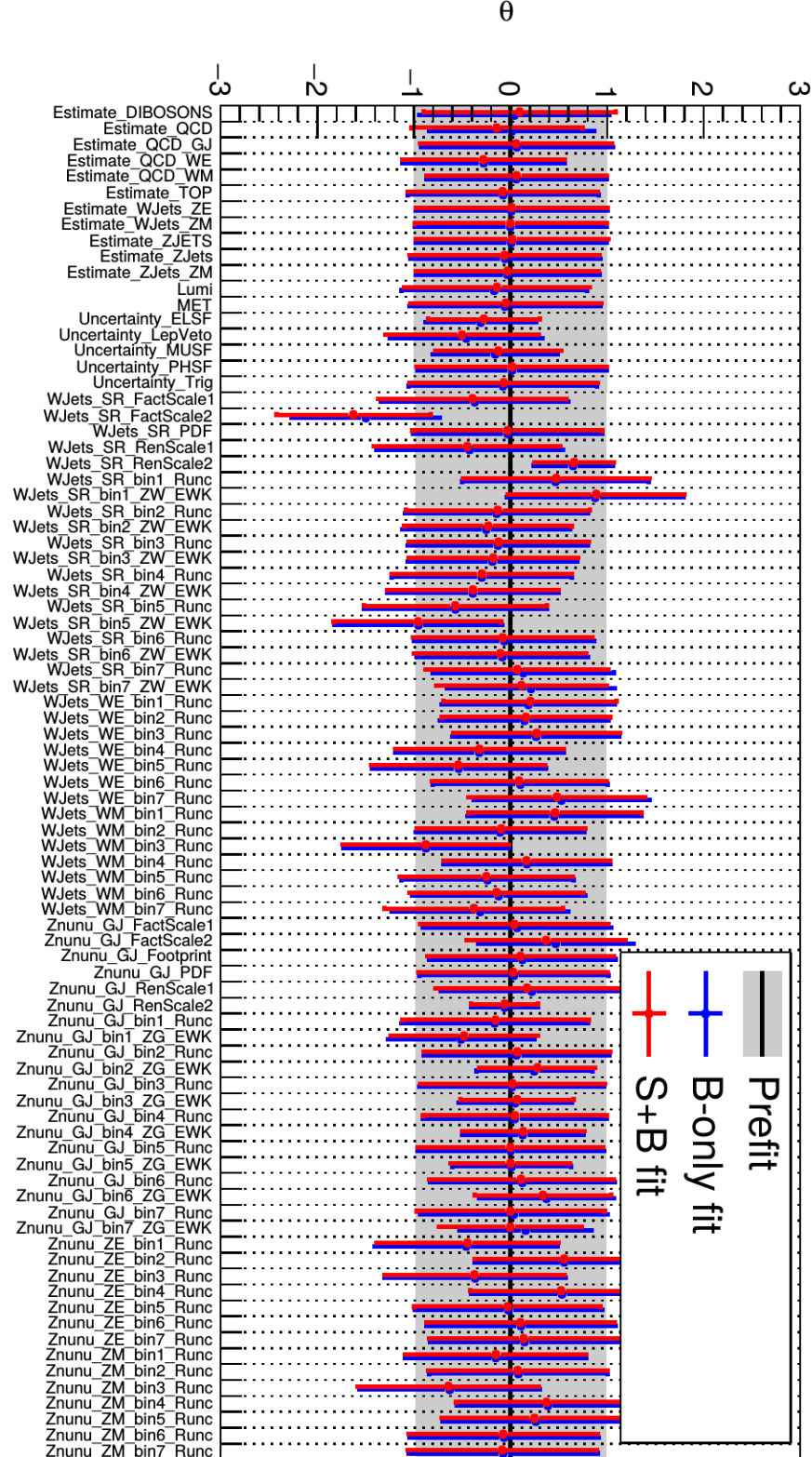


Figure 5.11: The post-fit nuisance parameters and their uncertainties, compared to the pre-fit values.

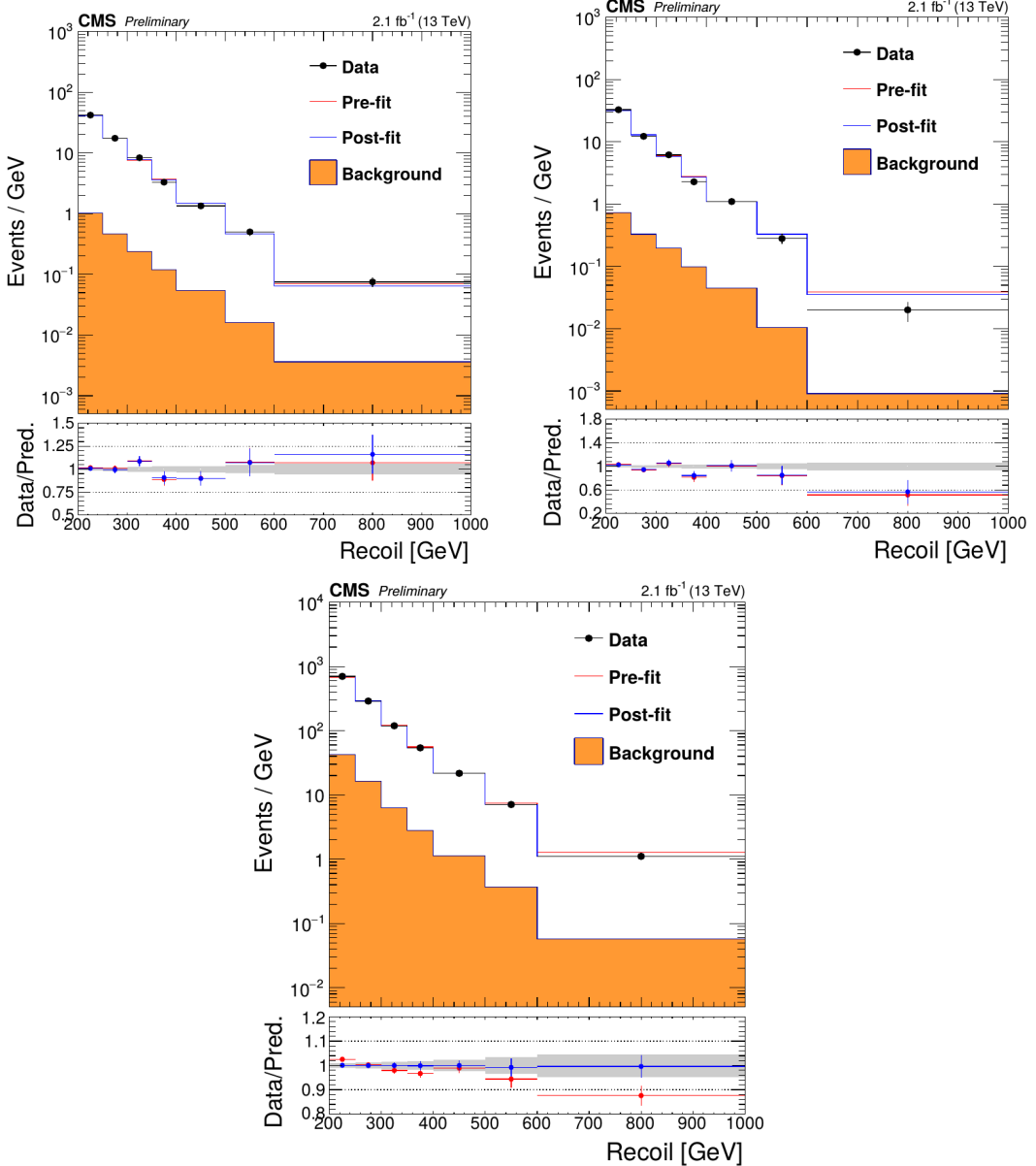


Figure 5.12: Comparison between data and prediction before (pre-fit) and after (post-fit) the simultaneous fit to the different control regions, in the dimuon (left), dielectron (right) and photon + jets (bottom) control regions. The grey band shows the uncertainty per bin, including all relevant systematic uncertainties.

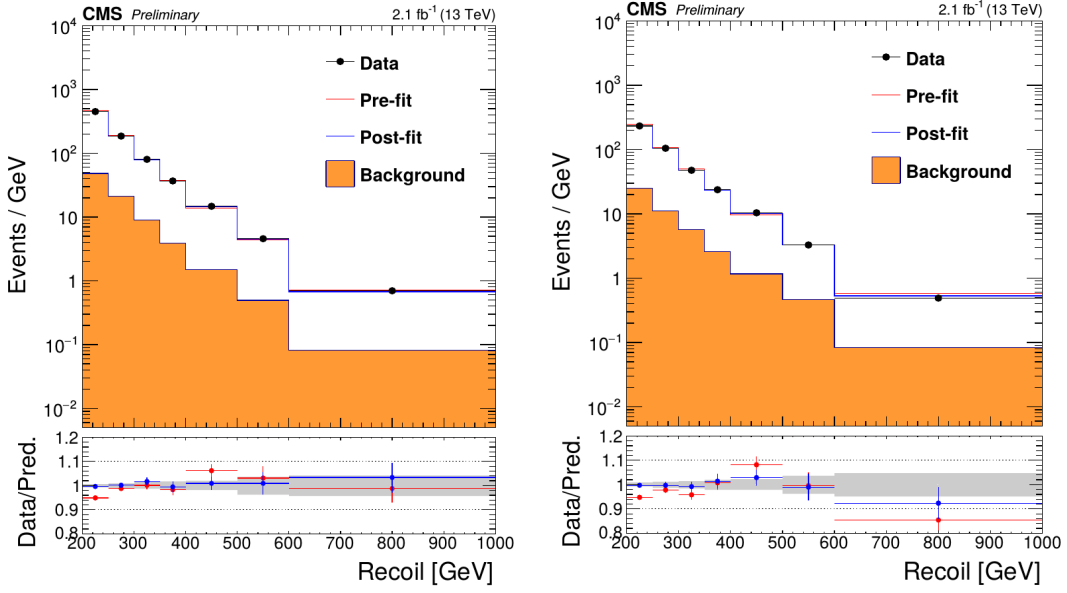


Figure 5.13: Comparison between data and prediction before (pre-fit) and after (post-fit) the simultaneous fit to the single lepton control regions, in the single muon (left) and single electron (right) control regions. The grey band shows the uncertainty per bin, including all relevant systematic uncertainties.

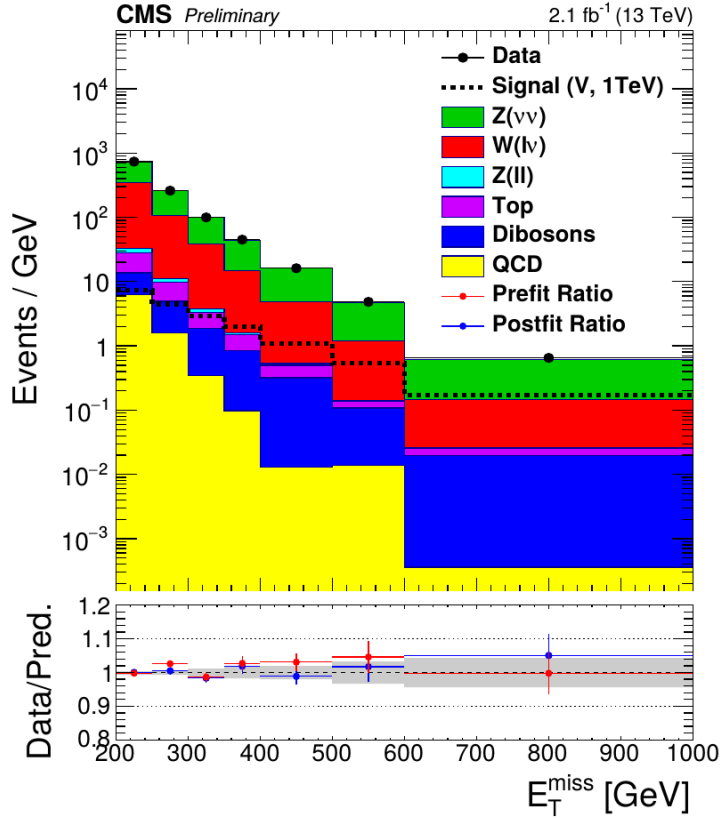


Figure 5.14: Post-fit missing transverse energy distribution for the expected backgrounds and the observed data in the signal region. The grey band indicates the post-fit uncertainty obtained from the background-only simultaneous fit in the signal and control regions.

¹ Z , or W boson p_T . As a result, no k-factors need to be applied to samples generated at LO and no
² additional systematic uncertainties need to be introduced for this.

³ 5.8 Interpretation

⁴ The results of the second iteration of this search, using the mono-V final state as well, are interpreted in
⁵ terms of simplified dark matter models assuming a vector, axial-vector, scalar, or pseudoscalar mediator
⁶ decaying to a pair of fermionic dark matter particles, as described in Section 2.2.4. As no significant
⁷ excess was observed, upper limits are placed 95% confidence level (CL) on the ratio of the signal cross
⁸ section to the predicted cross section, $\mu = \sigma/\sigma_{th}$. These limits are shown as a function of the mediator
⁹ mass (m_{med}) and the dark matter mass (m_{DM}) in Figures 5.15 and 5.16, for the four types of mediators.
¹⁰ The regions where the 95% CL upper limits on μ are less than one are considered to be excluded.

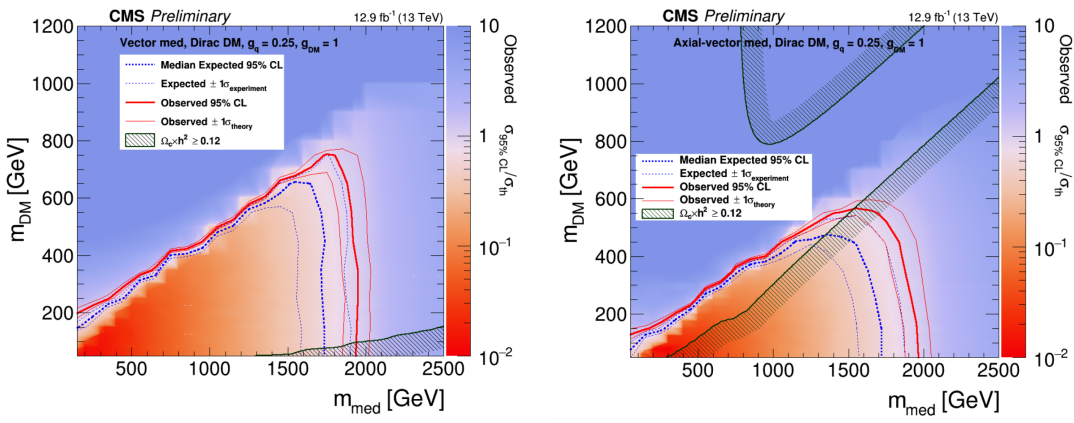


Figure 5.15: The 95% CL upper limits on the $\mu = \sigma/\sigma_{th}$ in the $m_{med} - m_{DM}$ plane, for a vector (left) or axial-vector (right) mediator. The cosmological constraints from the WMAP and Planck measurements of the CMB are shown as well.

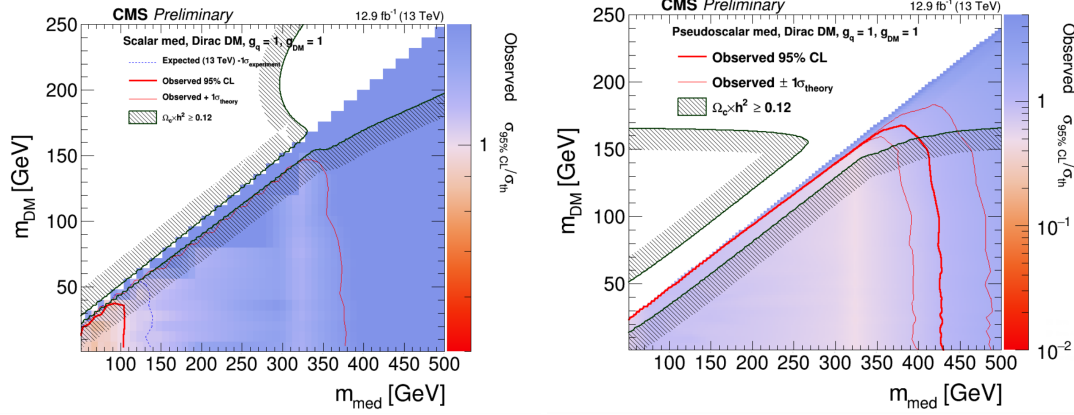


Figure 5.16: The 95% CL upper limits on the $\mu = \sigma/\sigma_{th}$ in the $m_{med} - m_{DM}$ plane, for a scalar (left) or pseudoscalar (right) mediator. The cosmological constraints from the WMAP and Planck measurements of the CMB are shown as well.

¹¹ For the vector and axial-vector models, mediator masses up to 1.95 TeV are excluded, while mediator
¹² masses up to 100 GeV and 430 GeV can be excluded for the scalar and pseudoscalar models, respectively.
¹³ Figures 5.15 and 5.16 also show the constraint from the observed cosmological relic density of dark
¹⁴ matter, which was determined from the WMAP and Planck CMB measurements. The expected dark
¹⁵ matter abundance is estimated using a thermal freeze-out mechanism and compared to the observed cold

dark matter density, assuming that the considered dark matter candidate is the dominant component of the observed dark matter.

The obtained limits can also be translated into 90% CL upper limits on the dark matter-nucleon scattering cross section $\sigma_{\text{SI/SD}}$, in order to compare them to results from direct detection experiments. The exclusion contours in the $m_{\text{DM}} - \sigma_{\text{SI/SD}}$ plane are obtained following the approaches outlined in [136–138], where σ_{SI} stands for spin-independent and σ_{SD} for spin-dependent dark matter-nucleon cross section. The resulting limits are shown in Figures 5.17 and 5.18.

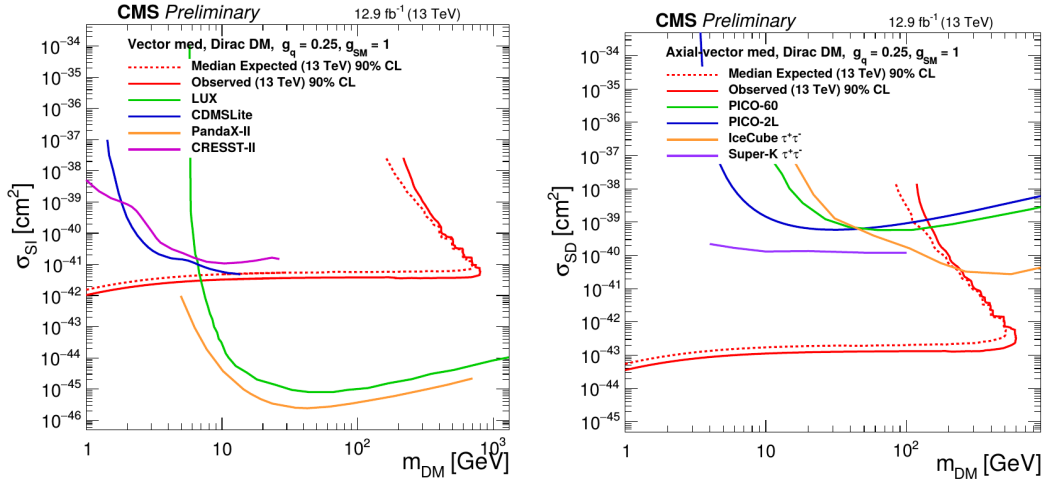


Figure 5.17: The 90% CL upper limits in the $m_{\text{DM}} - \sigma_{\text{SI/SD}}$ plane, for a vector (left) or axial-vector (right) mediator.

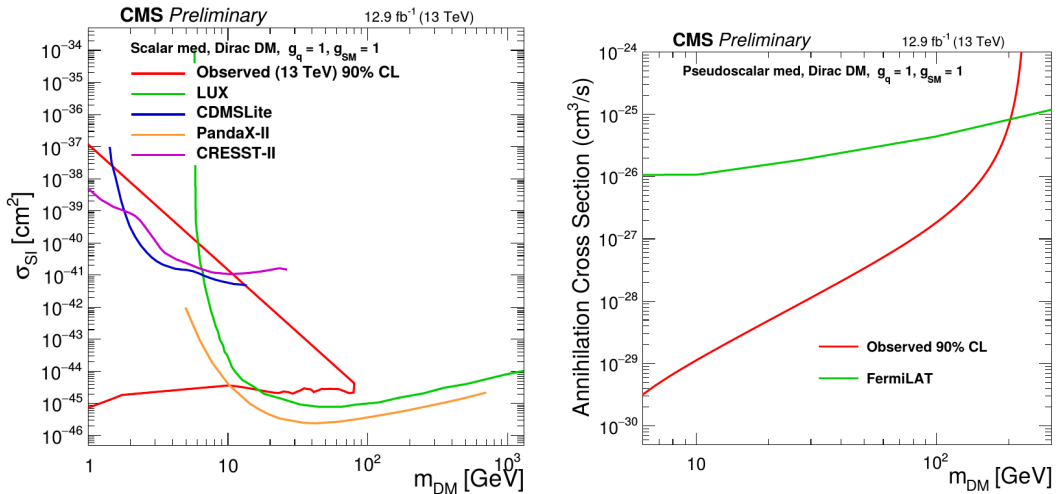


Figure 5.18: The 90% CL upper limits in the $m_{\text{DM}} - \sigma_{\text{SI/SD}}$ plane, for a scalar (left) or pseudoscalar (right) mediator.

For the vector and scalar mediators, the 90% CL upper limits on the spin-independent cross section are compared to results from the CDMSLite [139], LUX [140], PandaX-II [141], and CRESST-II [142] experiments. This shows that monojet limits are complementary to the results from the direct detection experiments at low dark matter masses. The 90% CL upper limits on the spin-dependent cross section obtained for the axial-vector mediator are compared to the PICO-2L [143], PICO-60 [144], IceCube [145], and Super Kamiokande experiments [146]. In the case of the pseudoscalar mediator, the limits are compared to the indirect detection results from the Fermi-LAT experiment [147, 148]. In the considered

- | scenario the dark matter annihilates into b quark pairs in the centre of the galaxy, producing gamma rays.

6

1
2

Search for SIMPs using Trackless Jets

3 The monojet dark matter search detailed in Chapter 5 can be complemented at high interaction cross
4 sections by a different search which does not look for dark matter in the form of missing transverse
5 momentum. Indeed, if the dark matter particles have an interaction cross section of the order of the
6 strong interaction, they will interact in the detector, mainly in the calorimeters. The analysis described in
7 this chapter is based on this scenario, and the considered simplified model is specified in Section 2.3.1.
8 In this model, the dark matter particles are produced in pairs through a new strongly interacting mediator,
9 and give rise to a pair of trackless jets as signature. Since the produced strongly interacting massive
10 particles (SIMPs) are neutral, the resulting jets can be distinguished from QCD jets using the jet charged
11 hadron energy fraction (CHF). The signal region where the SIMPs are being looked for is therefore
12 defined by requiring the two leading jets to have a low CHF. In the control region, which is used to
13 predict and validate the expected background, one or both jets are required to have a large CHF.

14 Firstly, the applied jet and photon reconstruction and identification are described, as well as the spe-
15 cific treatment applied for the primary vertex selection. The triggers that were designed specifically for
16 this search, exploiting the CHF, are outlined in Section 6.2. However, these triggers were found to be
17 problematic and eventually a generic single jet trigger was used instead. Next, the event selection is de-
18 tailed in Section 6.3 for both the signal and control regions. The strategy for the background estimation
19 and the systematic uncertainties are discussed in Sections 6.4 and 6.5, respectively. Finally, in Sec-
20 tions 6.6 and 6.7, the results are shown and interpreted in terms of the SIMP simplified model described
21 in Section 2.3.

22 **6.1 Physics object reconstruction**

23 In this analysis, jets with a very small charged hadron energy fraction (CHF) are being searched for. Since
24 these are rather peculiar jets containing no or very few tracks, a good primary vertex selection and photon
25 identification play an important role in suppressing the main physics and reconstruction backgrounds.

26 **6.1.1 Jets**

27 For the jet reconstruction, the standard method described in Section 4.3.7 is used. Although the jets in the
28 signal samples are expected to be neutral, it is beneficial to use PF jets because they directly provide an
29 unambiguous association of tracks to jets. The standard jet energy corrections are applied as well, while
30 the standard jet identification criteria are not used, since several of the quality criteria would actually
31 remove the neutral SIMP jets.

6.1.2 Photons

Since photons might be reconstructed as neutral jets, photon + jets events are an important background for the control as well as the signal region. The photons therefore need to be identified and rejected, which is done using the standard photon loose identification described in Section 4.3.3. Further photon rejection is achieved by analysis-specific selections on photon conversions and on the jet neutral electromagnetic energy fraction (NEMF), as described in Section 6.3.

6.1.3 Primary vertex

The standard primary vertex reconstruction described in Section 4.3.1 sometimes provides a wrong primary vertex, which arises from a pileup interaction. The choice of a wrong vertex is not a problem in the case of signal events, which will pass in particular the CHF cuts in the event selection detailed in Section 6.3 just as easily. However, a wrongly chosen vertex in a QCD background event leads to the jets having an artificially very low CHF, both in simulation and data, as the standard charged hadron subtraction (CHS) procedure will remove the tracks from the vertex of the true hard interaction. This makes such events appear signal-like. For the lowest jet charged hadron energy fractions considered in this analysis, this background of events with a misidentified primary vertex becomes dominant with respect to the background from QCD events with a very rare jet fragmentation into predominantly neutral hadrons and photons. In Figure 6.1 an event display is shown that demonstrates such a wrong choice of vertex.

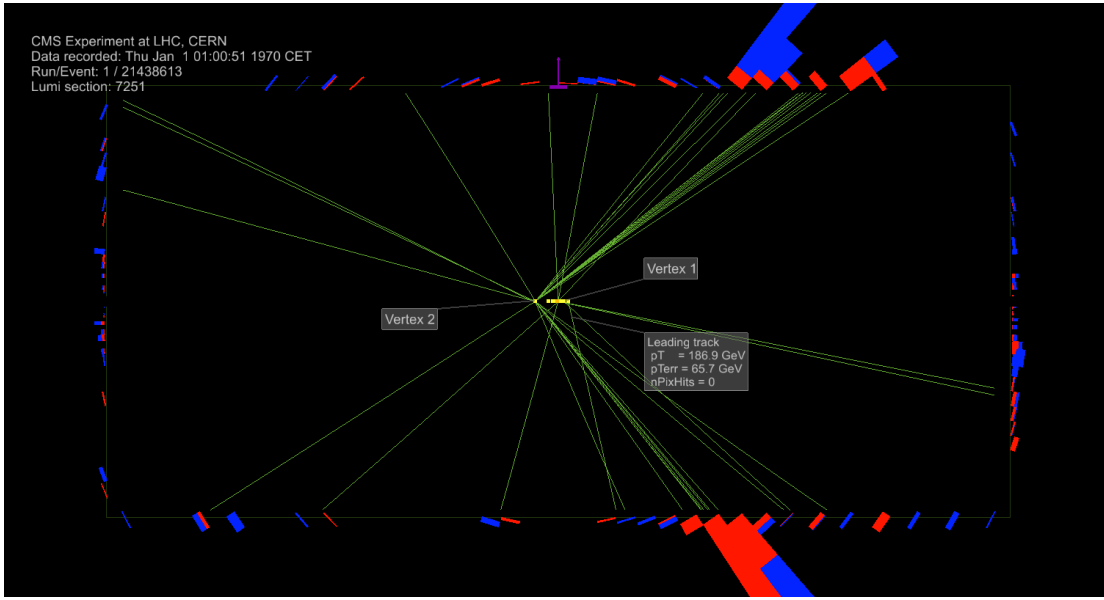


Figure 6.1: Event display showing an example of a wrong primary vertex selection in a MC simulated QCD event. Although "Vertex 2" is the real vertex of the hard collision, "Vertex 1" is selected because of the presence of a single high- p_T track with poor momentum resolution and no pixel hits attached. As a result, the two visible high- p_T jets (above 200 GeV), clearly with many tracks attached, are reconstructed with only 3% and 4% of charged energy fraction.

Investigating this problem, many events with a wrong vertex assignment were observed to have the highest- p_T track being of poor quality, with a high momentum with large uncertainty, and no pixel hits. This alone, though, does not provide a sufficient handle to suppress this background, and a plain cut on number of pixel hits was verified to remove a lot of signal events as well. Studying the simulated Quantum Chromodynamics (QCD) multijet events with a very low CHF coming from primary vertex misidentification by analysing event displays also showed that the true vertex is reconstructed as the second vertex in the list for the far majority of the cases. A second jet reconstruction was therefore produced, based on selecting the second entry in the list of primary vertices to be the event's collision vertex, and rerunning the CHS as well. If this second vertex was the correct one, the jets will now have

a large CHF in most of the cases, while the first event reconstruction yields low-CHF jets. In the event selection discussed in Section 6.3, it is then sufficient to ask both event reconstructions to pass the cut of low jet CHF, effectively suppressing this background induced from wrong primary vertex selection.

6.2 Trigger selection

Several triggers have been designed specifically for this analysis, as shown in Table 6.1. Four triggers were available to select signal events, denoted as “signal” in the table and providing a trade-off between a high CHF and a low jet p_T . The CHF cut is always applied on both jets. Two additional triggers, indicated with the “control” type, were used to determine the trigger efficiencies. These triggers were prescaled, meaning that only a fraction of the events are kept due to the otherwise very high rate of the trigger.

Trigger name	Type	Int. Lumi.
HLT_DiCentralPFJet170_CFMMax0p1_v*	Signal	33.1 fb^{-1}
HLT_DiCentralPFJet220_CFMMax0p3_v* ¹	Signal	5.91 fb^{-1}
HLT_DiCentralPFJet330_CFMMax0p5_v*	Signal	33.1 fb^{-1}
HLT_DiCentralPFJet430_v*	Signal	33.1 fb^{-1}
HLT_DiCentralPFJet170_v*	Control	0.101 fb^{-1}
HLT_SingleCentralPFJet170_CFMMax0p1_v*	Control	0.375 fb^{-1}

Table 6.1: Summary of the triggers designed for this analysis.

These triggers were designed by using QCD samples to test their performance before using them in data taking, since the signal samples do not simulate the trigger behaviour. The trigger efficiency of HLT_DiCentralPFJet330_CFMMax0p5 as a function of p_T and CHF is shown in Figure 6.2, using data and simulated QCD events. The signal efficiency measurement was first tried by taking a photon + jet sample, as photons could also mimic neutral jets. The photon was matched to the leading jet and the efficiency was measured at low CHF. However, the photon is in many cases reconstructed as an electron by the PF algorithm. Thus, the jet is reconstructed with a large electromagnetic energy fraction (EMF) and it does not mimic the SIMP signal.

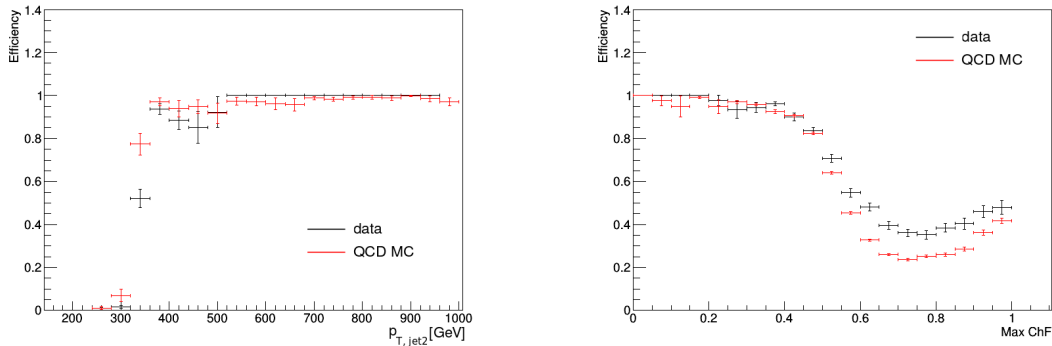


Figure 6.2: The HLT_DiCentralPFJet330_CFMMax0p5 trigger efficiency as a function of p_T (left) and CHF (right). Comparison between data (black) and QCD simulation (red).

Instead, one of the neutron signal samples described in Section 4.4 was used, generated with a SIMP mass of 700 GeV. The obtained trigger efficiency as a function of p_T and CHF is shown in Figure 6.3 for HLT_DiCentralPFJet330_CFMMax0p5, comparing the data and the signal-like events. This shows that the trigger reaches a plateau at only 60% signal efficiency. The origin of the inefficiency was found to come from a requirement asking at least one charged particle in the jets. This explains why the trigger efficiencies turn on at the expected values when using data or simulated QCD events, while it is largely inefficient in signal-like simulation which generates neutral jets.

¹Due to the unexpected high rate, this trigger was disabled after some time.

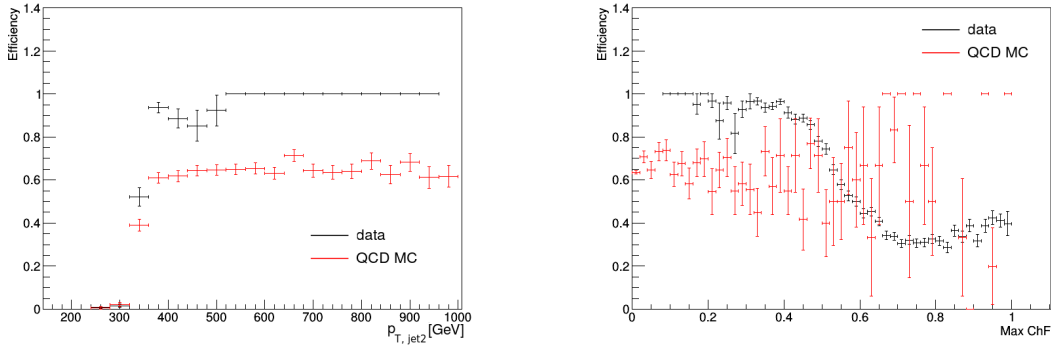


Figure 6.3: The HLT_DiCentral1PFJet330_CFMMax0p5 trigger efficiency as a function of p_T (left) and CHF (right). Comparison between data (black) and signal-like MC (red).

Consequently, the single jet trigger HLT_PFJet450 has been used for the analysis. It was selected because it has the lowest threshold among the unprescaled² single jet triggers. The trigger efficiency for the data was measured using the single muon events, and is defined as

$$\epsilon = \frac{\text{Obs}(\text{HLT_PFJet450 and HLT_IsoMu24})}{\text{Obs}(\text{HLT_IsoMu24})}, \quad (6.1)$$

where Obs in this case is the p_T spectrum of the leading jet for events that fired the single muon (and single jet) trigger. The jets are required to have a muon energy fraction smaller than 0.3 in order to avoid jets with large difference in the online and offline p_T . This difference can arise when the offline PF jet contains a high- p_T muon. Since the online jet is reconstructed using only information from the calorimeters, this can significantly change the total p_T of the jet between online and the offline PF jet. The trigger efficiency was also measured in the simulated QCD and neutron signal samples. In this case the denominator is the p_T spectrum of leading jet without any trigger selection, while the numerator is the p_T spectrum of the events firing the single jet trigger. Figure 6.4 shows the turn-on curves for data, QCD events, and the signal-like events. The trigger efficiency was found to be 98% for jets with $p_T > 550$ GeV.

6.3 Event selection

The event selection aims to select back-to-back dijet events with a low CHF. As a baseline selection, the two highest- p_T jets are required to have $p_T > 550$ GeV, in order to ensure the jets to be above the turn-on of the trigger. Furthermore, they are required to have $|\eta| < 2.0$, placing them fully within the tracking volume, thus suppressing backgrounds from jets that have a low CHF due to tracks falling out of tracker acceptance. Since the SIMPs do not undergo parton showering, while QCD partons undergo final state radiation, events with SIMPs have a lower number of jets than QCD multijet events, as can be seen from the top right plot in Figure 6.5. Events containing additional jets with $p_T > 30$ GeV in the full η acceptance of the CMS calorimeters on top of the two leading jets are therefore vetoed.

A photon veto is also applied to suppress photon + jets events. This is done by rejecting events with a photon within $\Delta R < 0.1$ of the leading or subleading jet, using the loose working point of the cut-based photon identification to identify photons, as described in Section 4.3.3. In some cases, however, jets have a large photon energy fraction, but the photon in the jet does not pass the loose identification requirements, for instance when there is a photon conversion in the tracker. In order to reject photon + jets events more efficiently, an additional cut is applied, as described in Section 4.3.3.

In order to avoid any problems related to the striking discrepancy between data and simulation observed for events with only one reconstructed vertex in the top left plot of Figure 6.5, at least two reconstructed vertices are required. Additionally, the azimuthal separation of the two selected jets is required

²Triggers with a lower p_T threshold exist, but these are prescaled. Prescaled triggers are typically not used to perform an analysis, as only a small fraction of the events that pass the trigger are kept, leading to large statistical uncertainties.

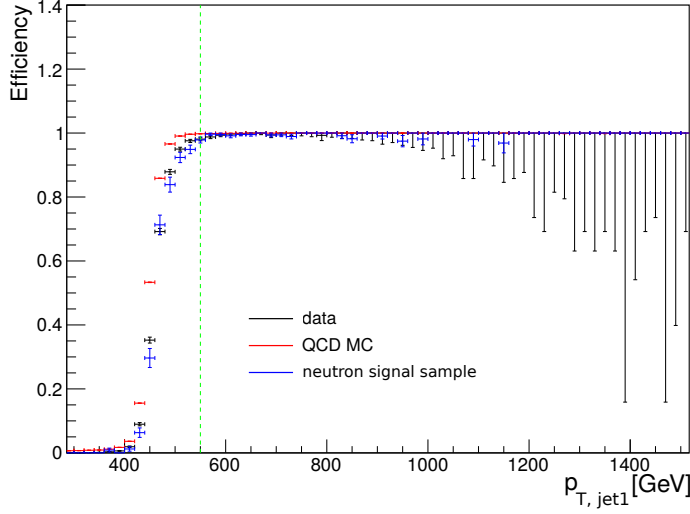


Figure 6.4: The HLT_PFTjet450 trigger efficiency turn-on as a function of the offline leading jet p_T , for data, QCD events, and the signal-like events. The p_T cut used in the event selection is shown with a green dashed line.

1 to be $\Delta\phi > 2$. Finally, noise filters are applied in order to reject beam halo or instrumental background,
2 such as noise in the calorimeters.

3 Table 6.2 shows the number of events remaining in data, for simulated QCD events, and for 2 signal
4 samples, after consecutively applying the described selection cuts. This shows that the background is
5 already reduced by a factor 5, mainly by the cut on the number of jets, while a high efficiency is main-
6 tained for the signal. In Figure 6.6, data, QCD multijet simulation, and signal are compared after these
7 selections, for the p_T , η and CHF of the two leading jets. Figure 6.5 shows the distribution of the number
8 of vertices, the number of jets, $\Delta\phi(\text{jet1}, \text{jet2})$, and H_T , which is defined as the sum of the transverse
9 momenta of the two jets. In some cases, all the selection cuts except the cut on the variable being shown
10 are applied. The bump and long tail that can be seen in the data for the $\Delta\phi(\text{jet1}, \text{jet2})$ distribution contain
11 events coming from processes with a heavy vector boson, such as Z + jets or W + jets, or $t\bar{t}$ events. The
12 simulation instead shows a steeply falling spectrum since only QCD dijet events are shown. Contributions
13 from Z + jets or W + jets, and $t\bar{t}$ events were verified to be negligible in the signal region using simulated
14 samples.

selection cut	yield			
	data	QCD MC	SIMP ($m_\chi = 1$ GeV)	SIMP ($m_\chi = 1000$ GeV)
$p_T^{j1,j2} > 550$ GeV	2540420	3152550	773	5.7
$ \eta_{j1,j2} < 2.0$	2441240	2980320	748	5.6
# jets = 2	534053	587670	636	4.9
photon veto	531366	586674	636	4.9
# vertices ≥ 2	531244	586641	636	4.9
$\Delta\phi(j1, j2) > 2$	531207	586641	636	4.9
noise filters	528614	582184	634	4.9

Table 6.2: Number of events remaining after the listed selection cuts in data, QCD events, and for 2 signal samples.

15 As will be detailed in Section 6.4, the background is predicted from a data control region where at least
16 one of the leading jets has a high CHF, above 0.25. No further selection on the second reconstruction with

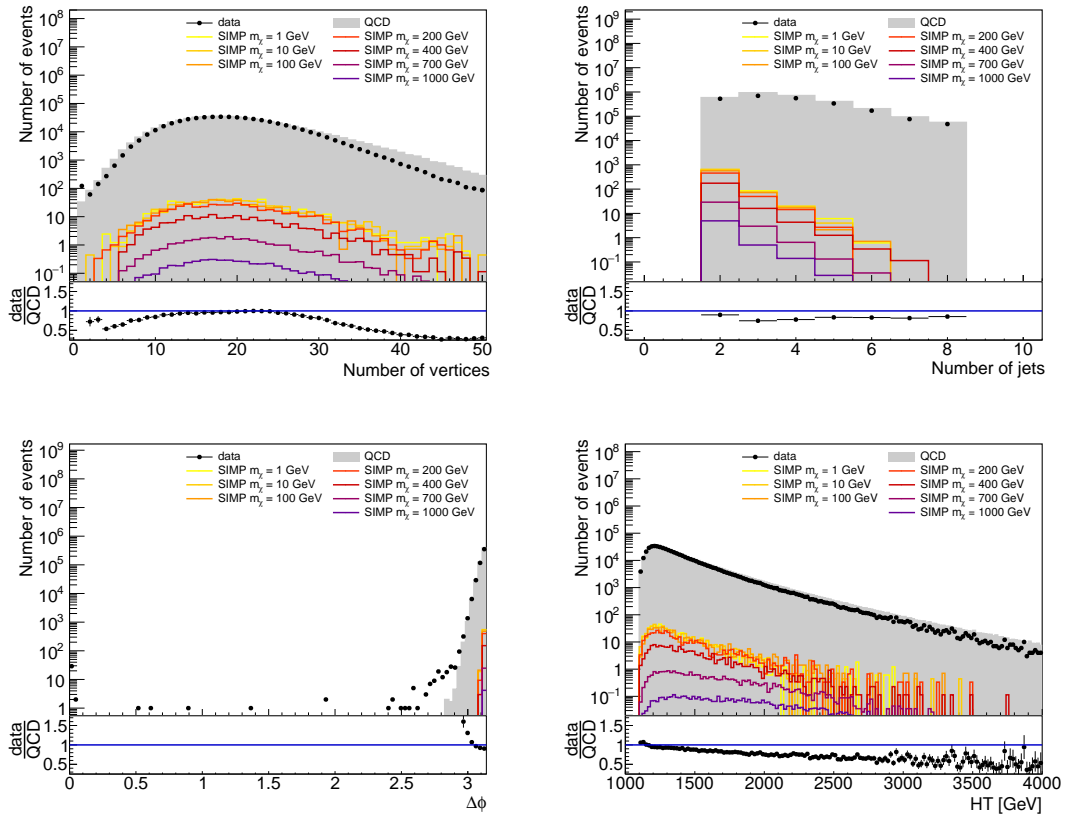


Figure 6.5: Number of vertices, number of jets, $\Delta\phi(\text{jet1}, \text{jet2})$, and H_T distributions, with selection cuts applied. The requirement on the number of vertices is not applied for the corresponding plot, the cut on the number of jets is not applied for the number of jets distribution, and the $\Delta\phi$ cut is similarly not applied for the corresponding distribution.

- 1 respect to the second primary vertex is applied for the control region, since the presence of at least one
- 2 jet with a large CHF avoids the problem of the wrong selection of primary vertex detailed in Section 6.1.
- 3 In the case of the signal region selection, both jets are required to have $\text{CHF} < x$, where x is the
- 4 signal cut being considered. In this case, the cut is applied for both reconstructions starting from the first
- 5 and second primary vertex.

6.4 Background estimation

- 7 The main background for this analysis are QCD multijets. This background is estimated from data, as
- 8 the simulation does not describe the data well, especially at low CHF. The signal events can then be
- 9 distinguished from this background using the jet CHF. A second background comes from photon + jets
- 10 events. However, this background is efficiently removed by applying a photon veto.

11 6.4.1 Photon + jets

- 12 The photon + jets background was studied using a high- H_T MC sample generated at LO with MAD-
- 13 GRAPH5-aMC@NLO, hadronized with PYTHIA 8, and simulated and reconstructed using the standard
- 14 procedure described in Chapter 4. The used sample corresponds to about 27 fb^{-1} , which is larger than
- 15 the data sample used for this analysis and is therefore sufficient to evaluate its contribution in the signal
- 16 region. This background is verified to be negligible after applying the signal region event selection, and
- 17 well within any other systematic uncertainty on the background prediction. The photon veto works well,

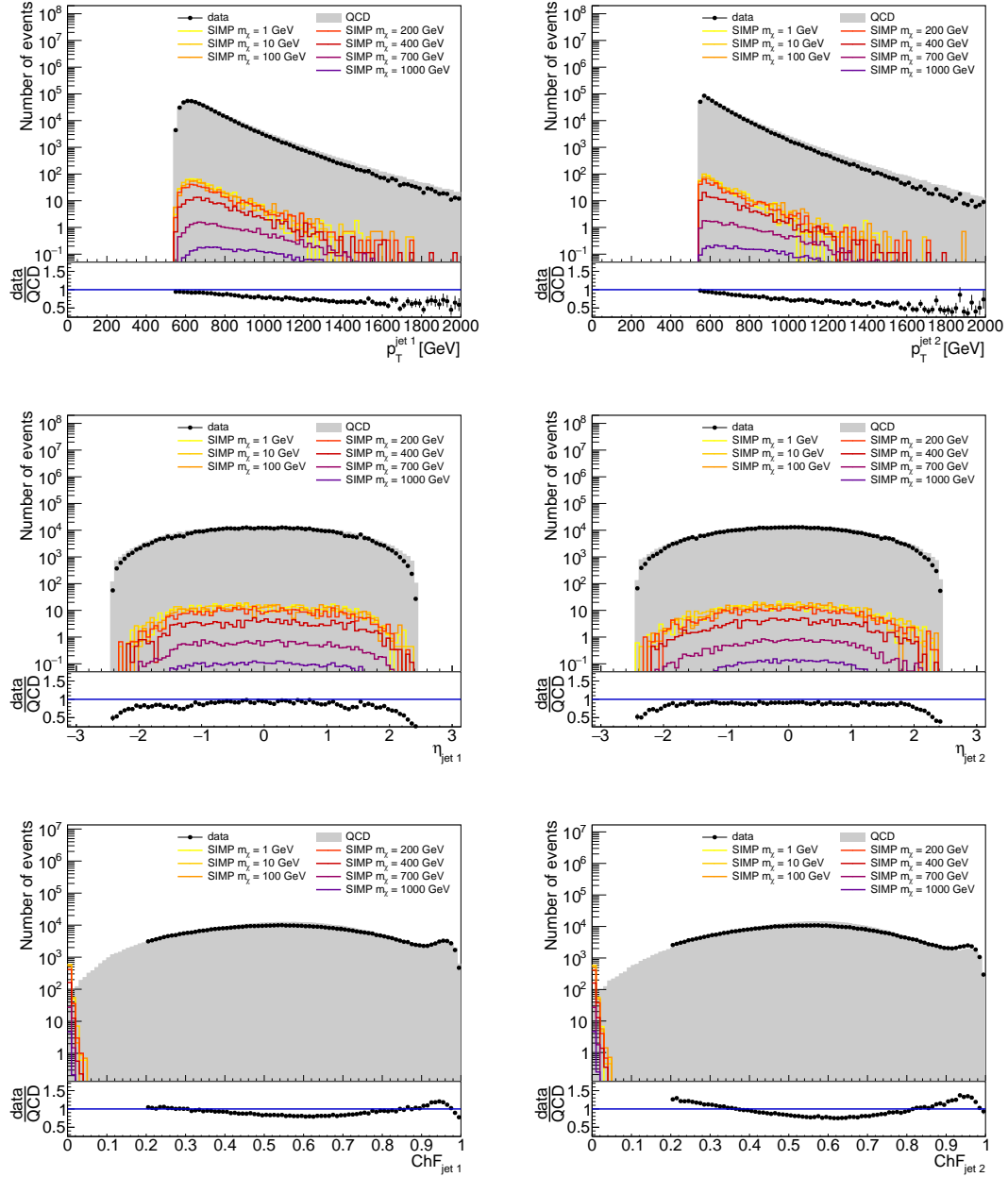


Figure 6.6: p_T , η and CHF of the leading (left) and subleading (right) jet. The selection cuts are applied, except for the cut on η in the corresponding plot.

especially the cut on the jet neutral electromagnetic fraction, and no events from the used simulated photon + jets sample remain after applying a cut of $\text{CHF} < 0.1$. Additionally, in part of the events remaining just above that cut the photon is not identified because it is very close to a jet. These events are therefore already contained in the overlapping QCD multijets sample.

6.4.2 QCD multijets

The QCD multijet background is estimated from data, since the simulation does not describe the data well, especially at low CHF, as can be seen from Figure 6.7 which compares the CHF distribution in the control region to the QCD MC. In this plot the subleading jet is required to have a large CHF, in order to stay in the control region.

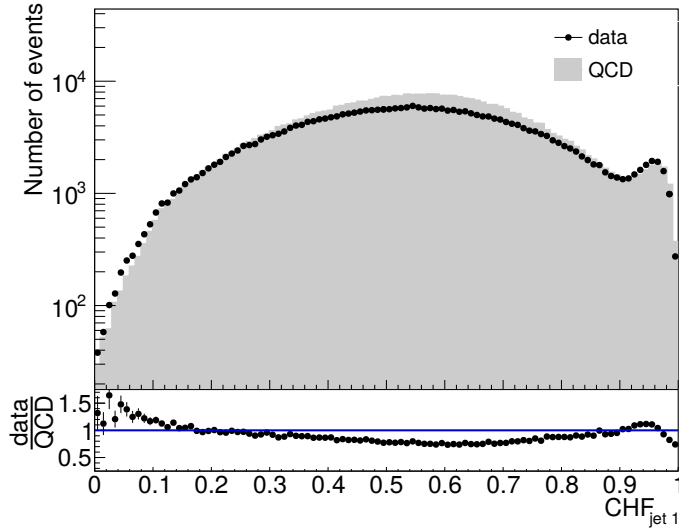


Figure 6.7: Data-MC comparison of the charged energy fraction of the leading jet, tagging events with subleading jet $\text{CHF} > 0.5$.

As a first step, the efficiency of the CHF cut is measured in the control region, by tagging one jet with high CHF and applying the CHF cut on the other jet. The efficiency is then given by the ratio of the number of events passing the cut divided by the total number of events selected in the control region. The measurement is performed in bins of jet p_T and η . The number of QCD events in the signal region is then predicted by using any QCD dijet event passing the selection cuts listed in Table 6.2 and applying the appropriate p_T and η dependent CHF cut efficiencies on the two leading jets. Figure 6.8 shows the measured 1D efficiency as a function of the CHF cut for various bins in p_T^{jet} and η_{jet} , as measured in the QCD MC. There is a strong dependence on the jet p_T , and a less pronounced dependence on the jet η at low CHF. The efficiencies are the highest for the $1.0 < |\eta| < 1.25$ bin, which can be attributed to this being the barrel-endcap transition region where most of the tracker material budget is located. The dependence on the jet p_T arises from the reconstruction. As can be seen from the left plot in Figure 6.9, at generator level the CHF is independent of the jet p_T , as one would expect. After reconstruction, as demonstrated in the right plot of Figure 6.9, a p_T dependence arises due to the known degradation of tracking efficiency in dense jet environments, which becomes more of an issue for very high p_T and thus collimated jets.

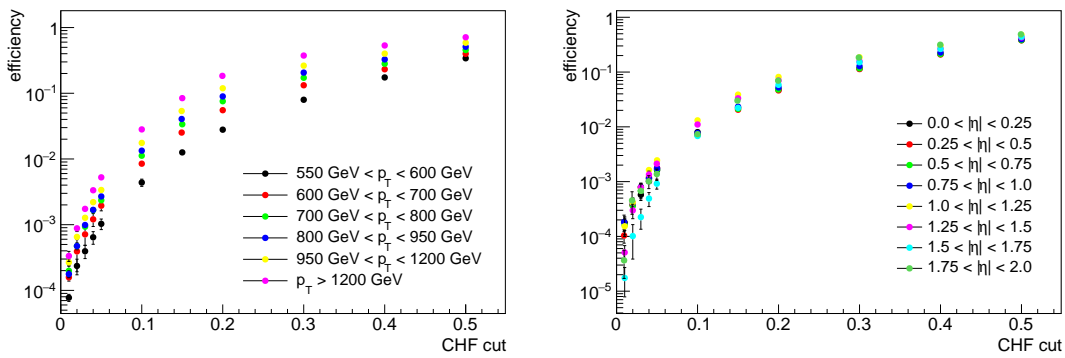


Figure 6.8: The efficiency of several CHF cuts in QCD MC, binned in p_T (left) and η (right).

A closure test is performed to validate this background prediction method, by comparing the MC truth and the 1- and 2-leg predictions in MC. The MC truth shows the yield after applying the CHF cuts

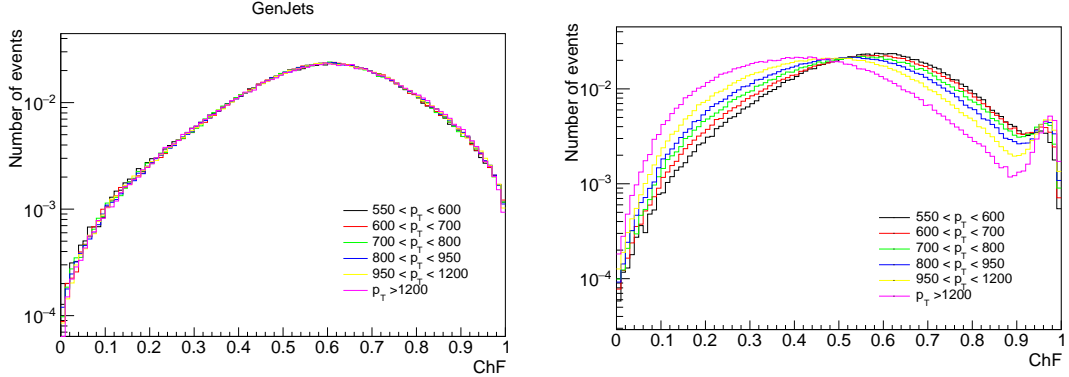


Figure 6.9: The CHF per bins of jet p_T , for generator level (left) and reconstructed (right) jets.

on both jets. For the 1-leg prediction the CHF cut is applied on one jet and the event is then weighted by applying the measured p_T - and η -dependent efficiency for the other jet. For the 2-leg prediction, the efficiencies are applied for both jets, and no CHF cut is applied directly.

As a first check the closure test was also performed at the generator level, using the GenJets, which are reconstructed from the generator level particles. This comparison is done in exclusive bins in $(\text{CHF}_{\text{jet}1}, \text{CHF}_{\text{jet}2})$, as illustrated in Figure 6.10. From Figure 6.11 one can see that there is a good agreement between MC truth, 1-, and 2-leg predictions. This shows that there are no relevant physics correlations between the 2 jets, an essential prerequisite for this background prediction to work well. The p_T and η binning seems adequate as well.

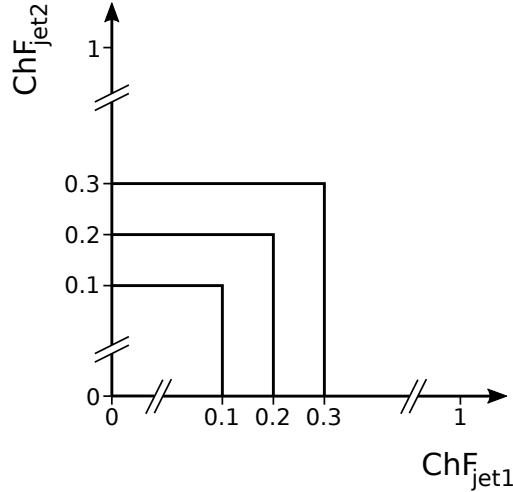


Figure 6.10: Illustration of the exclusive bins in the leading and subleading jet CHF, used for the closure test and the data vs. prediction comparisons.

Next, the closure test is performed with reconstructed jets, as shown in the left plot of Figure 6.12, using the exclusive binning. For the MC truth, the CHF cut is applied on the 2 leading jets of the standard jet collection, as well as the 2 leading jets of the jet collection created when using the second vertex as primary vertex. This extra cut is a part of the signal region event selection described earlier, designed to remove events where the wrong primary vertex was chosen and the charged fraction of the jets is removed by CHS. However, there is still a small discrepancy between the MC truth and the prediction at the tightest CHF cuts. This is mainly due to a very small number of events where the wrong vertex was chosen, but where the correct one is not the second one.

The closure test on MC is also performed in inclusive bins, as used in the signal region event selection, by applying the same cut on the CHF of both jets. This is shown in the right plot of Figure 6.12, with the applied CHF cut on the x-axis. For the MC truth, the statistical uncertainty is determined per HT-binned

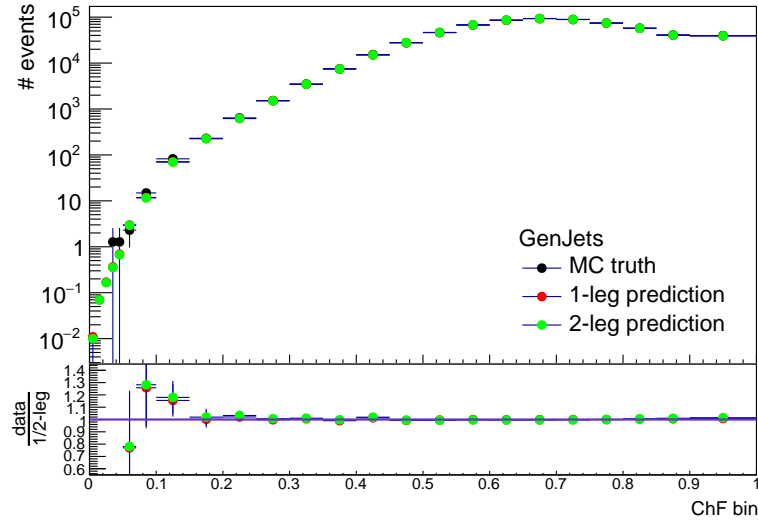


Figure 6.11: Closure test using GenJets.

1 QCD sample, using asymmetric vertical bars with correct coverage for event counts with Poisson variates
 2 when less than 10 events remain, and the square root of the remaining number of events otherwise. In
 3 this way, the statistical uncertainty correctly reflects the contribution of HT bins with few or no events
 4 left. The total statistical uncertainty is then calculated by multiplying the uncertainty per HT bin by the
 5 corresponding weight for this HT bin, and adding them quadratically. The systematic uncertainty on the
 6 background prediction is then defined as the difference between the MC truth and the prediction, unless
 7 it is smaller than the statistical uncertainty on the MC truth. In that case, the uncertainty on the MC truth
 8 is taken as systematic uncertainty.

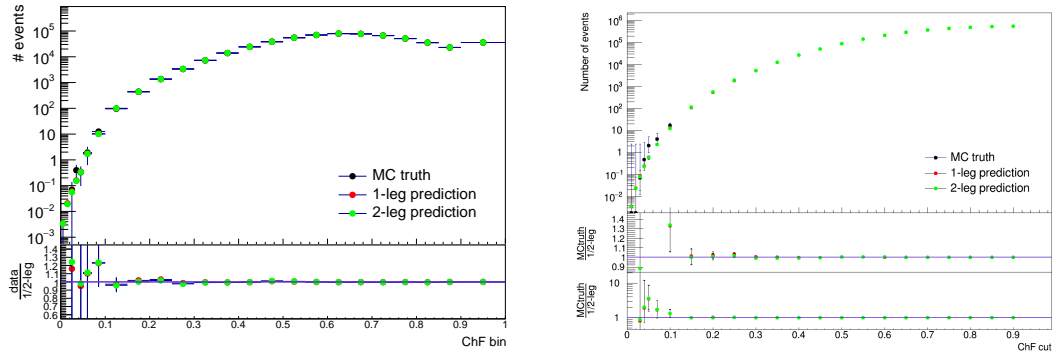


Figure 6.12: Closure test in MC using an exclusive (left) or inclusive (right) binning in CHF.

9 The QCD background prediction in data is shown in Figure 6.13 as a function of the exclusive CHF
 10 bins, using the `HLT_PFMET450` single jet trigger. The data is blinded in the signal region below CHF
 11 = 0.05. A distinction is made between the run periods B to F (left) and G to H (right). There is a clear
 12 deviation below a CHF of 0.4 for run periods B to F, while the agreement is very good down to CHF =
 13 0.05 for run periods G and H. The main difference between these 2 datasets is the issue with the Tracker
 14 APV pre-amplifier saturation, described in Section 3.2.6.1, which was solved from run period G onwards.

15 To first order, the measured CHF cut efficiencies should absorb the effects of tracking inefficiencies
 16 caused by the APV pre-amplifier saturation problem. However, this effect is also reflected in the dis-
 17 tribution of the number of vertices. As is shown in Figure 6.14, a subtle effect causes the data and the
 18 prediction from data to disagree in the distribution of the number of vertices for run periods B to F, while
 19 a good agreement is obtained for run periods G to H. As there are not enough data to derive the CHF effi-

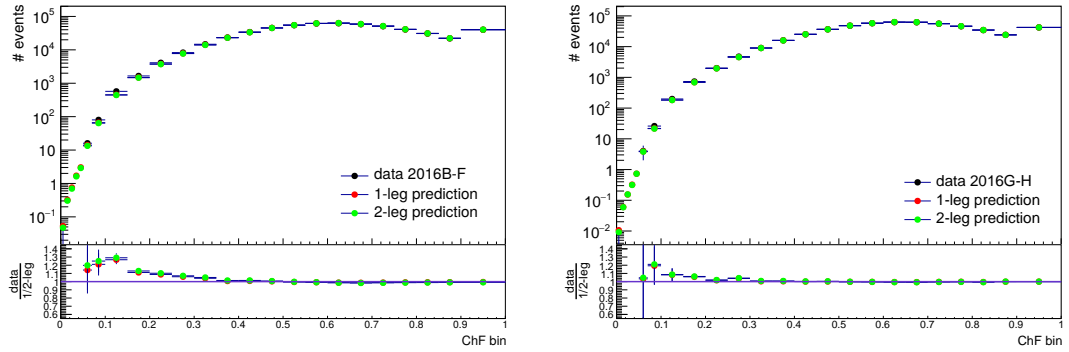


Figure 6.13: The 1- and 2-leg predictions from data, as well as the data (above CHF = 0.2) as a function of the exclusive CHF bins, for run periods B-F (left) and G-H (right).

encies reliably in bins of number of vertices as well as p_T and η , a recovery of the data in this way is not possible. A reweighting was also performed, using a fit to the ratio of data divided by the 2-leg prediction per CHF bin. Figure 6.15 shows the data versus data prediction comparison in run period E, applying the reweighting based on the number of vertices in the event, per CHF bin, and a clear improvement can be observed for the 2-leg prediction. In contrast, the 1-leg prediction has not been reweighted and still shows the original disagreement. This reweighting can however not be used in the signal region, where very few events remain. As a result, the analysis is performed with run periods G and H only, corresponding to an integrated luminosity of 16.1 fb^{-1} .

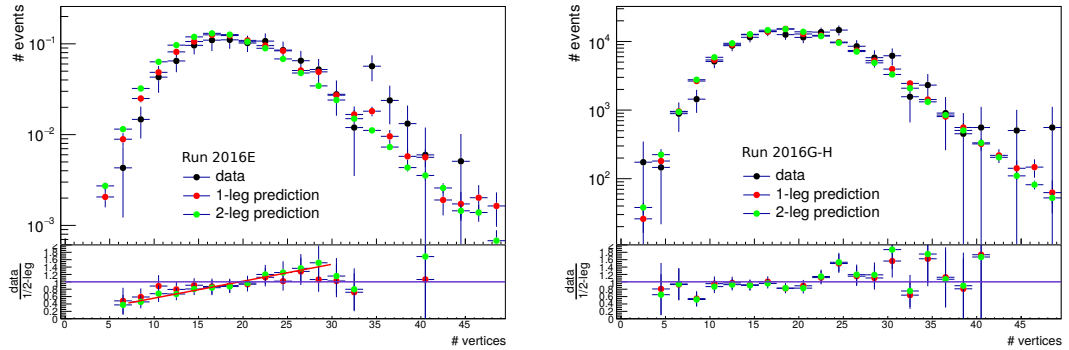


Figure 6.14: The distribution of the number of vertices for data, 1-leg, and 2-leg prediction using data from run period E (left) and run periods G-H (right).

6.5 Systematic uncertainties

For the signal prediction, systematic uncertainties are included for the luminosity, the jet energy corrections, and the trigger inefficiency at 550 GeV due to the turn-on. The systematic uncertainty for the luminosity amounts to 2.5%. The systematic uncertainty coming from the jet energy corrections is computed by varying the jet energy by the correction and recalculating the yield after applying the selection cuts and the CHF cut. Depending on the SIMP mass and the CHF cut, this uncertainty varies between 0.4% and 3.9%. A systematic uncertainty is also included to take into account the trigger inefficiency at 550 GeV due to the turn-on. This is done by taking a 100% uncertainty on the efficiency, which gives a 2% systematic uncertainty for the signal. This method does not take into account the fact that the turn-on was determined for one jet only and the inefficiency is strongly reduced when two jets with a similar p_T are present in the event. However, some signal events have one of the two jets with $\text{EMF} = 0$. In this case the jet which does not contain electromagnetic energy would not fire the single jet trigger and these events

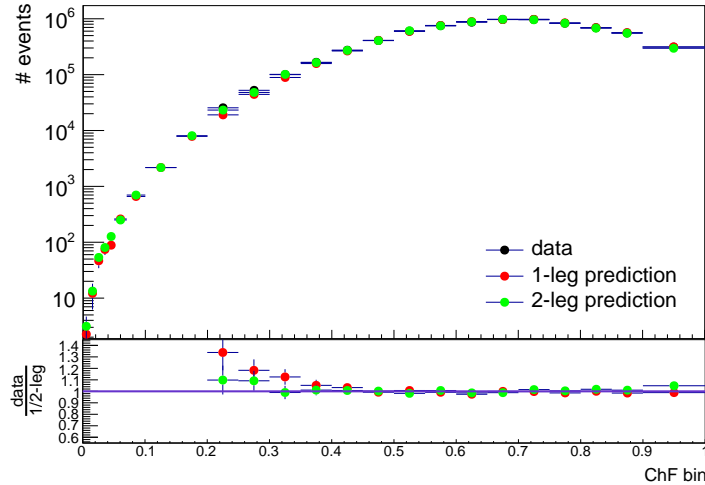


Figure 6.15: The 1- and 2-leg predictions from data, as well as the data (above CHF = 0.2) as a function of the exclusive CHF bins for run period E, reweighting the 2-leg prediction to data based on the number of vertices in the event, per CHF bin.

become single jet events from the trigger point of view. The 2% uncertainty is therefore conservative as it represents the worst case scenario. The photon and conversion veto was found to be 100% efficient on the signal, and as a result this systematic uncertainty is negligible. The effect of pileup was considered to be negligible as well, as the distribution of the number of vertices is very similar for the data and SIMP samples. As an example the data is compared to the SIMP sample with $m_\chi = 1000$ GeV in Figure 6.16, which shows that there is a good agreement in the bulk of the distribution with some deviations for a high number of primary vertices only.

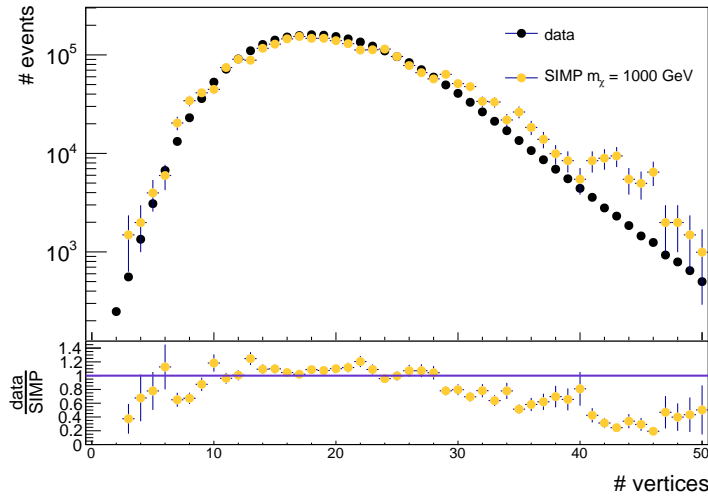


Figure 6.16: The distribution of the number of vertices in data compared to the SIMP signal with $m_\chi = 1000$ GeV.

As mentioned in Section 6.4, the main systematic uncertainty on the background prediction is obtained from the closure test in MC, by taking the difference between the MC truth and the prediction, unless it is smaller than the statistical uncertainty on the MC truth, in which case the uncertainty on the MC truth is taken as systematic uncertainty. This uncertainty varies between 4% and 3416%, depending on the CHF cut. As for the signal, the trigger inefficiency due to the turn-on at 550 GeV is also taken into account, yielding an additional 2% systematic uncertainty.

6.6 Results

Table 6.3 shows the number of predicted and observed events, per considered CHF cut. The prediction is done using the 1-leg data prediction, as this provides slightly smaller uncertainties due to the larger number of events that are selected to perform the prediction. The statistical uncertainty, as well as the systematic uncertainty from the closure test described in Section 6.5, are given.

A cut of $\text{CHF} < 0.05$ is chosen, to reject most of the QCD background. The background is then reduced to the level of about one event, and a large uncertainty does not have big consequences. Moreover, the uncertainty from the closure test is reduced when taking into account the smaller statistical uncertainty on the number of background events during the limit calculation. In addition, the expected sensitivity does not improve significantly at tighter CHF cuts, and the closure tests becomes statistically limited. The dominating uncertainty then comes from the closure test, and amounts to 250% in this case.

CHF cut	data prediction	QCD MC prediction	observed	SIMP signal [m_χ]	
				1 GeV	1000 GeV
0.2	902 ± 5 (stat.) ± 38 (syst.)	546.5 ± 0.6	969	634	4.9
0.15	210 ± 2 (stat.) ± 18 (syst.)	111.1 ± 0.4	229	634	4.9
0.1	26.9 ± 0.3 (stat.) ± 8.9 (syst.)	12.6 ± 0.2	30	634	4.9
0.07	5.1 ± 0.1 (stat.) ± 4.4 (syst.)	2.3 ± 0.2	4	634	4.9
0.05	1.28 ± 0.03 (stat.) ± 3.24 (syst.)	0.6 ± 0.1	0	634	4.9
0.04	0.55 ± 0.02 (stat.) ± 2.81 (syst.)	0.24 ± 0.09	0	633	4.9
0.03	0.22 ± 0.01 (stat.) ± 7.68 (syst.)	0.08 ± 0.07	0	632	4.9

Table 6.3: Number of predicted (using the 1-leg prediction from data) and observed events for the considered cuts. The expected number of signal events is also given for the $m_\chi = 1$ GeV and $m_\chi = 1000$ GeV scenarios.

Model-independent limits are derived for a $\text{CHF} < 0.05$ cut, using the CL_S criterion [134, 135] with the LHC style test statistic in which the systematic uncertainties are modelled as nuisance parameters. This was done using the RooStat-based Combine tool, taking into account the systematic uncertainties detailed in Section 6.5, as well as the statistical uncertainties on signal and background predictions. All included systematic uncertainties are profiled with a lognormal prior, except for the uncertainty coming from the closure test, which is profiled with a gamma function since it arises from the limited number of remaining events. The resulting expected fiducial cross section is $\sigma_{\text{fid}}^{95\%} = \sigma \times A \times \epsilon = 0.17$ fb. With zero observed events, the observed model-independent lower limit is found to be $\sigma_{\text{fid,obs}}^{95\%} = 0.18$ fb.

6.7 SIMP model interpretation

Limits are also derived on the production cross section for the SIMP simplified model, using the same method as described for the model-independent limits. The expected limits on the production cross section are shown for SIMP masses between 1 and 1000 GeV in Figure 6.17, using a cut of $\text{CHF} < 0.05$. In this case, the search is sensitive to all the generated SIMP mass points, up to 1000 GeV.

Figure 6.18 shows the expected and observed limits when including the observation of zero events in the signal region. The expected and observed limits, and the theoretical cross section are given with respect to the generator level cuts applied in the signal sample generation, $p_T^\chi > 200$ GeV and $|\eta_\chi| < 2.5$. The shown theoretical cross section is also given per SIMP mass point in Table 4.3. In summary, no significant excess above the expected background is observed, and the considered SIMP simplified model is ruled out for SIMP masses up to 1000 GeV.

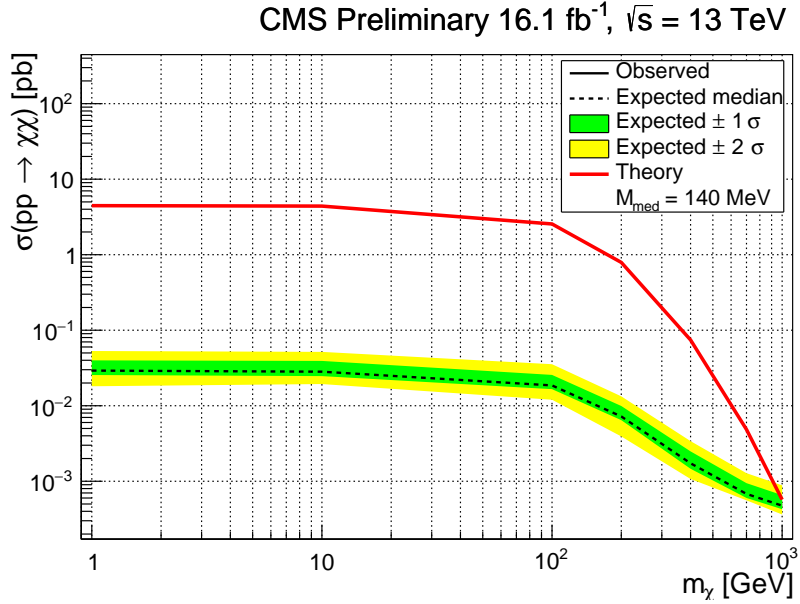


Figure 6.17: The expected limits on the production cross section, obtained without looking in the signal region, for SIMP masses between 1 and 1000 GeV, with 1σ and 2σ bands is shown, as well as the theoretical prediction (red), with respect to the generator level cuts ($p_T^\chi > 200$ GeV and $|\eta_\chi| < 2.5$).

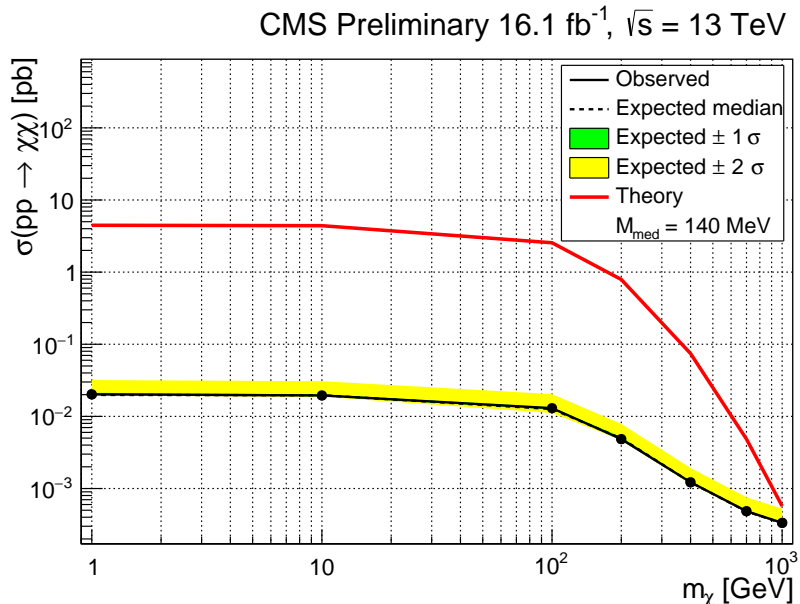


Figure 6.18: The expected and observed limits on the production cross section for SIMP masses between 1 and 1000 GeV, with 1σ and 2σ bands is shown, as well as the theoretical prediction (red), with respect to the generator level cuts ($p_T^\chi > 200$ GeV and $|\eta_\chi| < 2.5$).

7

1

2

Conclusion & Outlook

References

- [1] Michael E Peskin and Daniel V Schroeder. *An introduction to quantum field theory; 1995 ed.* Westview, Boulder, CO, 1995.
- [2] Yorikiyo Nagashima. *Beyond the standard model of elementary particle physics.* Wiley-VCH Verlag, Weinheim, Germany, 2014.
- [3] Georges Aad et al. *Observation of a new particle in the search for the Standard Model Higgs boson with the ATLAS detector at the LHC.* Phys. Lett., B716:1–29, 2012.
- [4] Serguei Chatrchyan et al. *Observation of a new boson at a mass of 125 GeV with the CMS experiment at the LHC.* Phys. Lett., B716:30–61, 2012.
- [5] Sheldon L. Glashow. *The renormalizability of vector meson interactions.* Nucl. Phys., 10:107–117, 1959.
- [6] Steven Weinberg. *A Model of Leptons.* Phys. Rev. Lett., 19:1264–1266, 1967.
- [7] Abdus Salam and John Clive Ward. *Weak and electromagnetic interactions.* Nuovo Cim., 11:568–577, 1959.
- [8] Peter W. Higgs. *Broken Symmetries and the Masses of Gauge Bosons.* Phys. Rev. Lett., 13:508–509, 1964.
- [9] F. Englert and R. Brout. *Broken Symmetry and the Mass of Gauge Vector Mesons.* Phys. Rev. Lett., 13:321–323, 1964.
- [10] G. S. Guralnik, C. R. Hagen, and T. W. B. Kibble. *Global Conservation Laws and Massless Particles.* Phys. Rev. Lett., 13:585–587, 1964.
- [11] David J. Gross and Frank Wilczek. *Ultraviolet Behavior of Nonabelian Gauge Theories.* Phys. Rev. Lett., 30:1343–1346, 1973.
- [12] H. David Politzer. *Reliable Perturbative Results for Strong Interactions?* Phys. Rev. Lett., 30:1346–1349, 1973.
- [13] <http://www.quantumdiaries.org/2014/03/14/the-standard-model-a-beautiful-but-flawed-theory/>
- [14] Q. R. Ahmad et al. *Direct evidence for neutrino flavor transformation from neutral current interactions in the Sudbury Neutrino Observatory.* Phys. Rev. Lett., 89:011301, 2002.
- [15] Y. Fukuda et al. *Evidence for oscillation of atmospheric neutrinos.* Phys. Rev. Lett., 81:1562–1567, 1998.
- [16] Gianfranco Bertone, Dan Hooper, and Joseph Silk. *Particle dark matter: Evidence, candidates and constraints.* Phys. Rept., 405:279–390, 2005.
- [17] F. Zwicky. *Die Rotverschiebung von extragalaktischen Nebeln.* Helv. Phys. Acta, 6:110–127, 1933. [Gen. Rel. Grav.41,207(2009)].
- [18] P. Salucci and A. Borriello. *The intriguing distribution of dark matter in galaxies.* Lect. Notes Phys., 616:66–77, 2003.

- [19] K. G. Begeman, A. H. Broeils, and R. H. Sanders. *Extended rotation curves of spiral galaxies: Dark haloes and modified dynamics*. Mon. Not. Roy. Astron. Soc., 249:523, 1991.
- [20] V. Belokurov, N. W. Evans, P. C. Hewett, A. Moiseev, R. G. McMahon, S. F. Sanchez, and L. J. King. *Two New Large Separation Gravitational Lenses from SDSS*. Mon. Not. Roy. Astron. Soc., 392:104, 2009.
- [21] Arno A. Penzias and Robert Woodrow Wilson. *A Measurement of excess antenna temperature at 4080-Mc/s*. Astrophys. J., 142:419–421, 1965.
- [22] George F. Smoot et al. *Structure in the COBE differential microwave radiometer first year maps*. Astrophys. J., 396:L1–L5, 1992.
- [23] E. Komatsu et al. *Seven-Year Wilkinson Microwave Anisotropy Probe (WMAP) Observations: Cosmological Interpretation*. Astrophys. J. Suppl., 192:18, 2011.
- [24] P. A. R. Ade et al. *Planck 2013 results. XVI. Cosmological parameters*. Astron. Astrophys., 571:A16, 2014.
- [25] <https://briankoberlein.com/2015/06/15/science-in-the-raw/>.
- [26] P. A. R. Ade et al. *Planck 2013 results. I. Overview of products and scientific results*. Astron. Astrophys., 571:A1, 2014.
- [27] M. Azzaro, F. Prada, and C. M. Gutierrez. *Motion properties of satellites around external spiral galaxies*. ASP Conf. Ser., 327:268, 2004.
- [28] Mario Mateo. *Dwarf galaxies of the Local Group*. Ann. Rev. Astron. Astrophys., 36:435–506, 1998.
- [29] John N. Bahcall, Chris Flynn, and Andrew Gould. *Local dark matter from a carefully selected sample*. Astrophys. J., 389:234–250, 1992.
- [30] Lars Bergström. *Nonbaryonic dark matter: Observational evidence and detection methods*. Rept. Prog. Phys., 63:793, 2000.
- [31] V. M. Lobashev. *The search for the neutrino mass by direct method in the tritium beta-decay and perspectives of study it in the project KATRIN*. Nucl. Phys., A719:153–160, 2003.
- [32] V. N. Aseev et al. *An upper limit on electron antineutrino mass from Troitsk experiment*. Phys. Rev., D84:112003, 2011.
- [33] Ch. Kraus et al. *Final results from phase II of the Mainz neutrino mass search in tritium beta decay*. Eur. Phys. J., C40:447–468, 2005.
- [34] M. C. Gonzalez-Garcia and Yosef Nir. *Neutrino masses and mixing: Evidence and implications*. Rev. Mod. Phys., 75:345–402, 2003.
- [35] Scott Dodelson and Lawrence M. Widrow. *Sterile-neutrinos as dark matter*. Phys. Rev. Lett., 72:17–20, 1994.
- [36] Naoki Yoshida, Aaron Sokasian, Lars Hernquist, and Volker Springel. *Early structure formation and reionization in a warm dark matter cosmology*. Astrophys. J., 591:L1–L4, 2003.
- [37] L. J. Rosenberg and K. A. van Bibber. *Searches for invisible axions*. Phys. Rept., 325:1–39, 2000.
- [38] Kimmo Kainulainen and Keith A. Olive. *Astrophysical and cosmological constraints on neutrino masses*. Springer Tracts Mod. Phys., 190:53–74, 2003.
- [39] Nima Arkani-Hamed, Savas Dimopoulos, and G. R. Dvali. *The Hierarchy problem and new dimensions at a millimeter*. Phys. Lett., B429:263–272, 1998.

- 1 [40] Lisa Randall and Raman Sundrum. *A Large mass hierarchy from a small extra dimension*. Phys.
2 Rev. Lett., 83:3370–3373, 1999.
- 3 [41] Edward W. Kolb, Daniel J. H. Chung, and Antonio Riotto. *WIMPzillas!* In Trends in theoretical
4 physics II. Proceedings, 2nd La Plata Meeting, Buenos Aires, Argentina, November 29–December
5 4, 1998, pages 91–105, 1998. [,91(1998)].
- 6 [42] David N. Spergel and Paul J. Steinhardt. *Observational evidence for selfinteracting cold dark
7 matter*. Phys. Rev. Lett., 84:3760–3763, 2000.
- 8 [43] A. De Rujula, S. L. Glashow, and U. Sarid. *CHARGED DARK MATTER*. Nucl. Phys., B333:173–
9 194, 1990.
- 10 [44] Alexander Kusenko and Mikhail E. Shaposhnikov. *Supersymmetric Q balls as dark matter*. Phys.
11 Lett., B418:46–54, 1998.
- 12 [45] John R. Ellis. *Particle candidates for dark matter*. Phys. Scripta, T85:221–230, 2000.
- 13 [46] Lars Bergstrom. *Dark Matter Candidates*. New J. Phys., 11:105006, 2009.
- 14 [47] R. Bernabei et al. *Final model independent result of DAMA/LIBRA-phase1*. Eur. Phys. J.,
15 C73:2648, 2013.
- 16 [48] R. Agnese et al. *Search for Low-Mass Weakly Interacting Massive Particles with SuperCDMS*.
17 Phys. Rev. Lett., 112(24):241302, 2014.
- 18 [49] E. Armengaud et al. *Constraints on low-mass WIMPs from the EDELWEISS-III dark matter search*.
19 JCAP, 1605(05):019, 2016.
- 20 [50] G. Angloher et al. *Results on low mass WIMPs using an upgraded CRESST-II detector*. Eur. Phys.
21 J., C74(12):3184, 2014.
- 22 [51] E. Aprile et al. *XENON100 Dark Matter Results from a Combination of 477 Live Days*. Phys.
23 Rev., D94(12):122001, 2016.
- 24 [52] D. S. Akerib et al. *Results from a search for dark matter in the complete LUX exposure*. Phys. Rev.
25 Lett., 118(2):021303, 2017.
- 26 [53] C. Amole et al. *Dark Matter Search Results from the PICO-60 C₃F₈ Bubble Chamber*. Phys. Rev.
27 Lett., 118(25):251301, 2017.
- 28 [54] Changbo Fu et al. *Spin-Dependent Weakly-Interacting-Massive-ParticleNucleon Cross Section
29 Limits from First Data of PandaX-II Experiment*. Phys. Rev. Lett., 118(7):071301, 2017.
- 30 [55] Teresa Marrodán Undagoitia and Ludwig Rauch. *Dark matter direct-detection experiments*. J.
31 Phys., G43(1):013001, 2016.
- 32 [56] W. B. Atwood et al. *The Large Area Telescope on the Fermi Gamma-ray Space Telescope Mission*.
33 Astrophys. J., 697:1071–1102, 2009.
- 34 [57] F. Aharonian et al. *Observations of the Crab Nebula with H.E.S.S.* Astron. Astrophys., 457:899–
35 915, 2006.
- 36 [58] J. Aleksic et al. *Performance of the MAGIC stereo system obtained with Crab Nebula data*. As-
37 trropart. Phys., 35:435–448, 2012.
- 38 [59] J. Holder et al. *Status of the VERITAS Observatory*. AIP Conf. Proc., 1085:657–660, 2009.
- 39 [60] M. Ageron et al. *ANTARES: the first undersea neutrino telescope*. Nucl. Instrum. Meth., A656:11–
40 38, 2011.

- [61] A. Achterberg et al. *First Year Performance of The IceCube Neutrino Telescope*. *Astropart. Phys.*, 26:155–173, 2006.
- [62] Andrei Kounine. *The Alpha Magnetic Spectrometer on the International Space Station*. *Int. J. Mod. Phys.*, E21(08):1230005, 2012.
- [63] P. Picozza et al. *PAMELA: A Payload for Antimatter Matter Exploration and Light-nuclei Astrophysics*. *Astropart. Phys.*, 27:296–315, 2007.
- [64] Albert M Sirunyan et al. *Search for dark matter produced with an energetic jet or a hadronically decaying W or Z boson at $\sqrt{s} = 13 \text{ TeV}$* . *JHEP*, 07:014, 2017.
- [65] Morad Aaboud et al. *Search for dark matter produced in association with a hadronically decaying vector boson in pp collisions at $\sqrt{s} = 13 \text{ TeV}$ with the ATLAS detector*. *Phys. Lett.*, B763:251–268, 2016.
- [66] Felix Kahlhoefer. *Review of LHC Dark Matter Searches*. *Int. J. Mod. Phys.*, A32(13):1730006, 2017.
- [67] Oliver Buchmueller, Caterina Doglioni, and Lian Tao Wang. *Search for dark matter at colliders*. *Nature Phys.*, 13(3):217–223, 2017.
- [68] The ATLAS collaboration. *Search for long-lived, massive particles in events with displaced vertices and missing transverse momentum in 13 TeV pp collisions with the ATLAS detector*. 2017.
- [69] The ATLAS collaboration. *Search for long-lived charginos based on a disappearing-track signature in pp collisions at $\sqrt{s} = 13 \text{ TeV}$ with the ATLAS detector*. 2017.
- [70] The ATLAS collaboration. *Search for Higgs boson decays to Beyond-the-Standard-Model light bosons in four-lepton events with the ATLAS detector at $\sqrt{s} = 13 \text{ TeV}$* . 2017.
- [71] Albert M Sirunyan et al. *Search for new physics with dijet angular distributions in proton-proton collisions at $\sqrt{s} = 13 \text{ TeV}$* . *JHEP*, 07:013, 2017.
- [72] Albert M Sirunyan et al. *Search for dijet resonances in protonproton collisions at $\sqrt{s} = 13 \text{ TeV}$ and constraints on dark matter and other models*. *Phys. Lett.*, B769:520–542, 2017. [Erratum: *Phys. Lett.* B772,882(2017)].
- [73] Morad Aaboud et al. *Search for new phenomena in dijet events using 37 fb^{-1} of pp collision data collected at $\sqrt{s} = 13 \text{ TeV}$ with the ATLAS detector*. *Phys. Rev.*, D96:052004, 2017.
- [74] Yang Bai and Arvind Rajaraman. *Dark Matter Jets at the LHC*. 2011.
- [75] CMS Collaboration. *Search for heavy stable charged particles with 12.9 fb^{-1} of 2016 data*. 2016.
- [76] Morad Aaboud et al. *Search for metastable heavy charged particles with large ionization energy loss in pp collisions at $\sqrt{s} = 13 \text{ TeV}$ using the ATLAS experiment*. *Phys. Rev.*, D93(11):112015, 2016.
- [77] <http://cms-results.web.cern.ch/cms-results/public-results/publications/EXO/index.html>.
- [78] Giorgio Busoni, Andrea De Simone, Enrico Morgante, and Antonio Riotto. *On the Validity of the Effective Field Theory for Dark Matter Searches at the LHC*. *Phys. Lett.*, B728:412–421, 2014.
- [79] Giorgio Busoni, Andrea De Simone, Johanna Gramling, Enrico Morgante, and Antonio Riotto. *On the Validity of the Effective Field Theory for Dark Matter Searches at the LHC, Part II: Complete Analysis for the s-channel*. *JCAP*, 1406:060, 2014.

- [80] Giorgio Busoni, Andrea De Simone, Thomas Jacques, Enrico Morgante, and Antonio Riotto. *On the Validity of the Effective Field Theory for Dark Matter Searches at the LHC Part III: Analysis for the t-channel.* JCAP, 1409:022, 2014.
- [81] Daniel Abercrombie et al. *Dark Matter Benchmark Models for Early LHC Run-2 Searches: Report of the ATLAS/CMS Dark Matter Forum.* 2015.
- [82] A. Goudelis, B. Herrmann, and O. Stl. *Dark matter in the Inert Doublet Model after the discovery of a Higgs-like boson at the LHC.* JHEP, 09:106, 2013.
- [83] Bhaskar Dutta, Yu Gao, and Teruki Kamon. *Probing Light Nonthermal Dark Matter at the LHC.* Phys. Rev., D89(9):096009, 2014.
- [84] James S. Bullock. *Notes on the Missing Satellites Problem.* 2010.
- [85] Michael Boylan-Kolchin, James S. Bullock, and Manoj Kaplinghat. *Too big to fail? The puzzling darkness of massive Milky Way subhaloes.* Mon. Not. Roy. Astron. Soc., 415:L40, 2011.
- [86] David H. Weinberg, James S. Bullock, Fabio Governato, Rachel Kuzio de Naray, and Annika H. G. Peter. *Cold dark matter: controversies on small scales.* Proc. Nat. Acad. Sci., 112:12249–12255, 2014. [Proc. Nat. Acad. Sci.112,2249(2015)].
- [87] Benoit Famaey and Stacy McGaugh. *Challenges for Lambda-CDM and MOND.* J. Phys. Conf. Ser., 437:012001, 2013.
- [88] J. F. Donoghue, E. Golowich, and Barry R. Holstein. *Dynamics of the standard model.* Camb. Monogr. Part. Phys. Nucl. Phys. Cosmol., 2:1–540, 1992. [Camb. Monogr. Part. Phys. Nucl. Phys. Cosmol.35(2014)].
- [89] C. Downum, T. Barnes, J. R. Stone, and E. S. Swanson. *Nucleon-meson coupling constants and form-factors in the quark model.* Phys. Lett., B638:455–460, 2006.
- [90] Scott W. Randall, Maxim Markevitch, Douglas Clowe, Anthony H. Gonzalez, and Marusa Bradac. *Constraints on the Self-Interaction Cross-Section of Dark Matter from Numerical Simulations of the Merging Galaxy Cluster 1E 0657-56.* Astrophys. J., 679:1173–1180, 2008.
- [91] Jonathan L. Feng. *Dark Matter Candidates from Particle Physics and Methods of Detection.* Ann. Rev. Astron. Astrophys., 48:495–545, 2010.
- [92] Gregory D. Mack, John F. Beacom, and Gianfranco Bertone. *Towards Closing the Window on Strongly Interacting Dark Matter: Far-Reaching Constraints from Earth’s Heat Flow.* Phys. Rev., D76:043523, 2007.
- [93] J. Rich, R. Rocchia, and M. Spiro. *A Search for Strongly Interacting Dark Matter.* Phys. Lett., B194:173, 1987. [,221(1987)].
- [94] Adrienne L. Erickcek, Paul J. Steinhardt, Dan McCammon, and Patrick C. McGuire. *Constraints on the Interactions between Dark Matter and Baryons from the X-ray Quantum Calorimetry Experiment.* Phys. Rev., D76:042007, 2007.
- [95] Gregory D. Mack and Adithya Manohar. *Closing the window on high-mass strongly interacting dark matter.* J. Phys., G40:115202, 2013.
- [96] Richard H. Cyburt, Brian D. Fields, Vasiliki Pavlidou, and Benjamin D. Wandelt. *Constraining strong baryon dark matter interactions with primordial nucleosynthesis and cosmic rays.* Phys. Rev., D65:123503, 2002.
- [97] Xue-lei Chen, Steen Hannestad, and Robert J. Scherrer. *Cosmic microwave background and large scale structure limits on the interaction between dark matter and baryons.* Phys. Rev., D65:123515, 2002.

- 1 [98] Cora Dvorkin, Kfir Blum, and Marc Kamionkowski. *Constraining Dark Matter-Baryon Scattering*
2 *with Linear Cosmology*. Phys. Rev., D89(2):023519, 2014.
- 3 [99] H. Richard Gustafson, Cyril A. Ayre, Lawrence W. Jones, Michael J. Longo, and P. V. Ra-
4 mana Murthy. *Search for New Massive Long-lived Neutral Particles*. Phys. Rev. Lett., 37:474,
5 1976.
- 6 [100] K. A. Olive et al. *Review of Particle Physics*. Chin. Phys., C38:090001, 2014.
- 7 [101] N. Daci, Isabelle De Bruyn, S. Lowette, M. H. G. Tytgat, and B. Zaldivar. *Simplified SIMPs and*
8 *the LHC*. JHEP, 11:108, 2015.
- 9 [102] Esma Anais Mobs. *The CERN accelerator complex. Complexe des accrateurs du CERN*. Oct
10 2016. General Photo.
- 11 [103] S. Chatrchyan et al. *The CMS Experiment at the CERN LHC*. JINST, 3:S08004, 2008.
- 12 [104] David Aaron Matzner Dominguez, D. Abbaneo, K. Arndt, N. Bacchetta, A. Ball, E. Bartz,
13 W. Bertl, G. M. Bilei, G. Bolla, H. W. K. Cheung, et al. *CMS Technical Design Report for the*
14 *Pixel Detector Upgrade*. 2012.
- 15 [105] G. L. Bayatian et al. *CMS Physics*. 2006.
- 16 [106] Serguei Chatrchyan et al. *Energy Calibration and Resolution of the CMS Electromagnetic*
17 *Calorimeter in pp Collisions at $\sqrt{s} = 7$ TeV*. JINST, 8:P09009, 2013. [JINST8,9009(2013)].
- 18 [107] Giovanni Abbiendi. *The CMS muon system in Run2: preparation, status and first results*. PoS,
19 EPS-HEP2015:237, 2015.
- 20 [108] A. Tapper and Darin Acosta. *CMS Technical Design Report for the Level-1 Trigger Upgrade*.
21 2013.
- 22 [109] Jean-marc Olivier Andre, Ulf Behrens, James Branson, Philipp Maximilian Brummer, Olivier
23 Chaze, Sergio Cittolin, Cristian Contescu, Benjamin Gordon Craigs, Georgiana Lavinia Dar-
24 lea, Christian Deldicque, Zeynep Demiragli, Marc Dobson, Nicolas Doualot, Samim Erhan,
25 Jonathan Richard Fulcher, Dominique Gigi, Maciej Szymon Gladki, Frank Glege, Guillermo
26 Gomez Ceballos, Jeroen Guido Hegeman, Andre Georg Holzner, Mindaugas Janulis, Raul
27 Jimenez Estupinan, Lorenzo Masetti, Franciscus Meijers, Emilio Meschi, Remigius Mommsen,
28 Srecko Morovic, Vivian O'Dell, Luciano Orsini, Christoph Maria Ernst Paus, Petia Petrova, Marco
29 Pieri, Attila Racz, Thomas Reis, Hannes Sakulin, Christoph Schwick, Dainius Simelevicius, Petr
30 Zejdl, Hamburg, California, San Diego, California, Chicago, Illinois, Massachusetts Institute
31 of Technology, Cambridge, Massachusetts, also at Vilnius University, Vilnius, Lithuania, and also
32 at. *Performance of the CMS Event Builder*. Technical Report CMS-CR-2017-034, CERN, Geneva,
33 Feb 2017.
- 34 [110] Stefan Hche. *Introduction to parton-shower event generators*. In Proceedings, Theoretical Ad-
35 vanced Study Institute in Elementary Particle Physics: Journeys Through the Precision Frontier:
36 Amplitudes for Colliders (TASI 2014): Boulder, Colorado, June 2-27, 2014, pages 235–295, 2015.
- 37 [111] J. Pumplin, D. R. Stump, J. Huston, H. L. Lai, Pavel M. Nadolsky, and W. K. Tung. *New generation*
38 *of parton distributions with uncertainties from global QCD analysis*. JHEP, 07:012, 2002.
- 39 [112] A. D. Martin, W. J. Stirling, R. S. Thorne, and G. Watt. *Parton distributions for the LHC*. Eur.
40 Phys. J., C63:189–285, 2009.
- 41 [113] Richard D. Ball et al. *Parton distributions for the LHC Run II*. JHEP, 04:040, 2015.
- 42 [114] J. Alwall, R. Frederix, S. Frixione, V. Hirschi, F. Maltoni, O. Mattelaer, H. S. Shao, T. Stelzer,
43 P. Torrielli, and M. Zaro. *The automated computation of tree-level and next-to-leading order*
44 *differential cross sections, and their matching to parton shower simulations*. JHEP, 07:079, 2014.

- 1 [115] Stefano Frixione, Paolo Nason, and Carlo Oleari. *Matching NLO QCD computations with Parton*
2 *Shower simulations: the POWHEG method.* JHEP, 11:070, 2007.
- 3 [116] V. N. Gribov and L. N. Lipatov. *Deep inelastic e p scattering in perturbation theory.* Sov. J. Nucl.
4 Phys., 15:438–450, 1972. [Yad. Fiz.15,781(1972)].
- 5 [117] Yuri L. Dokshitzer. *Calculation of the Structure Functions for Deep Inelastic Scattering and e+ e-*
6 *Annihilation by Perturbation Theory in Quantum Chromodynamics.* Sov. Phys. JETP, 46:641–653,
7 1977. [Zh. Eksp. Teor. Fiz.73,1216(1977)].
- 8 [118] Guido Altarelli and G. Parisi. *Asymptotic Freedom in Parton Language.* Nucl. Phys., B126:298–
9 318, 1977.
- 10 [119] Torbjörn Sjöstrand, Stephen Mrenna, and Peter Skands. *PYTHIA 6.4 physics and manual.* JHEP,
11 05:026, 2006.
- 12 [120] Bo Andersson, G. Gustafson, G. Ingelman, and T. Sjostrand. *Parton Fragmentation and String*
13 *Dynamics.* Phys. Rept., 97:31–145, 1983.
- 14 [121] John M. Campbell and R. K. Ellis. *MCFM for the Tevatron and the LHC.* Nucl. Phys. Proc. Suppl.,
15 205-206:10–15, 2010.
- 16 [122] John Allison et al. *Geant4 developments and applications.* IEEE Trans. Nucl. Sci., 53:270, 2006.
- 17 [123] Serguei Chatrchyan et al. *Description and performance of track and primary-vertex reconstruction*
18 *with the CMS tracker.* JINST, 9(10):P10009, 2014.
- 19 [124] A. Strandlie and R. Frühwirth. *Discrimination between different types of material in track recon-*
20 *struction with a Gaussian-sum filter.* IEEE Trans. Nucl. Sci., 53:3842–3849, 2006.
- 21 [125] A. M. Sirunyan et al. *Particle-flow reconstruction and global event description with the CMS*
22 *detector.* JINST, 12:P10003, 2017.
- 23 [126] Matteo Cacciari, Gavin P. Salam, and Gregory Soyez. *The anti- k t jet clustering algorithm.* Journal
24 of High Energy Physics, 2008(04):063, 2008.
- 25 [127] Serguei Chatrchyan et al. *Identification of b-quark jets with the CMS experiment.* JINST, 8:P04013,
26 2013.
- 27 [128] Vardan Khachatryan et al. *Reconstruction and identification of lepton decays to hadrons and at*
28 *CMS.* JINST, 11(01):P01019, 2016.
- 29 [129] Adam Alloul, Neil D. Christensen, Céline Degrande, Claude Duhr, and Benjamin Fuks. *FeynRules*
30 *2.0 - A complete toolbox for tree-level phenomenology.* Comput.Phys.Commun., 185:2250–2300,
31 2014.
- 32 [130] Johann H. Kuhn, A. Kulesza, S. Pozzorini, and M. Schulze. *Electroweak corrections to hadronic*
33 *photon production at large transverse momenta.* JHEP, 03:059, 2006.
- 34 [131] Stefan Kallweit, Jonas M. Lindert, Stefano Pozzorini, Marek Schnherr, and Philipp Maierhöfer.
35 *NLO QCD+EW automation and precise predictions for V+multijet production.* In Proceedings,
36 50th Rencontres de Moriond, QCD and high energy interactions: La Thuile, Italy, March 21-28,
37 2015, pages 121–124, 2015.
- 38 [132] Stefan Kallweit, Jonas M. Lindert, Philipp Maierhöfer, Stefano Pozzorini, and Marek Schnherr.
39 *NLO electroweak automation and precise predictions for W+multijet production at the LHC.* JHEP,
40 04:012, 2015.
- 41 [133] Stefan Kallweit, Jonas M. Lindert, Philipp Maierhöfer, Stefano Pozzorini, and Marek Schnherr.
42 *NLO QCD+EW predictions for V + jets including off-shell vector-boson decays and multijet merg-*
43 *ing.* JHEP, 04:021, 2016.

- 1 [134] A. L. Read. *Presentation of search results: the CLs technique*. J. Phys., G28:2693, 2002.
- 2 [135] T. Junk. *Confidence level computation for combining searches with small statistics*. Nucl. Instrum.
3 Meth., A434:435, 1999.
- 4 [136] Oliver Buchmueller, Matthew J. Dolan, Sarah A. Malik, and Christopher McCabe. *Characteris-
5 ing dark matter searches at colliders and direct detection experiments: Vector mediators*. JHEP,
6 01:037, 2015.
- 7 [137] Andriy Kurylov and Marc Kamionkowski. *Generalized analysis of weakly interacting massive
8 particle searches*. Phys. Rev., D69:063503, 2004.
- 9 [138] Junji Hisano, Koji Ishiwata, and Natsumi Nagata. *Gluon contribution to the dark matter direct
10 detection*. Phys. Rev., D82:115007, 2010.
- 11 [139] R. Agnese et al. *New Results from the Search for Low-Mass Weakly Interacting Massive Particles
12 with the CDMS Low Ionization Threshold Experiment*. Phys. Rev. Lett., 116(7):071301, 2016.
- 13 [140] D. S. Akerib et al. *Improved Limits on Scattering of Weakly Interacting Massive Particles from
14 Reanalysis of 2013 LUX Data*. Phys. Rev. Lett., 116(16):161301, 2016.
- 15 [141] Andi Tan et al. *Dark Matter Results from First 98.7 Days of Data from the PandaX-II Experiment*.
16 Phys. Rev. Lett., 117(12):121303, 2016.
- 17 [142] G. Angloher et al. *Results on light dark matter particles with a low-threshold CRESST-II detector*.
18 Eur. Phys. J., C76(1):25, 2016.
- 19 [143] C. Amole et al. *Improved dark matter search results from PICO-2L Run 2*. Phys. Rev.,
20 D93(6):061101, 2016.
- 21 [144] C. Amole et al. *Dark matter search results from the PICO-60 CF₃I bubble chamber*. Phys. Rev.,
22 D93(5):052014, 2016.
- 23 [145] M. G. Aartsen et al. *Improved limits on dark matter annihilation in the Sun with the 79-string
24 IceCube detector and implications for supersymmetry*. JCAP, 1604(04):022, 2016.
- 25 [146] K. Choi et al. *Search for neutrinos from annihilation of captured low-mass dark matter particles
26 in the Sun by Super-Kamiokande*. Phys. Rev. Lett., 114(14):141301, 2015.
- 27 [147] M. Ackermann et al. *Constraining Dark Matter Models from a Combined Analysis of Milky Way
28 Satellites with the Fermi Large Area Telescope*. Phys. Rev. Lett., 107:241302, 2011.
- 29 [148] A. A. Abdo et al. *Observations of Milky Way Dwarf Spheroidal galaxies with the Fermi-LAT
30 detector and constraints on Dark Matter models*. Astrophys. J., 712:147–158, 2010.

List of Acronyms

1

2

3

A

4

5
6 ATLAS Almost Toroidal LHC ApparatuS

7

8

B

9

10
11 BU Builder Unit

12

13

C

14

15
16 CERN European Organization for Nuclear Research
17 CHS charged hadron subtraction
18 CMB Cosmic Microwave Background
19 CMS Compact Muon Solenoid
20 CSC Cathode Strip Chambers

21

22

D

23

24
25 DAQ data acquisition
26 DQM Data Quality Monitoring
27 DT Drift Tubes

28

29

E

30

31
32 ECAL electromagnetic calorimeter

33

34

F

35

36
37 FED Front End Driver
38 FSR final state radiation
39 FU Filter Unit

1

2

G

3

4

5	GSF	Gaussian-sum filter
---	-----	---------------------

6

7

H

8

10	HCAL	hadronic calorimeter
11	HLT	High-Level Trigger
12	HSCP	heavy stable neutral particle

13

14

I

15

16

17	IP	interaction point
18	ISR	initial state radiation

19

20

J

21

23	JER	jet energy resolution
----	-----	-----------------------

24

25

L

26

27

28	L1	Level-1
29	LEIR	Low Energy Ion Ring
30	LEP	Large Electron Positron
31	LHC	Large Hadron Collider
32	LO	leading order

33

34

N

35

36

37	NLO	next-to-leading order
----	-----	-----------------------

38

39

P

40

41

42	PDF	parton distribution function
43	PF	particle flow
44	PS	Proton Synchrotron
45	PSB	Proton Synchrotron Booster

1

2

Q

3

4

5 QCD

Quantum Chromodynamics

6

7

R

8

10 RF

radio-frequency

11 ROC

read-out chip

12 RPC

Resistive Plate Chambers

13 RU

Readout Unit

14

15

S

16

18 SIDM

self-interacting dark matter

19 SIMP

strongly interacting massive particle

20 SPS

Super Proton Synchrotron

21 SUSY

supersymmetry

22

23

T

24

26 TEC

Tracker EndCaps

27 TIB

Tracker Inner Barrel

28 TID

Tracker Inner Disks

29 TOB

Tracker Outer Barrel

30

31

W

32

34 WIMP

weakly interacting massive particle

